Carrier transport study for organic semiconductors using hydrostatic pressure

A DISSERTATION
SUBMITTED TO THE FACULTY OF THE GRADUATE SCHOOL
OF THE UNIVERSITY OF MINNESOTA
BY

Dominic David Schroepfer

IN PARTIAL FULFILLMENT OF THE REQUIREMENTS
FOR THE DEGREE OF
DOCTOR OF PHILOSOPHY

Prof. P. Paul Ruden

December 2008

Acknowledgements

First and foremost I would like to thank my advisor, Prof. P. Paul Ruden, for his guidance throughout this project. Without his support, both academic and financial, this work would not have been possible. Discussions with Prof. Ruden and my group members Dr. Mohammad Zahed Kauser, Dr. Yuming Liu, Jeff Balk, Mohammad Yunus, Isaiah Steinke, and Hsui-Chuang Chang have greatly aided the development of this thesis. I would also like to acknowledge the contributions of Prof. Marshall Nathan and his former student Dr. Zhenlin Rang for input and laboratory expertise.

I would also like to thank Prof. C. Daniel Frisbie for his guidance and financial support through MERSEC funding. I am indebted to Prof. Frisbie's research group, especially Dr. Sandra Fritz-Vos, Dr. Lei Diao, Dr. Jiyoul Lee, Dr. Jeong Ho Cho, Yan Liang, and Yu Xia for providing the samples tested in this project.

Valuable samples and discussions were also provided by Dr. Jia Chen of IBM in Yorktown Heights, NY, and Prof. Sean Shaheen, formerly at NREL and currently at the University of Denver.

Finally, I would like to thank my friends and family, especially my parents, Paul and Linda, and my girlfriend, Stacy Serum.

Abstract

Organic semiconducting materials show tremendous potential for use in low cost and light weight devices. However, transistors based on these materials are plagued with inconsistencies in their mobility and threshold voltage. To further the understanding of these devices, hydrostatic pressure is used in this research project to modify the transport properties of the free charge carriers within the semiconductor layer.

Thin film transistors made with P3HT are found to respond approximately linear with pressure in both the mobility and threshold voltage. A linear mobility increase of 300% over 1GPa is found for one sample and an increase of 130% is found for a second sample. The threshold voltages change by 40V (from 40V at atmospheric pressure to 0V at 1GPa) for the former device and by 15V (15V to 0V) for the latter. The mobility increase is attributed to a decrease in inter-molecular spacing, which is well approximated by a linear relationship due to the small change in inter-molecular spacing. The threshold voltage changes show evidence of a change in trap site energy relative to the zero-bias Fermi level. Preliminary temperature data indicates that the traps are donor like.

Pentacene thin film devices are tested and compared to the P3HT results. With large source to drain voltages (V_{ds} = -20V to -40V) the FETs made from pentacene thin films are unstable, but show initial increases in mobility of nearly 100% from atmospheric pressure to 100MPa. Lowering V_{ds} allows the data to appear more like the P3HT results, showing an approximately linear mobility increase of 100% through the entire 1GPa pressure cycle. The dependence of the threshold voltage on pressure for low V_{ds} has some curvature, but is still roughly linear from -25V at atmospheric pressure to

-15V at 1GPa. The threshold voltage change is positive (as opposed to negative for P3HT), which indicates increasing negative fixed space charge, but both films (P3HT and pentacene) shift closer to thresholds voltages of 0V. An alternative pentacene thin film device, a capacitor made of a pentacene film, SiO_2, and doped Si, is used to study the mobility in another manner. This device shows a nearly linear mobility increase of 500% for 1GPa of pressure. The threshold for this device is nearly constant, in contrast to the FET.

Carbon nanotubes and single crystals of organic semiconducting material are also made into FETs and tested versus pressure in this project. Carbon nanotubes are able to return a 50% increase in mobility with 1GPa of pressure, with an approximately constant threshold voltage. Data taken for single crystal rubrene devices extrapolates to a 1400% increase in mobility with 1GPa of pressure, based on data taken from atmospheric pressure to 70MPa (an increase of 100%). The single crystal device is unable to withstand any additional pressure, and the damage that occurs with pressure makes the threshold voltage shift difficult to characterize.

Table of Contents

Chapter 1: Introduction.....1

1.1 Background.....1

1.2 Motivation for pressure research.....2

1.2.1 Mobility vs. pressure.....4

1.2.2 Threshold voltage.....8

1.3 Overview of thesis.....8

Chapter 2: The pressure system.....11

2.1 Introduction.....11

2.2 The U11 Compressor.....11

2.2.1 Controlling the pressure.....14

2.2.2 Control feedback.....15

2.3 GC10 cell, plug, and capillary.....16

2.3.1 Electrical connections.....16

2.3.2 Sample table.....18

2.4 Gas purge.....20

2.5 Summary.....21

Chapter 3: P3HT.....22

3.1 Introduction.....22

3.2 Device fabrication.....24

3.3 Doping and impurity effects in P3HT films.....25

3.4 I-V response to pressure.....28

3.4.1 Mobility response.....29

3.4.2 Threshold voltage response.....30

3.5 Temperature dependence.....32

3.6 Ion gel device.....34

3.7 Summary/Conclusion.....35

Chapter 4: Pentacene thin films.....36

4.1 Introduction.....36

4.2 Device fabrication.....37

4.3 FET response to pressure.....38

4.4 Semiconductor-oxide-“metal” capacitor.....42

4.4.1 Analytic model.....45

4.4.2 Pressure response.....49

4.4.3 Capacitor summary.....52

4.5 Low drain voltage FET experiment.....53

Chapter 5: Carbon nanotubes.....56

5.1 Introduction.....56

5.2 Device setup.....57

5.3 Effects of pressure on I-V characteristics.....60

5.4 Temperature dependence.....63

5.5 Summary/Conclusion.....64

Chapter 6: Single molecular crystals.....65

6.1 Introduction.....65

6.2 Crystal and device fabrication.....66

6.3 Pressure effects on I-V characteristics.....67

6.4 Summary/Conclusions.....72

Chapter 7: Summary and future work.....73

7.1 Summary.....73

7.1.1 Mobility.....73

7.1.2 Threshold voltage shifts.....75

7.2 Future work.....76

Appendix A: The relationship between trapped charges and threshold voltage shifts. 78

A.1 Changing the trap site concentration 78

A.2 Fast traps 78

A.3 Slow traps 79

A.4 Conclusion 80

Appendix B: Pressure effect on the pentacene film.....81

Appendix C: Data summary for all of the pentacene thin film FETs presented in section 4.3. 84

C.1 Sample A.....84

C.1 Sample B.....85

C.1 Sample C.....87

C.1 Sample D.....88

C.1 Sample E.....90

Appendix D: Modeling a pentacene metal-semiconductor-metal structure. 92

D.1 Introduction.....92

D.2 Model framework.....93

D.2.1 Equilibrium.....93

D.2.2 Steady state, non-equilibrium.....95

D.2.3 Injection currents.....96

D.3 Applying the code to actual devices.....98

References..... 101

List of Tables

Table 4.1: The pentacene FET samples and their controlled differences.....38

Table D.1: Summary of model parameters used in figure D.1.....100

List of Figures

Figure 1.1: Plot of the overlap integral dependence on lattice spacing for the H_2^+ ion on a semi-logarithmic scale. 6

Figure 2.1: The pressure system. 12

Figure 2.2: Pressure system diagram. 12

Figure 2.3: The third stage of the U11 compressor with the piston retracted. 13

Figure 2.4: The front panel to the U11 compressor. 14

Figure 2.5: The GC10 cell and plug. 17

Figure 2.6: The sample table as shipped and the custom piece developed to hold the samples in a vertical position. 18

Figure 2.7: Custom sample table using pressure contacts. 19

Figure 2.8: Spring clamp holder. 19

Figure 2.9: Concept of gas flush. 21

Figure 3.1: Molecular diagram of P3HT. 23

Figure 3.2: Ordering of P3HT. 23

Figure 3.3: The P3HT FET structure and picture of actual device. 25

Figure 3.4: Current versus time for a P3HT sample at atmosphere in an argon environment. 26

Figure 3.5: Progression of an I_d-V_{gs} curve during the stabilization process. ...26

Figure 3.6: Example of stabilization during a pressure run. 27

Figure 3.7: Current changes with pressure for a P3HT device. 28

Figure 3.8: I_d-V_{gs} plots for samples 1 and 2 at pressure. 29

Figure 3.9: Linear mobility versus pressure for P3HT. 30

Figure 3.10: Threshold voltages versus pressure for P3HT. 31

Figure 3.11: Mobility versus pressure for a P3HT device at room temperature and at 10C. 33

Figure 3.12: Mobility and threshold voltage versus pressure during the cooling of the P3HT sample. 33

Figure 3.13: Threshold voltage versus pressure for a P3HT device at room temperature and 10C. ..34

Figure 3.14: I_d-V_{gs} curves under pressure for a P3HT FET made with ion gel replacing the gate insulator. 35

Figure 4.1: I_d-V_{gs} at atmospheric pressure for pentacene FETs while sealed in the pressure system before and after pressure application. 40

Figure 4.2: Mobility versus pressure for devices A, B, and D. 40

Figure 4.3: Threshold voltage versus pressure for devices A, B, and D. 41

Figure 4.4: Schematic of the pentacene-oxide-metal capacitor. 42

Figure 4.5: A typical I-V response for the pentacene capacitor. 43

Figure 4.6: Current curve of the capacitor device during the pressure run. 44

Figure 4.7: Carrier profile of the capacitor from a simple model. 46

Figure 4.8: Predicted current response for the capacitor. 47

Figure 4.9: Slope and mobility versus pressure plot for the capacitor. 50

Figure 4.10: Number of carriers in the pentacene layer versus pressure. 51

Figure 4.11: Plot of the capacitor current with a fully charged channel versus pressure. 52

Figure 4.12: I_d-V_{gs} of a pentacene FET with low V_{ds} at pressure. 54

Figure 4.13: Mobility and threshold voltage versus pressure for a pentacene FET with low V_{ds}. 54

Figure 5.1: An AFM image of the CNT layer. 58

Figure 5.2: Final device layout and dimensions for the CNT FET. 58

Figure 5.3: Device mounting process for the CNT FET. 59

Figure 5.4: Simple analysis of gas penetration into the CNT. 61

Figure 5.5: The CNT device I_d-V_{gs} curves under Ar pressure. 62

Figure 5.6: Change in mobility versus pressure of CNT FET. 62

Figure 5.7: Threshold voltage changes versus pressure of CNT FET. 63

Figure 5.8: I_d-V_{gs} curves for CNT FET in a temperature test. 64

Figure 6.1: Device setup of a FET on a rubrene crystal. 65

Figure 6.2: A. Diagram of an organic crystal on a silicon wafer device. 67
B. Crystal on PDMS stamp.

Figure 6.3: Image of the bulk crystal sheared off of the interfacial layer ...68
connected to the Si wafer.

Figure 6.4: Current versus pressure plot for the device shown in 69
figure 6.3.

Figure 6.5: Mobilities versus pressure for the device shown in 69
figure 6.3.

Figure 6.6: Threshold voltage shift for the device shown in figure 6.3. 70

Figure B.1: Optical image of a pentacene thin film FET channel 81
blister damage after pressure is applied.

Figure B.2: AFM image of a pentacene thin film before and after 82
pressure.

Figure B.3: X-ray diffraction data for a pentacene thin film before 83
and after pressure.

Figure C.1: I_d-V_{gs} for sample A under pressure. 84

Figure C.2: Current versus pressure for sample A. 85

Figure C.3: Mobility and threshold voltage versus pressure for 85
sample A.

Figure C.4: I_d-V_{gs} for sample B under pressure. 86

Figure C.5: Current versus pressure for sample B. 86

Figure C.6: Mobility and threshold voltage versus pressure for 87
sample B.

Figure C.7: I_d-V_{gs} for sample C under pressure. 87

Figure C.8: Current versus pressure for sample C. 88

Figure C.9: Mobility and threshold voltage versus pressure for 88
sample C.

Figure C.10: I_d-V_{gs} for sample D under pressure. 89

Figure C.11: Current versus pressure for sample D. 89

Figure C.12: Mobility and threshold voltage versus pressure for 90
sample D.

Figure C.13: I_d-V_{gs} for sample E under pressure. 90

Figure C.14: Current versus pressure for sample E. 91

Figure C.15: Mobility and threshold voltage versus pressure for 91
sample E.

Figure D.1: Plot of the experimental data and model fits for the 100
pentacene metal-semiconductor-metal device.

Chapter 1: Introduction

1.1 Background

Studies on organic semiconductors have been conducted for many years, but interest has increased considerably in the last decade. In the mid and late 1990s several groups found that increasing the order of organic semiconducting thin films resulted in charge carrier mobilities comparable to amorphous silicon.[1,2,3,4,5,6,7] This research demonstrates that organic semiconductor based electronic devices can achieve performance benchmarks in field effect transistors (FETs) of mobility and on/off current ratio that rival amorphous silicon. This enables applications for organic semiconductor based devices from new technologies which could overcome the previously poor performance to the development of devices that expand the technology based on amorphous silicon.[2,8,9,10,11,12,13,14,15]

The drive to develop organic semiconductor devices stems from the ability of these materials to be light, cheap, flexible, and processable on a large scale. Organic thin films are lighter and more flexible than amorphous silicon films and can be deposited on light and flexible substrates.[13,16,17,18,19] Fabricating organic semiconductor based devices can be accomplished with solution based deposition and printed contacts, avoiding the costly vacuum processes inherent in silicon technology.[11,13,17,18,20,21,22,23,24,25,26,27] The elimination of vacuum equipment allows organic devices to be more easily scalable. Currently, the best laboratory devices are deposited on silicon and use thermally evaporated (in vacuum) gold electrodes, negating the advantages listed above. However, devices constructed of all organic materials, including the electrodes, and on plastic

substrates have been demonstrated.[13,16,17,18,19] There is still much work to be done, but the benefits of an organic material based semiconductor technology are promising and drive the current research strongly.

1.2 Motivation for pressure research

There is a direct correlation between the amount of order in an organic semiconductor (or any semiconductor) and the charge carrier mobility.[1,7,22,26,28,29] Current thin film deposition processes can create enough order to allow so-called band like transport to occur.[4,30,31] However the mobility is more likely to be defined by a hopping or trap and release type model for transport.[4,32,33,34] The order in the organic material allows π orbital overlap leading to their bulk semiconducting properties. Studies on single crystals of these materials provide a near perfect long range order and may provide a best case scenario for what thin films can achieve.[31,35,36] The packing of organic materials can take a herringbone motif, misaligning the π orbitals.[37,38,39] Research is being done to chemically alter the stacking motif to try and align the orbitals better.[40,41,42] Another method to increase overlap is to mechanically force the molecules closer together by applying hydrostatic pressure, this is the method used during this project.[37,38]

Applying pressure to a semiconductor is used to force the constituent molecules or atoms of a film into closer proximity. The tighter packing increases orbital overlap, altering the band structure of the material and increasing the mobility. In a molecular system the pressure can also alter the molecular form (bond length stretching and compression) and structural degrees of freedom, as observed by Raman

spectroscopy.[34,43,44,45,46,47,48,49] In situ measurements of these effects are not possible with the equipment used here, any changes they have on the transport will be measured and analyzed in terms of macroscopic device operation. Pressure is also found to cause phase changes and polymorph transitions in some organic materials.[38,50,51,52,53] When a persistent variation occurs in the before and after pressure data, characterization will be preformed on the material to check for possible lattice changes. For this project, the devices will be monitored primarily in field effect transistor operation to extract the mobility and threshold voltage changes. In doing this, the transport of free charge carriers (mobility) and the fixed space charge (threshold voltage) in the material will be monitored.

The transistors tested in this project are operated within the linear (or triode) region ($|V_{ds}|<|V_{gs}-V_T|$; V_{gs} is the gate to source voltage, V_T is the threshold voltage, and V_{ds} is the drain to source voltage). The transistor equation governing this condition is given by:

$$I_D = (\frac{W}{L})\frac{\mu C}{2}(2(V_{gs} - V_T)V_{ds} - V_{ds}^{\ 2}) \qquad \text{Equation 1.1}$$

The drain current (I_D) is measured for specified source/gate and source/drain biases applied. The capacitance (C) is governed by the SiO_2 (bulk modulus of 100GPa) which will change by less than 1%. Likewise the width and length (W and L) values will also be governed by the SiO_2 and their ratio will change even less. This leaves the mobility (μ) and threshold voltage (V_T) as pressure dependent parameters.

1.2.1 Mobility vs. pressure

A change in mobility with changing pressure can be easily seen conceptually by thinking of the pressure as a reduction in lattice spacing within the material. As the pressure increases the volume decreases, reducing the space between carrier sites. This means that the carriers experience less resistance moving from site to site. For a small polaron model with hopping transport, this manifests itself as an increase in the tunneling probability, which is proportional to $exp(-2\rho/\lambda)$; ρ is the distance between carrier sites and λ is the localization length of the small polaron carrying the charge.[54] The localization length will likely shrink with ρ but is assumed to be minor in comparison.

A band transport model will also result in easier motion of the carriers, although in a less direct manner. To illustrate the effects of lattice spacing on the mobility in a band transport framework, a simple one-dimensional tight binding model is presented. The starting equations for a tight binding treatment are:[55]

$$\begin{aligned} \langle k | H | k \rangle &= \alpha - \gamma \sum_m \exp(-ik \cdot p_m) = \varepsilon_m(k) \\ -\alpha &= \int dV\, \varphi^*(r) H \varphi(r) \\ -\gamma &= \int dV\, \varphi^*(r-\rho) H \varphi(r) \\ \Psi_k(r) &= \sum_j C_{jk} \varphi(r - r_j) \end{aligned}$$

Equation 1.2

α is a self energy term and γ represents an overlap integral. Within the tight binding approximation α remains constant with decreasing spacing, but the overlap term will change. For a simple example to find the nature of the overlap dependence on lattice spacing ρ, the formation of the hydrogen ion (H_2^+) is considered in the ground state. The ground state of a single hydrogen atom is:

$$\Psi_{gi}(r_i) = \frac{1}{\sqrt{\pi a^3}} \exp(-r_i / a) \qquad \text{Equation 1.3}$$

with a being the Bohr radius and the subscript i identifying the two atoms (i=1,2). The tight binding approximation gives a system wave function of:

$$\Psi_g(r) = A(\Psi_{g1}(r) \pm \Psi_{g2}(r-\rho)) \qquad \text{Equation 1.4}$$

A is a normalization factor. This yields an overlap integral of:

$$\begin{aligned} -\gamma &= \frac{1}{\pi a^3} \left\langle \exp(-(r-\rho)/a) \middle| H_1 + H_2 \middle| \exp(-r/a) \right\rangle \\ -\gamma &= \frac{1}{\pi a^3} (E_{g1} + E_{g1}) \left\langle \exp(-(r-\rho)/a) \middle| \exp(-r/a) \right\rangle \end{aligned} \qquad \text{Equation 1.5}$$

The effects of the two Hamiltonians on their respective ground state wave functions are to return the ground state energy of the individual atoms, which are the same. The ground state energy, like the self energy, does not change with changing ρ, so the integral is the only factor that can vary with pressure. Before looking at the integral itself, a variable substitution is useful. By placing one atom at the origin, the r vector becomes $r\hat{r}$, the other vector becomes:

$$(\vec{r} - \vec{\rho}) = \sqrt{r^2 + \rho^2 - 2r\rho\cos(\theta)}\,\hat{r} \qquad \text{Equation 1.6}$$

now substituting:

$$\begin{aligned} y &= \sqrt{r^2 + \rho^2 - 2r\rho\cos(\theta)} \\ d(y^2) &= 2y\,dy = 2r\rho\sin(\theta) \end{aligned} \qquad \text{Equation 1.7}$$

This makes the integral:

$$\gamma \propto \int dV \ \exp(-(r-\rho)/a)\exp(-r/a)$$

$$\gamma \propto \iiint \exp(-y/a)\exp(-r/a)r^2 \sin(\theta)\, d\phi\, d\theta\, dr$$

$$\gamma \propto 2\pi \int_0^{\infty} \exp(-r/a)\, r \frac{1}{\rho} \int_{|r-\rho|}^{r+\rho} \exp(-y/a)\, y\, dy\, dr \qquad \text{Equation 1.8}$$

$$\gamma \propto \exp(-\rho/a)\left(\frac{\rho^2}{3a^2} + \frac{\rho}{a} + 1\right)$$

As can be seen, the overlap integral increases as an exponential function with decreasing ρ. While there is a polynomial factor of ρ that will decrease the overlap with decreasing spacing, this is not the dominant feature. To clarify, the value on the right side of equation 1.8 is plotted versus ρ/*a* for ρ/*a* > 1, see figure 1.1.

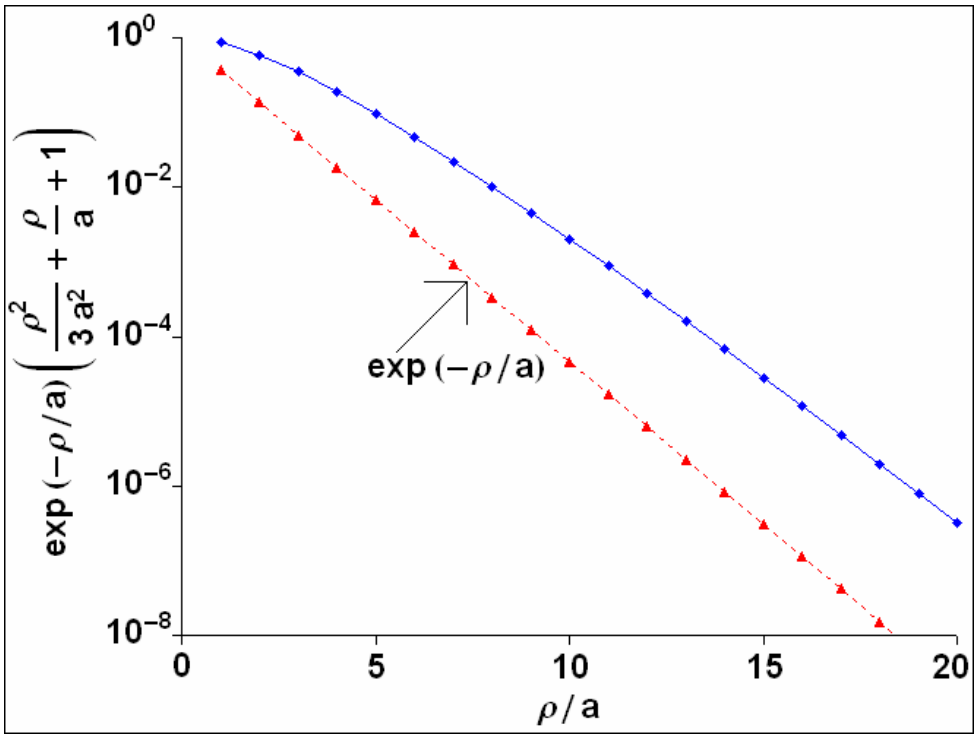

Figure 1.1, Plot of the overlap integral dependence on lattice spacing for the H_2^+ ion on a semilogarithmic scale. See equation 1.8.

The final element of the tight binding equation shown in equation 1.2 is the summation multiplier to the overlap integral. To get a sense of this factor a simple linear chain of identical atoms is considered. In this case the equation is:

$$\varepsilon_m = -\alpha - \gamma \sum_m \exp(-ik \cdot p_m) = -\alpha - \gamma[\exp(-ik\rho) + \exp(ik\rho)]$$
$$\varepsilon_m = -\alpha - \gamma(2\cos(k\rho)) \qquad \text{Equation 1.9}$$

For small $k\rho$:

$$\varepsilon_m = -\alpha - \gamma(2\cos(k\rho)) = -\alpha - 2\gamma(1 - (\frac{k\rho}{2})^2) \qquad \text{Equation 1.10}$$

It is evident that the lattice spacing ρ does affect the energy of the electron system, now an expression connecting ρ and the mobility is needed.

The mobility is given by:

$$\mu = \frac{q\tau_0}{m^*} \qquad \text{Equation 1.11}$$

τ_0 is the mean time between scattering events and only adds to the mobility increase with pressure if there is any change at all. q is the electron/carrier charge. m^* is the effective mass, which can be calculated directly from the energy equation 1.10:

$$\mu \propto \frac{1}{m^*} = \frac{1}{\hbar^2}\frac{\partial^2 \varepsilon(k)}{\partial k^2} = \frac{2\gamma\rho}{\hbar^2} \qquad \text{Equation 1.12}$$

There is a power dependence of the overlap on the distance, but the overall effect will be governed by the exponential change in the effective mass given by the overlap integral (γ) as is evident from figure 1.1.

1.2.2 Threshold voltage

The threshold voltage is the minimum V_{gs} that allows a conducting channel to form in the semiconducting material, which can be looked at as:

$$V_{gs} = -\frac{Q}{C} = -\frac{1}{C}(Q_{fixed} + ep_s) = V_T - \frac{ep_s}{C}$$
$$V_T = -\frac{Q_{fixed}}{C} \qquad \text{Equation 1.13}$$

As stated, the capacitance can be considered to be independent of pressure. This leaves the fixed sheet charge in the organic semiconductor (Q_{fixed}) to account for any change in threshold voltage. The negative sign is written explicitly to show that a negative gate voltage creates positive charges, and to form the direct relation to equation 1.14. There are two ways to change the fixed charge considered in this project; a change in the trap energy level separation with the zero-bias Fermi level and an increase in trap site concentration due to damage. This is explored in more detail in appendix A. The detailed mechanism of fixed charge change is uncertain; but within the assumptions presented, the change in threshold voltage can be defined as:

$$\Delta V_T = -\frac{\Delta Q_{fixed}}{C} \qquad \text{Equation 1.14}$$

1.3 Overview of thesis

Chapter 2 will cover the pressure system used for this project. It will explain the U11 compressor and its controls. The GC10 plug and its operation are also covered. Modifications to the equipment and prescribed operating procedures that are required for experimentation are explained.

Chapter 3 will cover the experiments done on P3HT thin films. The P3HT films show a strong response to pressure in both the measured mobility and threshold voltage. While these responses are primarily linear it is reasoned that the mobility's exponential change is small enough to appear linear. Some self doping and dedoping phenomena are covered. Early data for expansions from the basic pressure versus transistor operation experiment is also given.

Chapter 4 covers experiments done on pentacene thin films. Pentacene thin film transistors are tested in a similar fashion as the P3HT devices tested in chapter 3. Instability in the pentacene device characteristics motivates an exploration of a semiconductor-insulator-metal capacitor device. The results from this device are analyzed and compared to the transistor data.

Chapter 5 covers tests done on carbon nanotube (CNT) FETs. The experiment probes (ideally) single semiconducting CNT devices. A brief discussion of CNT devices under pressure in a helium versus argon environment is presented. Pressure results for a CNT FET in Ar are analyzed. A temperature test of a CNT device is also exhibited.

Chapter 6 covers tests done on single crystal rubrene samples. A FET fabricated from a single crystal of rubrene is used to avoid the problems posed by grain boundaries. Low pressure results (atmosphere to 70MPa) are presented. Difficulties in expanding the experiment to higher pressures are discussed as well as attempts to overcome these difficulties.

Chapter 7 contains a summary of these results and how they are interpreted collectively. Then suggested continuations for each of these experiments are presented.

Appendix A contains a formulation relating the threshold voltage shift to the change in energy separation between the HOMO level and trap energy level.

Appendix B contains data from optical, AFM, and x-ray analysis on pentacene thin films before and after exposure to pressure.

Appendix C contains a more complete data summary for the pentacene FETs tested in chapter 4, section 4.3.

Appendix D contains modeling work done on a metal-pentacene-metal device structure.

Chapter 2: The pressure system

2.1 Introduction

The gas pressure system consists of a U11 compressor and a GC10 gas pressure cell from Unipress (a commercial division of the Polish Institute of High Pressure Physics), see figure 2.1. The system works by compressing gas from a base source pressure of 8 to 18MPa in three stages to a maximum pressure of 1300MPa (1GPa ≈ 10kbar). The compressor houses three compression stages and contains the control mechanisms to regulate the pressure. The pressure is transmitted to the GC10 cell, which contains the sample, through a capillary. Sealing plugs for the GC10 cell contain sample holders and electrical feedthroughs to access the sample. The following is a detailed description of the compressor, GC10 cell and plug, sample holders, and system operation.

2.2 The U11 Compressor

The pistons and cylinders housed in the compressor are the foundation of the pressure system. The pressure is increased by reducing the active volume of the cylinders. To make the piston action more effective, the cylinders (also referred to as stages) of the pressure system can be isolated from each other. This allows one piston to fully extend, compress the gas within its cylinder, and be shut off from the system to reduce the base volume for the next stage. The force on the pistons is supplied by pressurized oil reaching 80MPa. In order to reach the maximum pressure of 1300MPa, the pistons utilize an area conversion of 1:1, 5:1, and 80:1 to increase the maximum pressure in these three cylinders by the same ratio. Ideally the final 80:1 conversion will

create more than 1300MPa in pressure, but other parts of the compressor and cell limit the peak pressure. The source gas is supplied partially pressurized, at least 8MPa and no more than 18MPa for He, to ensure that the full 1300MPa can be reached. The basic pressurization of the system starts by filling the cylinders with the pressurized source gas then closing the system from the source. The three stages are compressed individually by allowing the oil to pressurize one cylinder at a time. A diagram of the pressure system is shown in figure 2.2.

Figure 2.1: The pressure system, a U11 compressor from Unipress connected to a capillary leading into a safety enclosure to the GC10 cell behind the compressor.

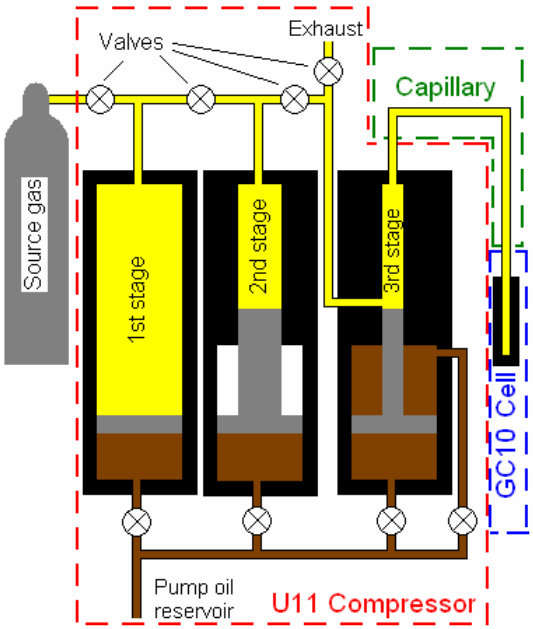

Figure 2.2: Pressure system diagram, major sections of the system are designated by the dashed lines.

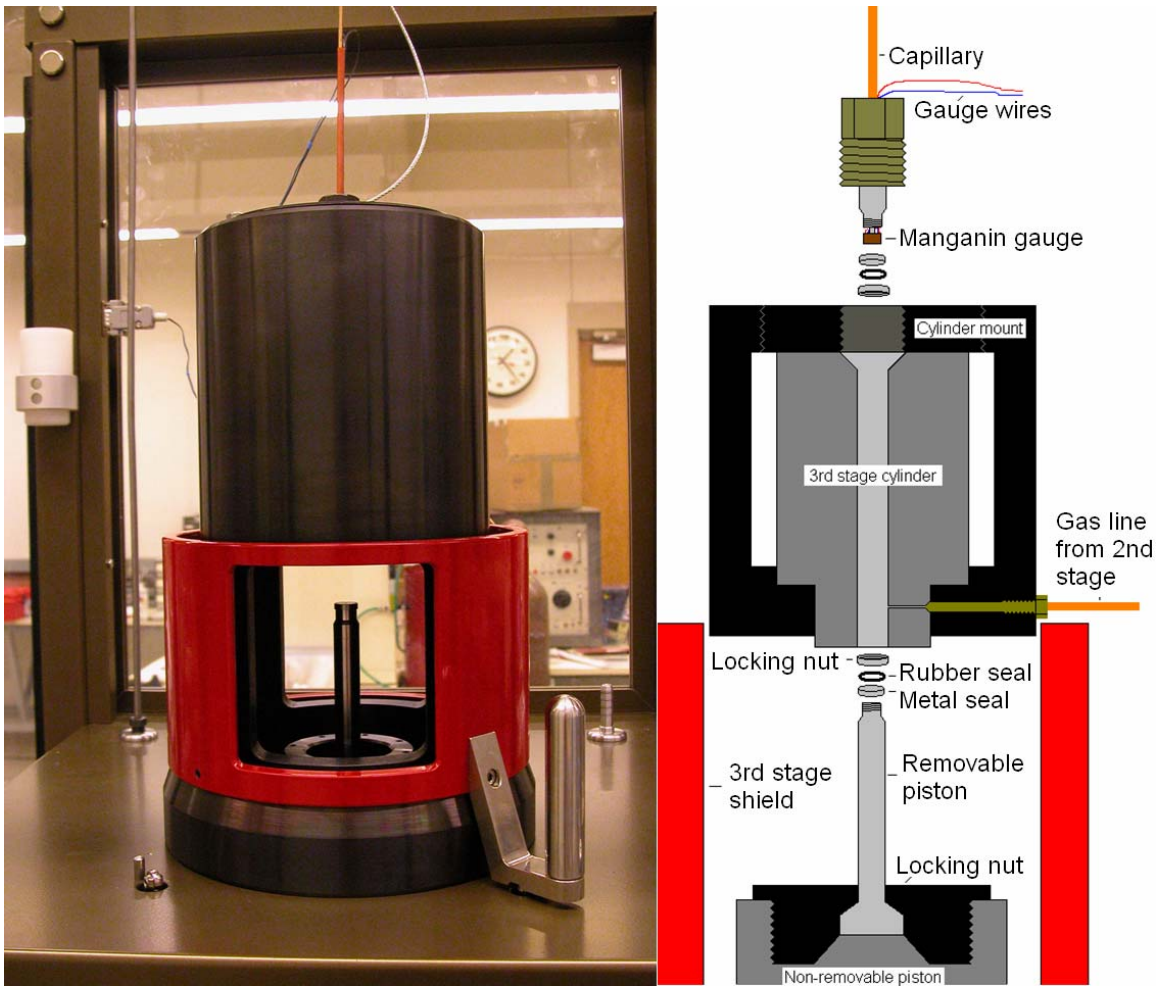

Figure 2.3: The third stage of the U11 compressor with the piston retracted.

The first and second stages are completely housed within the compressor and are not accessible, but the third stage is not fully enclosed. Given the pressures in the third stage, it is envisioned that maintenance will be required. The upper part of the third stage piston and cylinder, the parts exposed to the high gas pressure, can be disconnected from the U11 compressor, see figure 2.3. This access allows for regular replacement of the seals exposed to high pressures, both on the piston and at the capillary. The seals for this stage consist of rubber and metal on both the piston and capillary. The rubber seal is meant to provide the seal at low pressures and push on the metal one until the metal seal

is able to conform to the piston or capillary surface and the inner bore of the cylinder, at which point the metal seal takes over.

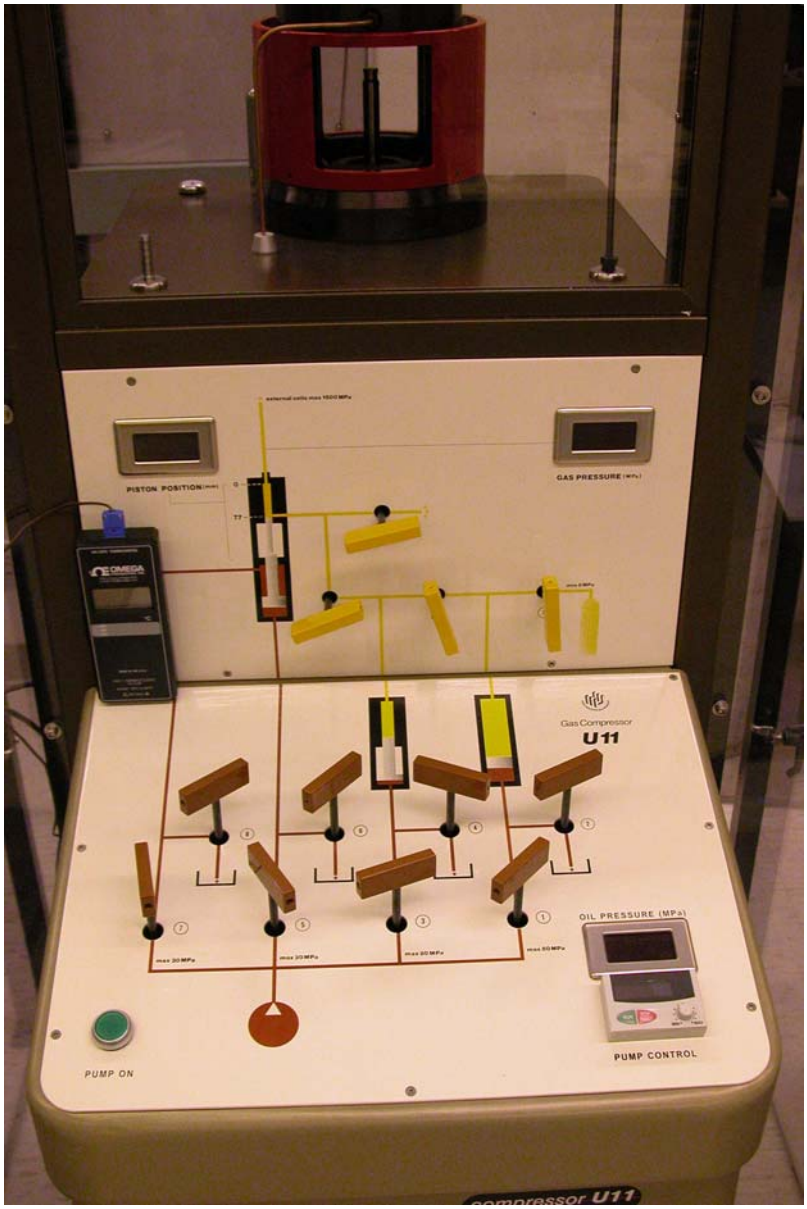

Figure 2.4: The front panel to the U11 compressor.

2.2.1 Controlling the pressure

Control of the pressure is governed by the user's control of the pump oil pushing on the cylinders. As mentioned, the oil from a pump is fed into the first, second, or third

stage depending on the valve settings. A speed control for the pump is provided on the front panel as well as all the control valves, shown in figure 2.4. The lowest pressure increase speed allowed by the pump speed controller is too fast for most of the samples tested in this project. A method to gain more control over the ramping speed by allowing only some of the oil pressure supplied by the pump to reach the piston is used to slow down the ramp. The excess oil bleeds into the oil reservoir through an unused cylinder. This, in principle, allows the ramp speed to be set as low as desired.

The ramp down in pressure is controlled by draining the oil from the compressed cylinders and bleeding the gas through the isolation valves separating the gasses in the first, second, and third stage. The method to increase pressure is largely replicated in venting. First the pressure from a stage is bled into the feed line, then from the feed line into the reservoir through an unused stage. To switch between stages (for example when the third stage is completely vented to 300MPa) the preceding stage is pressurized to match (the second stage is pressurized to 300MPa), and the gas valve separating the stages is opened, then the oil release is repeated on the preceding stage. To complete the ramp to atmosphere the source gas pressure is vented directly to the atmosphere.

2.2.2 Control feedback

There are three indicators on the front panel in figure 2.4 and two additional sensors that are monitored during the pressure cycle. On the front panel are gauges for the piston position of the third stage, the oil pressure in the feed line to all three cylinders, and the gas pressure in the third stage. Additionally there is a semiconductor pressure gauge and a thermocouple located on the plug which can be read with a multimeter

outside the system. The piston position gauge on the third stage is used primarily in servicing the system and detecting problems. The oil pressure gauge is used to monitor the oil pressure entering the stages. The gas pressure sensor is a manganin gauge located on the third stage end of the capillary. It uses a four probe resistance measurement to determine the resistance of the sensor and converts that to a pressure internally; there is also a set of tuning knobs for this gauge located on the compressor for calibration. The semiconductor gauge on the plug is primarily used when the system is placed in a cryogenic environment, since the manganin gauge is sensitive to temperature. A thermocouple on the plug is used extensively to ensure that the system remains at an approximately constant temperature; changes are restricted to +/-0.5C.

2.3 GC10 cell, plug, and capillary

The capillary and GC10 cell are primarily Be/Cu tubes used to transfer and hold the pressurized gas. The capillary consists of a thin (3mm diameter), flexible, tube with the manganin gauge and third stage connector on one end and the GC10 cell connector on the other. The cell is a short, thick, tube that encloses the sample. However, it is limited to 6mm in diameter and roughly 2cm in length of enclosed space. The seals to the cell, for both the capillary and the plug, are made with metal seals that are torqued into place before each run.

2.3.1 Electrical connections

The sample plug contains all of the feedthroughs that are used to probe the sample while under pressure, figure 2.5. The parts of the plug responsible for sealing the cell are

made out of Be/Cu. The feedthroughs enter the plug through a hole that flares out on the pressurized side, forming a socket into which the pressure forces a Be/Cu cone. The wires are inserted into this hole, spread out around the socket, and covered with pyrophilite (to seal the cone and socket). The cone for the socket is made with a screw to connect to the sample holder. The wires are thin, greater than 32 gauge, and coated in varnish to isolate them electrically from each other and the plug. There are 12 wires total, consisting of six copper wires for probing the sample, a copper and constantan wire pair to form a type k thermocouple, and two each of copper and constantan to access the semiconductor gauge (a four probe resistance measurement). The semiconductor gauge wires are chosen to be two each of copper and constantan to allow the gauge wires to act as spares if one of the other wires breaks. The thermocouple wires are simply soldered

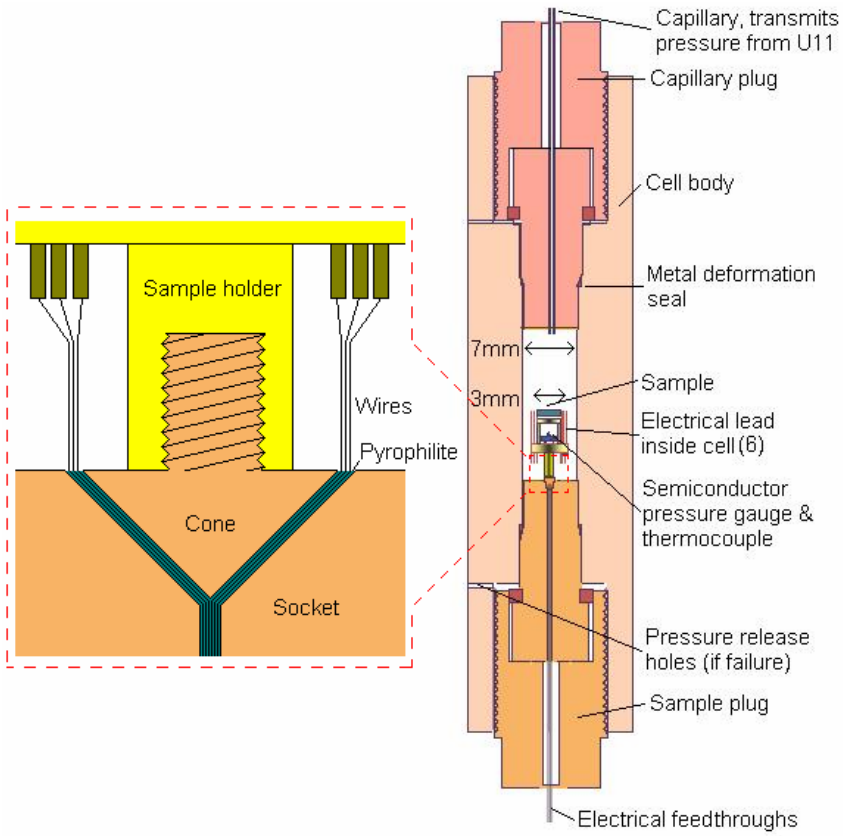

Figure 2.5: The GC10 cell and plug

together and placed under the sample table. The rest of the wires are soldered to brass pins that are held in the sample holder. The sample makes contact to the probing pins through an indium cap on each pin; ideally this allows the wires to simply be pressed into the indium, but they can also be soldered.

2.3.2 Sample table

The sample table (to hold the sample under test on the plug) uses two pins inserted into holes on the sample holder's base and held in place by friction. The sample size restriction for the system as shipped is roughly 3mm in diameter and 2cm tall. An alteration to the sample table by turning it 90 degrees allows a 10mm long and 5mm wide plate, see figure 2.6. Another variation is to lengthen the plate to 20mm and place 0-80 screw holes on the ends of the plate. Then an acrylic plate, 20mm long with metal pins running through it, is fastened onto the plate to form a small probe station, figure 2.7. The last variation used the same brass piece with the screw holes and took Be/Cu foil cut

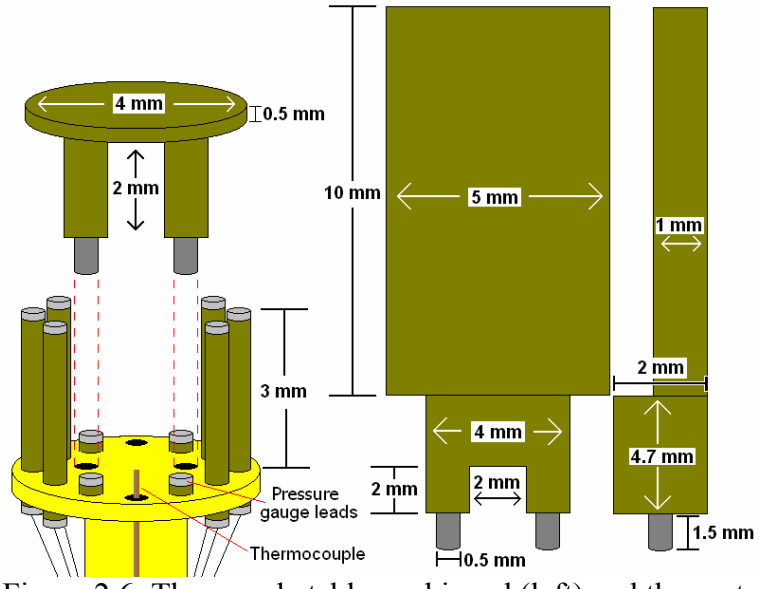

Figure 2.6: The sample table as shipped (left) and the custom piece (right) developed to hold the samples in a vertical position.

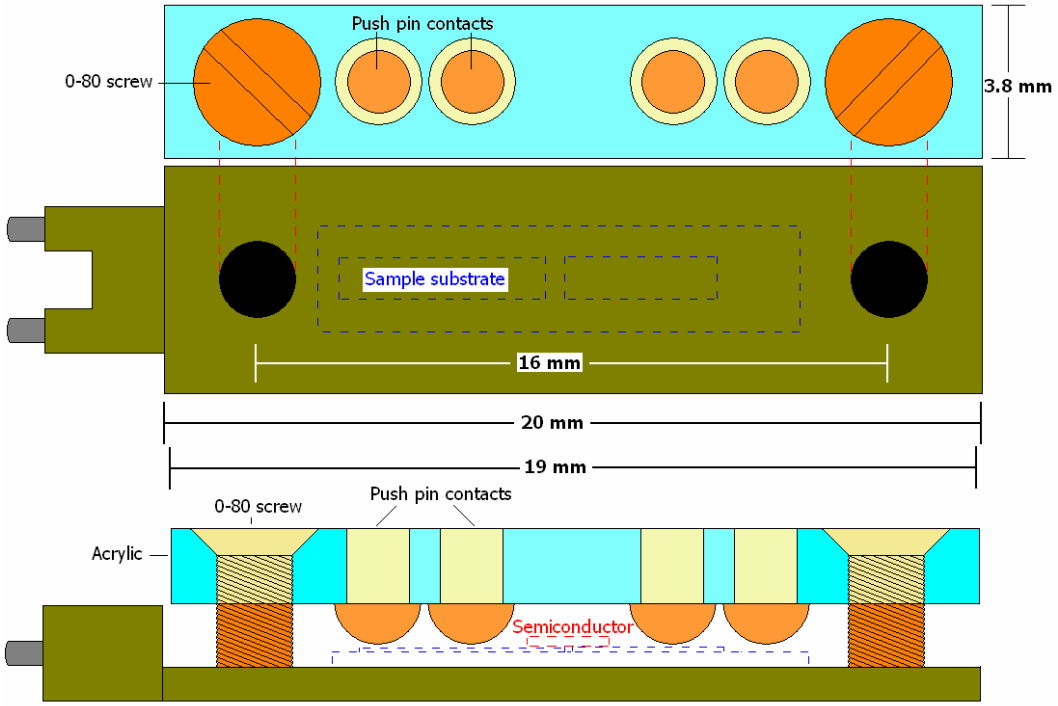

Figure 2.7: Pressure contact to the sample device (like a probe station). Contact to the plug made by connecting wires to the tops of the push pins. Used for samples that are sensitive to silver paste or solder contacts.

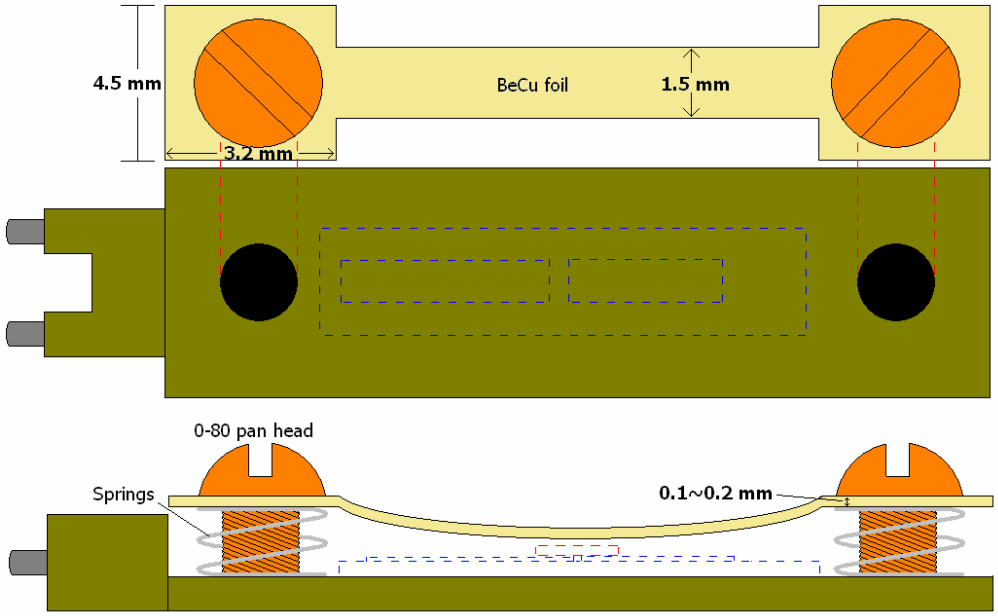

Figure 2.8: Spring clamp holder, connections still made by silver paint and gold wires on the device contacts. In development to remedy single crystal delamination from soft substrates (chapter 6).

into a strip, bent in a curve, and tightened down with screws to form a spring clamp, see figure 2.8. The sample tables prove to be useful in customizing the pressure system according to sample constraints.

2.4 Gas purge

The final aspect of the pressure system covered here is purging the system until only pure source gas remains. As already mentioned, the source gas is provided to the system at pressures below 18MPa but above 8MPa. For this project, bottled gasses of carrier grade or better are used with an initial pressure of 18MPa. The directed purge method is to bring the sealed system up to the bottle pressure, close off the third stage, and then vent only the third stage to the atmosphere. This is to be repeated two or three times depending on the purity needed. During experiments it is found that even with these low pressures some devices can be detrimentally altered. To avoid pressurizing the system before the experiment begins, the system is instead flushed of environmental gasses. To flush the system the cell/capillary connection is left open but the capillary is still directing all gas into the cell. Then as the gas flows through the capillary, the exhaust will flush the cell and eventually the system will contain only (or at least a high percentage) of the bottle gas, figure 2.9. To seal the system from the atmosphere, the cell/capillary connection is closed while a little bit of gas is still exiting the capillary, this may cause the cell to pressurize slightly but not as much as purging the system would. This will work best with Ar or some other gas that is heavier than air, so that the heavy gas can pool in the cell. The method has proved useful and is now the default method.

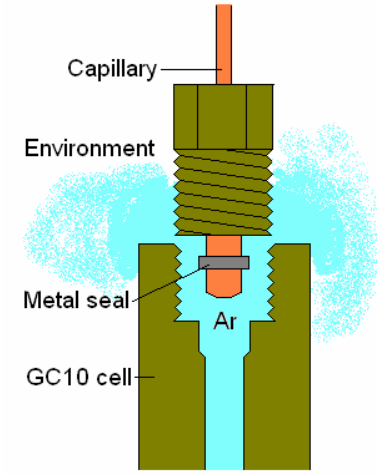

Figure 2.9: Concept of gas flush.

2.5 Summary

This summarizes the operation and capabilities of the pressure system. As demonstrated, there is some room for customization within the system but essentially the device is to be used as prescribed. Control of the pressure ramp has been refined to a useful level. The capillary gives some additional flexibility in the experiments that can be performed but given the space constrictions and the all metal cell, the practical extensions are restricted to temperature baths. The baths are primarily cooling due to any heating above 60C being deemed detrimental to the Be/Cu alloys. There is an optical cell, available from Unipress, which could allow for some additional experiments and the manufacturer is willing to work with us on custom equipment, so this could be realized as part of future work.

Chapter 3: P3HT

3.1 Introduction

Solution processing of organic semiconductors enables the cost benefits needed to launch organic semiconductor based devices in commercial applications. Among current solution processable semiconductors, poly(3-hexlythiophene) (P3HT) has emerged as a leading candidate for these new applications. P3HT deposited from solution in the right conditions will self align the monomer into polymer chains and the chains into sheets on the substrate.[1,20,21,22,26,56,57,58,59,60] This order results in mobilities on the order of 0.1cm^2/Vs with on/off current ratios in field effect transistors up to 10^8.[25,26,27] Circuits have already been demonstrated that use P3HT based transistors to drive LED and OLED pixels.[2,14,18]

A P3HT monomer is shown schematically in figure 3.1. Upon proper deposition, the molecules will self assemble into a regioregular arrangement, figure 3.2. The regioregular chains are deposited so that the polymer lies on the substrate in a straight line, with other chains lined up next to and on top of it.[3,59] To enable π orbital overlap in the conduction direction (parallel to the substrate), the P3HT is deposited so that the polymer plane is (almost) perpendicular to the substrate plane.[41,42,58] This order allows transport of charge carriers in two dimensions; through the hybridized π orbitals along the chain and across the chains through π orbital overlap.[1,32,60] Currently dip coating creates the highest quality films, however other methods such as drop casting and spin coating can also yield good films.[2,20,21,24,25,26,27,64] Pressure application to this film will

decrease the inter-chain spacing as well as compress the chain, moving the hybridized orbitals closer together.[61]

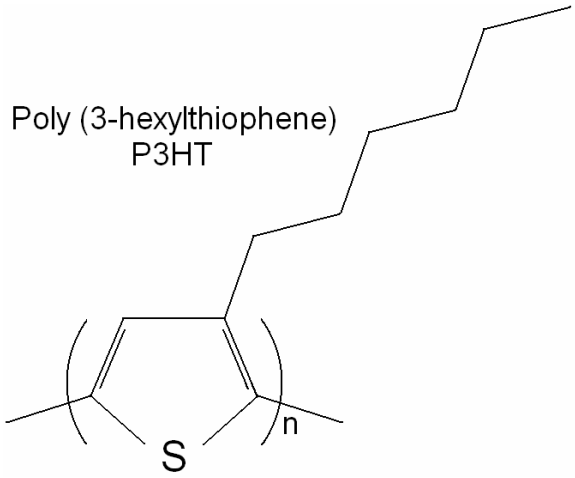

Figure 3.1: Molecular diagram of P3HT.

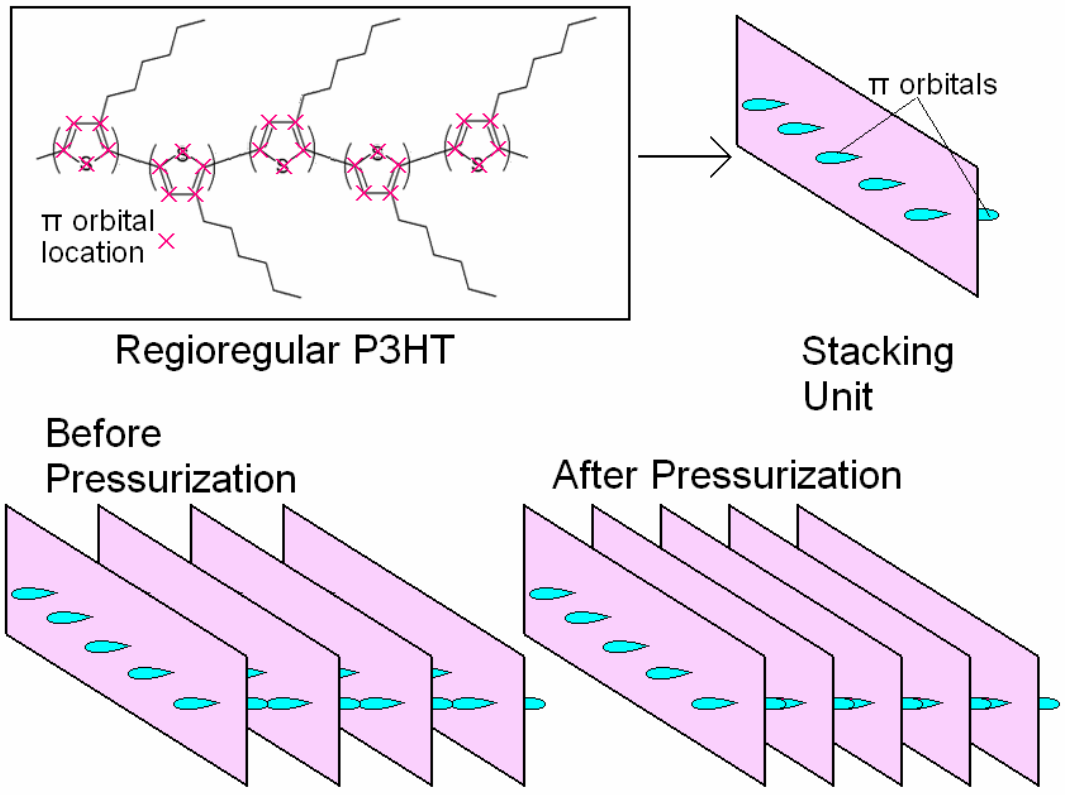

Figure 3.2: Ordering of P3HT. The π orbital depiction in the "Stacking Unit" is not meant to represent the actual location of orbitals. They can also be viewed as the hybridized π orbitals (but still not necessarily at the actual locations).

3.2 Device fabrication

The P3HT films used in the main pressure study are deposited by Prof. Sean Shaheen, formerly of NREL and currently at the University of Denver. The films are deposited on doped silicon wafers with 300nm of thermal oxide. The organic material is purchased from Rieke Metals and used without further purification. The P3HT is dissolved in an o-dichlorobenzene solution at a concentration of 20mg/mL and deposited on a SiO_2/Si substrate by the slow dry technique described by G. Li et al. with 600rpm spin coat deposition. The wet film is allowed to dry in a Petri dish for 30min and then annealed at 80C for 10min under nitrogen, yielding approximately a 100nm thick P3HT film covering the entire surface. The films are then shipped to Mr. Yu Xia in Prof Frisbie's group to thermally deposit gold source/drain pads. This finishes the device with the doped wafer acting as the gate and the SiO_2 providing the gate insulator. A diagram of the device is shown in figure 3.3.

Two other devices are fabricated solely in Prof. Frisbie's lab. The first is similar to the device described in figure 3 except that the P3HT layer is deposited by Mr. Xia through a dip coating method. The other device replaces the gate insulator with an ion gel, fabricated by Dr. Jiyoul Lee and Dr. Jeong Ho Cho in Prof. Frisbie's research group. For this device the P3HT is spin coated on a silicon wafer (which only acts as a substrate). The source/drain contacts are deposited by thermal gold deposition. The insulator is replaced with a mobile ion suspension in a gel, which is placed over the channel. The gate is formed by a copper strip connected to a glass cover slide (to provide extra support to the copper) set on top of the gel and aligned over the channel. These

devices are used to explore variations to the basic pressure response observed in the main part of this study.

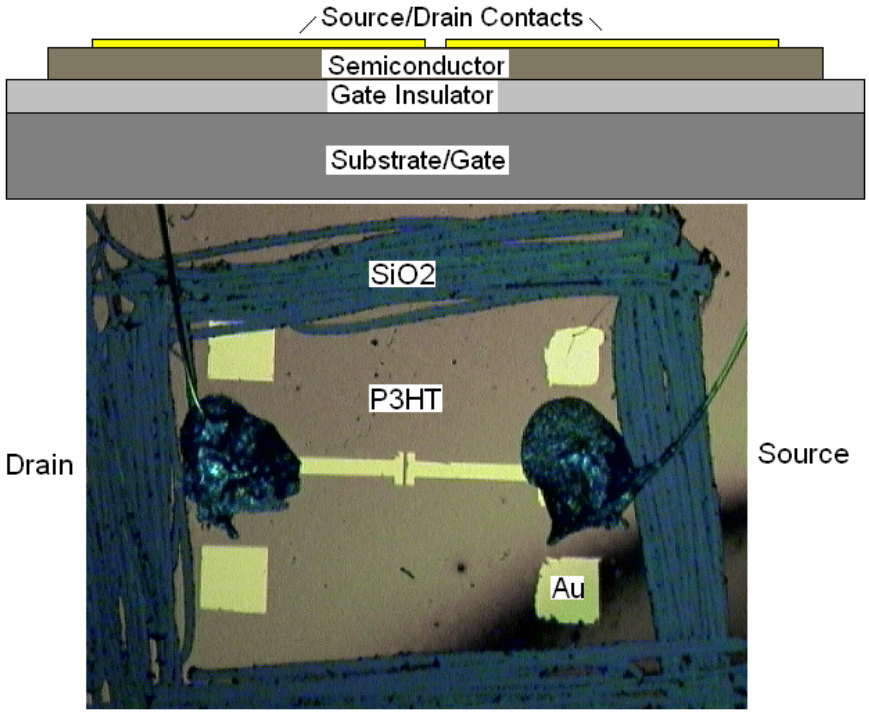

Figure 3.3: The P3HT FET structure and picture of actual device.

3.3 Doping and impurity effects in P3HT films

All three device types show self doping when exposed to the atmosphere. Luckily the dopant is not bound strongly to the P3HT film and is largely released in a pure argon environment. A typical plot of current versus time associated with the dopant loss is shown in figure 3.4. In this plot the current is monitored at a specific bias condition over many hours while in a pure Ar environment. Given this time frame, the device is usually left to dwell in the Ar at atmosphere overnight, then a few I-V traces are taken to ensure that the device is stable. The dopant is assumed to be O_2 as is seen in literature.[62,63,64]

Full plots of the I-V curves taken for some of the data points in figure 3.4 are shown in figure 3.5. The plots show a shifting threshold voltage, from positive voltage to less

positive. This indicates a negative change in threshold voltage, and from equation 1.14 this indicates the addition of positive charges. It is envisioned that O_2 is leaving the film, meaning the oxygen represented a fixed negative charge within P3HT (an electron acceptor type impurity).

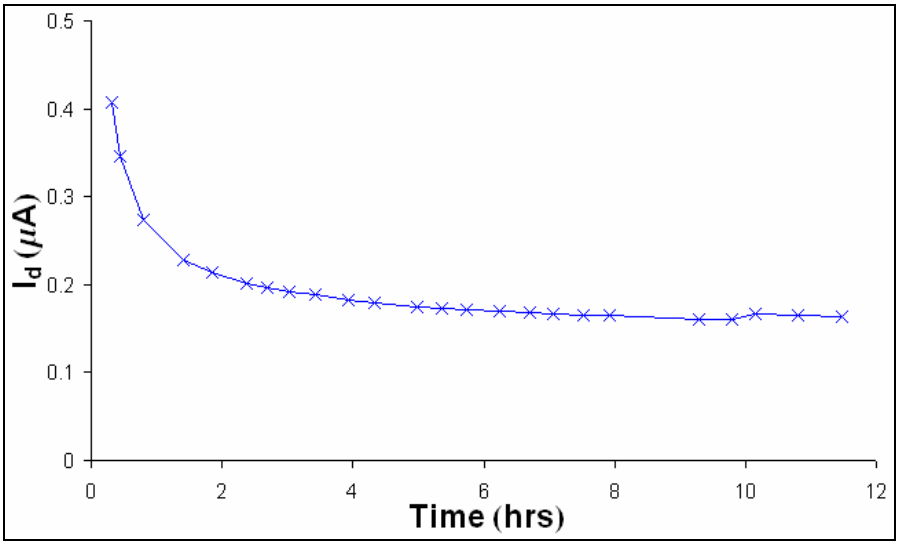

Figure 3.4: Current versus time for a P3HT sample at atmosphere in an argon environment. $V_{ds} = V_{gs} = -40V$.

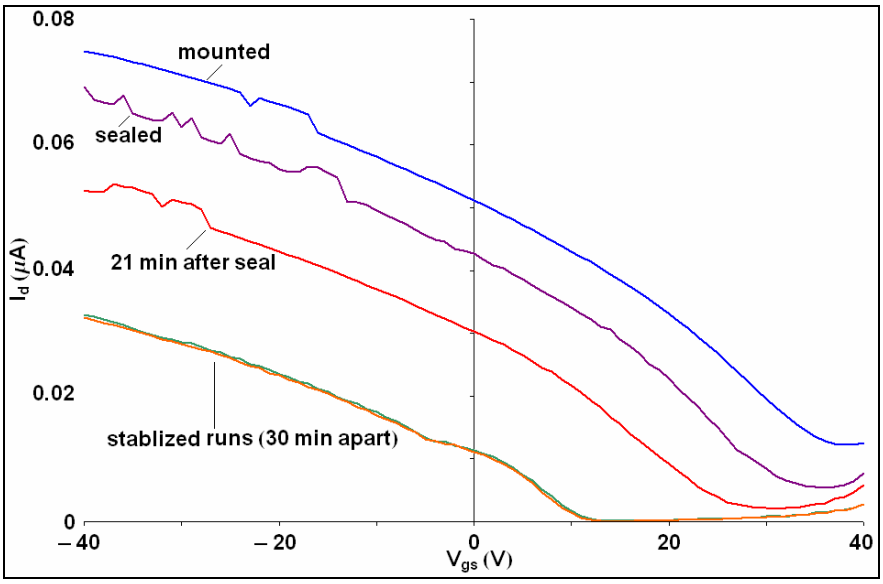

Figure 3.5: Progression of an I_d-V_{gs} curve during the stabilization process depicted in figure 3.4. This plot suggests the threshold shifts from high positive bias to a lower positive voltage. $V_{ds} = -7.5V$.

The need for a stabilization period is not restricted to the initial release of dopants. During the main pressure cycle, stabilization is required at each pressure step. A sample of these dwell step stabilizations is seen in figure 3.6. Initially the currents drop with time, as seen in the 56MPa current set. This is similar to the release of O_2 dopants shown above. The 150MPa data set is seen as a transition point. Beyond 300MPa the currents increase with time, even though the threshold shift is still negative. Throughout the changes the shift is continually negative, indicating the fixed space charge is getting increasingly positive. The change from a decrease in current with time (sub 150MPa) to an increase in current with time, while the threshold voltage shifts in the same direction, indicates a mobility change. The increase in current with increasing time could be the film adjusting to pressure; a kind of mechanical relaxation time. The decrease in current with time could be a bias stress. While both effects occur at each pressure, the pressure change (which controls the mobility change) is smaller for a given time (which will control the bias stress) at the lower pressures as compared to the higher pressures.

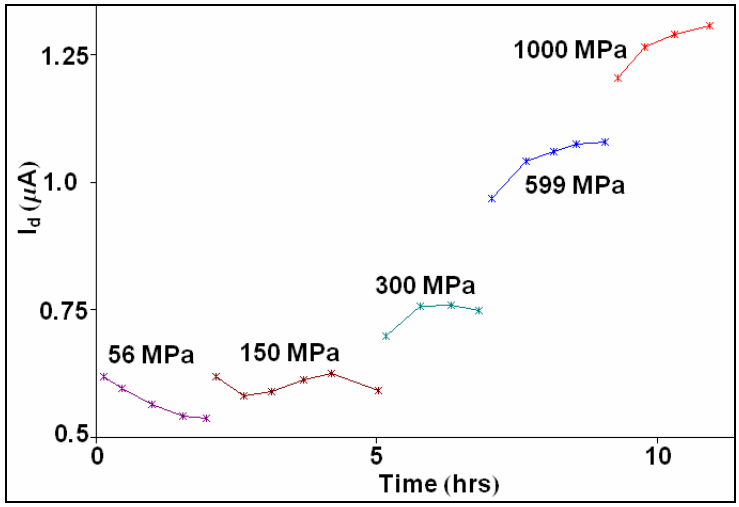

Figure 3.6: Example of stabilization during a pressure run. Data for V_{ds}=-42V and V_{gs}=-30V.

3.4 I-V response to pressure

The samples made with the P3HT deposited by Prof. Shaheen are used to find the basic pressure response for this material. Two samples are presented here to illustrate reproducibility, both samples are nominally identical. This comparison will also help to highlight device response variations that occur randomly from device to device.

During an experiment the pressures are ramped up or down to set points to allow stabilization of the device curves. Upon reaching a desired pressure, an I_d-V_{gs} curve is taken immediately and in intervals of 30min until the curve is stable. Once stable, an I_d-V_{ds} sweep is taken and the pressure is ramped to the next dwell point. During the experiment the current at a particular bias condition is monitored and when this current changes by less than 1% over 30min the device is considered stable. Figure 3.7 shows the traces of current versus pressure. From 50 to about 600MPa the currents increase with pressure as expected for an increasing mobility with increasing pressure. From 600MPa to 1000MPa the currents drop. This drop is due to a shift in the threshold

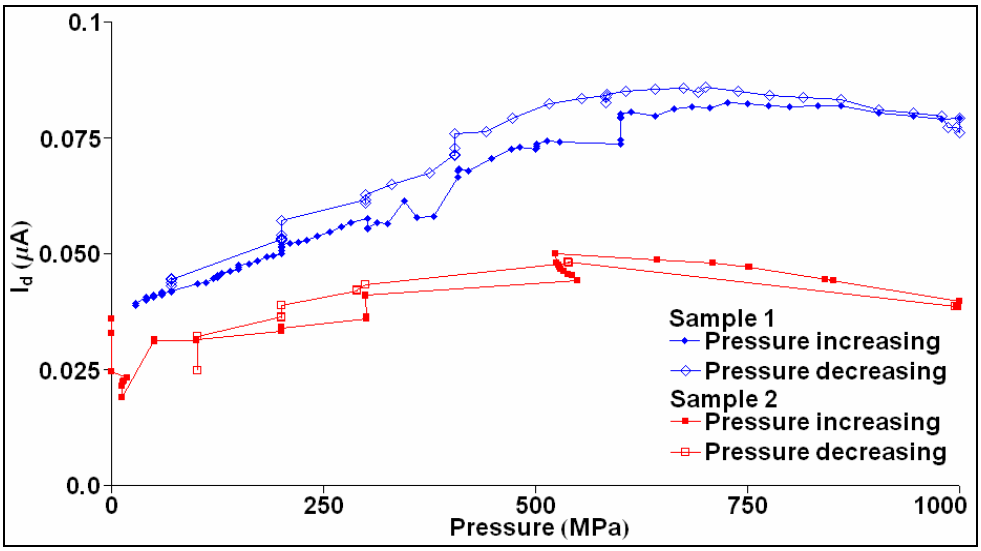

Figure 3.7: Current changes with pressure for a P3HT device. Sample 1 is biased at V_{ds} = -7.5V and V_{gs} = -40V. Sample 2 is biased at V_{ds} = -20V and V_{gs} = -30V. Both curves show peaks around 600MPa.

voltage. The retraces indicates that these samples are able to survive the pressure run.

3.4.1 Mobility response

The mobilities during the pressure cycle are extracted from the linear regime of the I_d-V_{gs} curve. Examples of I_d-V_{gs} curves are shown in figure 3.8. Sample 1 is operated throughout the pressure cycle with V_{ds} = -7.5V. The V_T shifts from +40 to 0V. Sample 2 operates at V_{ds} = -20V. Its V_T shifts from +20 to 0V. A V_{gs} of -40V will give linear FET characteristics. Figure 3.9 shows the mobility extracted from a linear fit to this gate bias at each pressure step. The mobility is found to have an approximately linear response to pressure. On the retrace back to atmosphere, the mobility shows little hysteresis. The

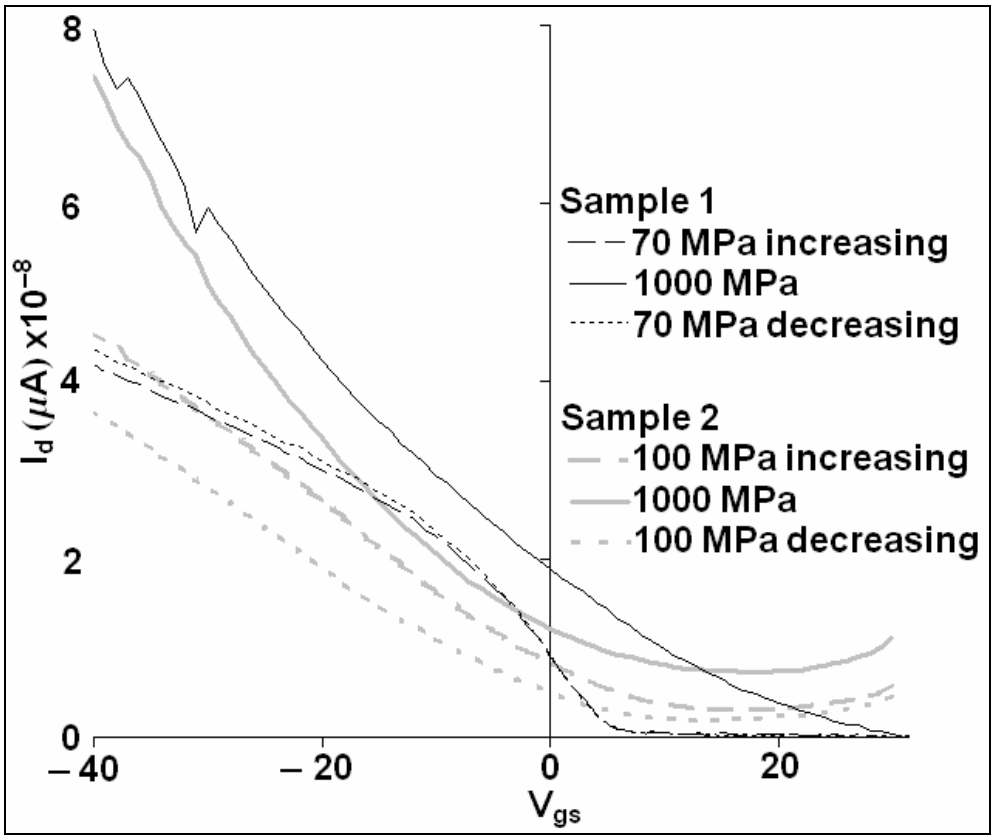

Figure 3.8: I_d-V_{gs} plots for samples 1 and 2. V_{ds} for sample one is -7.5V, for sample 2 it is -20V. The pressure that each curve is taken at is given in the legend.

trend of increasing mobility with increasing pressure is expected from the premise that increased pressure decreases inter-molecular spacing and increases the π orbital overlap. The linear trend that the mobility takes is a little surprising at first glance since the transfer integral from the orbital overlap changes in an exponential manner. However, assuming that the compressibility of P3HT is similar to that of crystalline tetracene, a volume reduction of nearly 10%/GPa, a lattice spacing change of only 3% is expected. A change this small allows the exponential to be well approximated by a linear function.

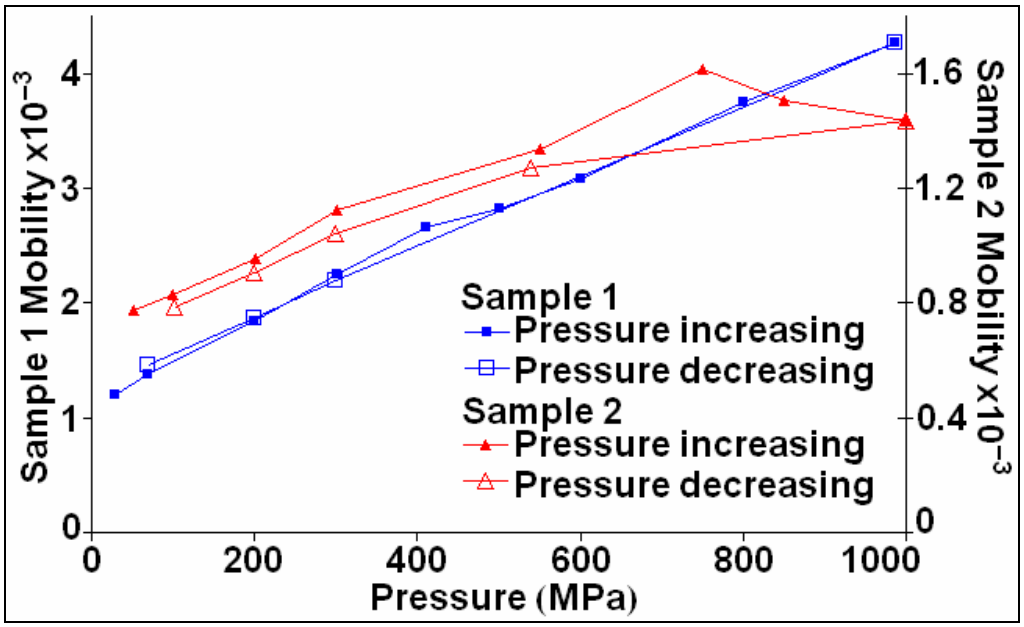

Figure 3.9: Linear mobility versus pressure. Mobility extracted for V_{gs} = -20 to -40V. V_{ds} = -7.5V for sample 1 and -20V for sample 2.

3.4.2 Threshold voltage response

The threshold voltage for the linear region is plotted vs. pressure in figure 3.10. Like the mobility plot, the trend is roughly linear and shows little hysteresis. The change in voltage is negative as pressure increases, which as stated before indicates a loss of fixed electron concentration or a gain of fixed hole concentration. This effect is the main reason why the current in figure 3.7 decreases in the high pressure region. To illustrate

how the linear FET I-V relation can have a curved response to pressure with a linear response in mobility and threshold voltage, the relation is rewritten as:

$$I_D = \frac{W\mu C}{2L}(2(V_{gs} - V_T)V_{ds} - V_{ds}^{\ 2})$$

$$I_D = -\mu V_T(V_{ds}\frac{WC}{L}) + \mu(V_{gs}V_{ds}\frac{WC}{L} - V_{ds}^{\ 2}\frac{WC}{2L}) \qquad \text{Equation 3.1}$$

The product of μ and V_T gives I_d a quadratic response to pressure.

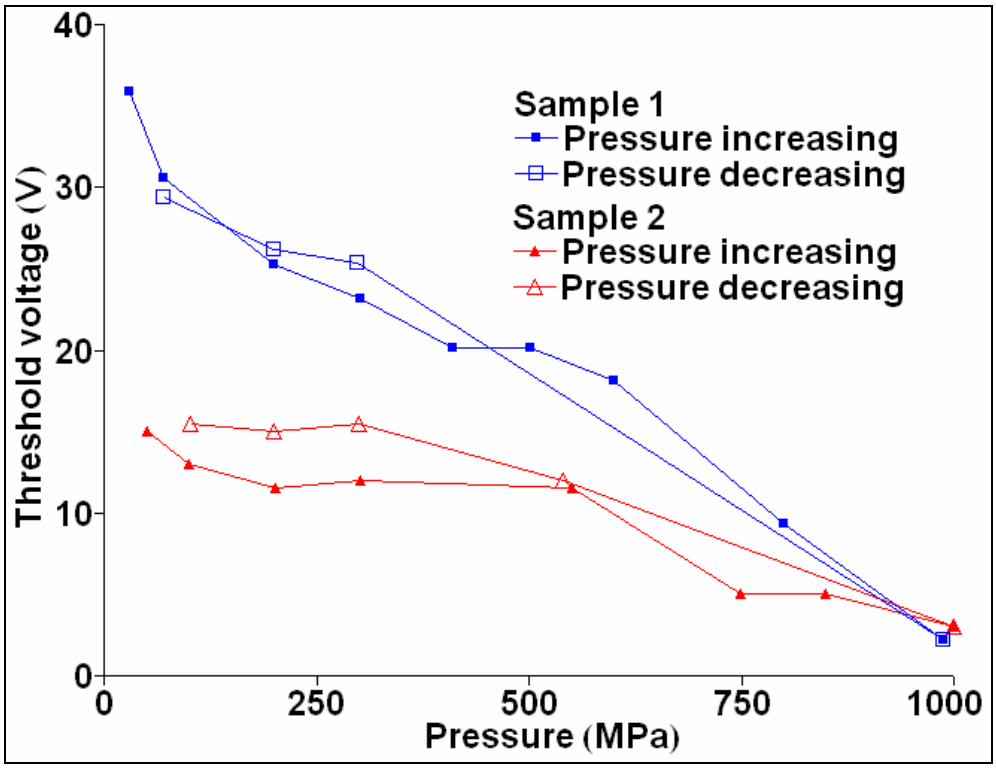

Figure 3.10: Threshold voltages as defined by the linear regions used to extract the mobilities in figure 3.9.

The change in fixed charge is not likely to be due to change in an impurity density, leaving a change in filling/ionization percentage to account for the threshold voltage shift. Using the change in threshold voltage to find the change in charge and attributing that to the traps gives:

$$-\Delta V_T = 20V = \frac{\Delta N_T^{*} t_{ox}}{\varepsilon_{ox}} = \frac{\Delta N_T^{*} (3x10^{-5} cm)}{3.9(8.85x10^{-14} F/cm)} \qquad \text{Equation 3.2}$$

$$\Delta N_T^{*} = 2.3x10^{11} cm^{-2}$$

Within the assumptions made in appendix A, this indicates that the trap and Fermi levels energy spacing decreases with increasing pressure.

3.5 Temperature dependence

As mentioned in section 2.5, the main variation to the experiment that is allowed with the pressure system is the introduction of a cooling bath. A sample similar to the samples made of films deposited by Prof. Shaheen is tested with a slight temperature change.

The sample, prepared entirely by Mr. Xia, differs from the previous samples by using a dip coating method for the P3HT deposition. The device is ramped up to pressure in the same way as in section 3.4, then cooled from room temperature (24C) to 10C, and ramped back down to atmosphere at 10C. The change in temperature represents just over 5% change in thermal energy. The mobility for this device on the ramp up at 24C and the ramp down at 10C is plotted in figure 3.11. The plot shows a systematic shift up in the mobilities in the cooled state. This is interpreted as the P3HT resisting the expansion upon releasing pressure. This is verified by looking at the mobility as the device is cooled at nearly constant pressure, figure 3.12. With varying temperature the change in mobility is very small. The threshold voltage changes by a greater amount with temperature (~5V), which is larger than expected for a pressure of 15MPa (figure 3.10 changes by 0.04V/MPa). The direction of the change is also different from the pressure

induced change already discussed. A decrease in threshold voltage (as argued in appendix A) indicates an increase in positive space charge. A reduction in thermal energy will reduce the likelihood of an impurity to ionize. Increasing a positive space charge while decreasing the amount of ionization, in the simplest case, points to a

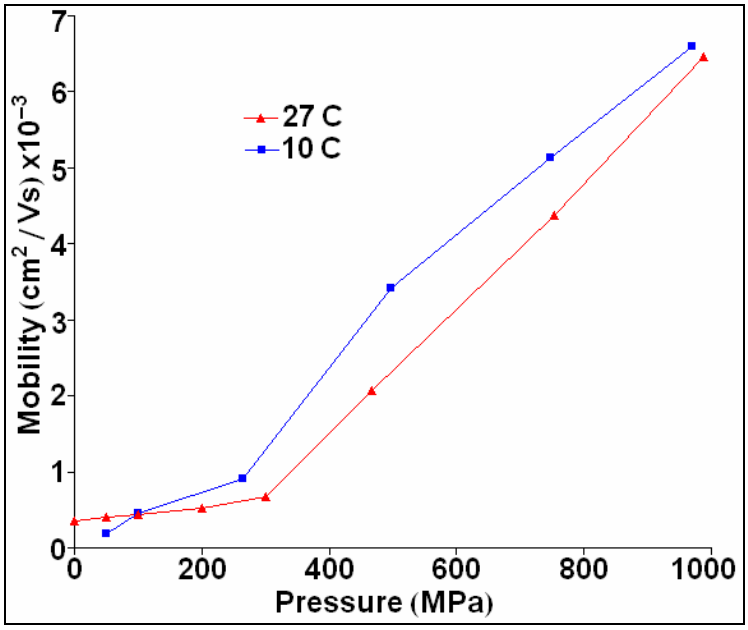

Figure 3.11: Mobility versus pressure for the device at room temperature and at 10C. V_{ds} = -20V. V_{gs} = -40V.

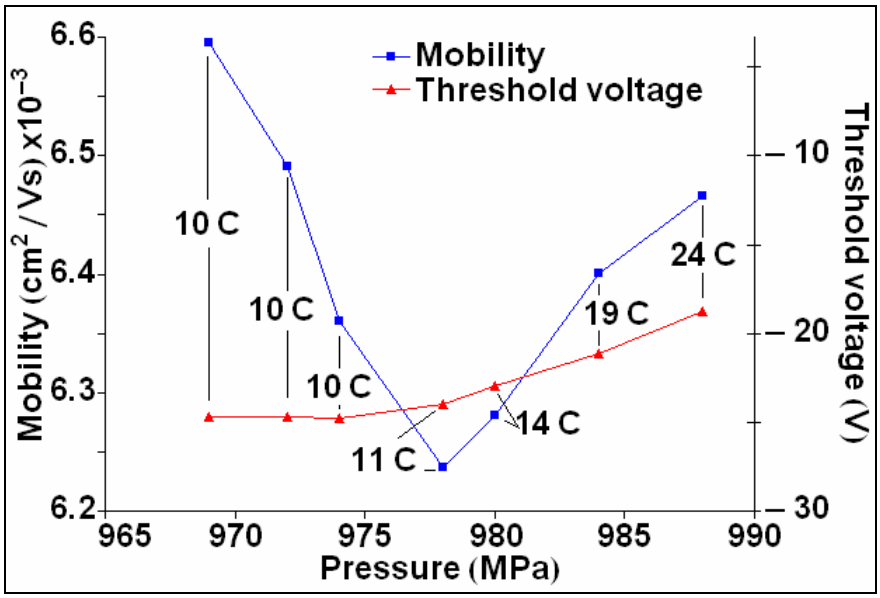

Figure 3.12: Mobility and threshold voltage versus pressure during the cooling of the sample. V_{ds} = -20V. V_{gs} = -40V.

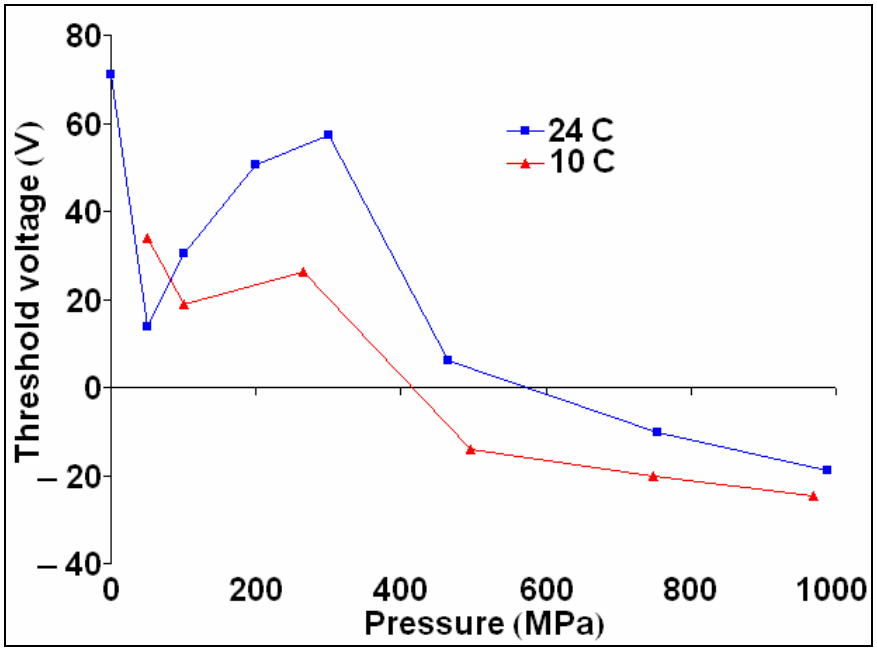

Figure 3.13, Threshold voltage versus pressure for room temperature and 10C. V_{ds} = -20V. V_{gs} = -40V.

donor like impurity. A look at the full threshold trend with pressure and temperature is shown in figure 3.13. The general trend is in the negative direction with increasing pressure like in figure 3.10, but the relation is not linear for this device. While the data shows promise for future temperature studies, more work is clearly required.

3.6 Ion gel device

The final device structure tested using P3HT as the organic semiconductor is a FET using an ionic gel instead of a gate insulator. The ion gel device fabricated by Dr. Lee and Dr. Cho is tested in the same way as the device in section 3.4. The I_d-V_{gs} of the device on the ramp up is shown on the left in figure 3.14 and the ramp down on the right. The device shows a drop in current and mobility as the pressure is increased, the threshold voltage appears to remain relatively constant. Extraction of the mobility is

difficult due to uncertainty in the gel's response to pressure. However, it does demonstrate that the device can be tested under pressure, pointing to a clear possibility for more extensive future work.

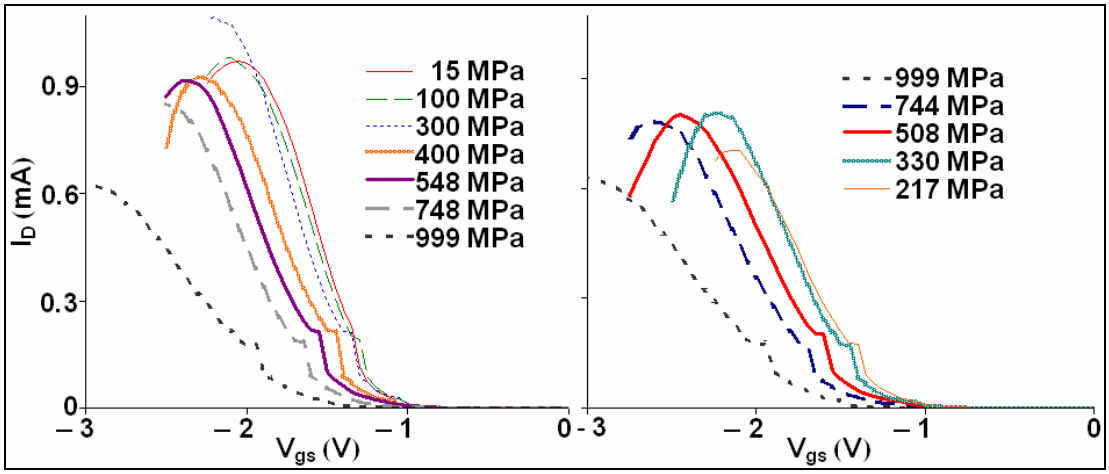

Figure 3.14, I_d-V_{gs} curves under pressure for a P3HT FET made with ion gel. V_{ds} = -2V

3.7 Summary/Conclusion

Subjecting P3HT to hydrostatic pressure results in a clear increase for the carrier mobility in P3HT FETs. The increase of 100-300%/GPa in the mobility is on the order of the increases found by Dr. Rang for thin film pentacene and single crystal rubrene.[53,65,66] Both the mobility and the threshold show good data on the ramp down, indicating that the devices are not permanently altered by the pressure cycle. The increase in mobility is attributed to the π orbital overlap modification and the linear trend is attributed to the small change in inter-molecular spacing. Threshold voltage changes provide evidence that energy levels of impurities in P3HT are shifted with respect to the zero bias Fermi level. Preliminary temperature data suggest that these impurities are donor-like. To further this work, refined temperature studies need to be conducted. P3HT devices made with ion gels are feasible with the present gas pressure system.

Chapter 4: Pentacene thin films

4.1 Introduction

Pentacene thin film field effect transistors are among the most studied organic semiconductor devices in literature. Pentacene shows great promise as an organic material, with crystalline devices reaching mobilities of 30cm^2/Vs. Typical pentacene based FETs are thermally evaporated onto SiO_2 surfaces with possible surface treatments to improve the order of the film.[5,7,29,30,67,68,69,70,71,72] Recent progress has been made with solution depositions using a pentacene based molecule. Given this interest, pentacene is one of the few types of organic semiconducting materials to be tested previously under hydrostatic pressure.[43,50,51,53,66,73,74]

Dr. Zhenlin Rang reports on two thin film pentacene FETs that he tested in a liquid pressure system. One device's mobility changed from 0.13cm^2/Vs to 0.17cm^2/Vs over 300MPa and the other changed from 0.017cm^2/Vs to 0.067cm^2/Vs over 600MPa. The changes are found to fit a linear relationship with reasonable agreement. If the results are extrapolated to 1GPa, the devices would show mobility increases of about 100% and 500%. The threshold voltages observed in these devices display only minor dependencies on pressure; the changes did not exceed 3V while biased with $V_{ds} = V_{gs} =$ -40V. This would represent a 3.5x10^{10}cm^{-2} change in carriers as figured in section 3.4, an order of magnitude less than in P3HT thin films. While these results have good retrace data (the data taken when reducing the pressure agrees with the data taken when increasing pressure) the samples themselves have an order of magnitude difference in mobility and a 5x change in pressure response. Dr. Rang's use of a liquid system, with

hexane/pentane as the pressure transmitting fluid, requires protection of the samples from the liquid. The added processing steps in protecting the samples could alter the pentacene devices. By using a gas pressure system the protection steps, and any impact they may have on the devices, can be avoided.

4.2 Device fabrication

The standard pentacene devices used in this project are field effect transistors (FETs) fabricated in Prof. C. Daniel Frisbie's research group. The FETs are constructed of heavily doped silicon wafer pieces with thermal oxide, thermally evaporated pentacene, and thermally evaporated gold source/drain contacts. The doped silicon is conductive enough to act as the gate as well as a substrate. Contact to the gate is accomplished by back side metallization, typically with Al. The thermal oxide (300nm thick) is used as the gate insulator. The pentacene is thermally evaporated on the oxide. Source and drain contacts are thermally deposited on to the pentacene through shadow masks with a 10:1 width to length ratio. The pentacene layer thickness and substrate temperature are changed throughout the experiment so these values will be listed separately.

The FETs used in this project were fabricated by Dr. Sandra Fritz-Vos and Mr. Yan Liang. The sample from Dr. Vos was fabricated for testing two years before the refinements to the pressure cycle explained in section 2.2.1 were implemented, then used as an equipment test once the new pressure cycle was adopted. The samples from Mr. Liang were fabricated just prior to experimentation. The data recorded while testing Dr. Vos's sample was considered good for a pentacene FET, motivating experiments to be

pursued using Mr. Liang's devices. Mr. Liang's initial devices did not respond as well as Dr. Vos's sample to the pressure applied, so subsequent samples were fabricated by Mr. Liang to try and recreate Dr. Vos's sample, see table 4.1 for the relevant parameters.

Sample Name:	Fabricated by:	Pentacene thickness:	Substrate temperature during fabrication:
A	Dr. Vos	16nm	60C
B	Mr. Liang	30nm	No heating
C	Mr. Liang	15nm	No heating
D	Mr. Liang	15nm	40C
E	Mr. Liang	15nm	60C

Table 4.1: The pentacene samples and their controlled differences.

In addition to the FETs, a new device structure developed and fabricated by Mr. Liang is tested in the pressure system. This device consists of a pentacene strip on top of 300nm SiO_2 with heavily doped silicon beneath. There is a gold electrode connected to the pentacene on the end of the strip. The structure forms a semiconductor-oxide-metal capacitor (with the heavily doped Si acting as the metal). This device allows the channel carriers entering and exiting the device to be measured directly by monitoring the currents entering end exiting the gold electrode. More on this device will be presented in section 4.4.

4.3 FET response to pressure

By testing the pentacene FETs in a gas pressure system, the complications found by Dr. Rang with the hexane/pentane pressure medium are avoided. However, while optical checks, AFM imaging, and x-ray analysis show no appreciable change in the pentacene layer with applied pressure in the gas system (presented in Appendix B), the devices are inconsistent in their pressure response. As mentioned, the sample by Dr. Vos (sample A)

shows a good retraceable pressure response. Sample A has an approximate 100% increase in mobility with 1GPa of applied pressure and only a 5V shift in threshold voltage, comparable with the results found by Dr. Rang. The other samples listed in table 4.1 show a peak in mobility increase with pressure around 100MPa; sample A shows a knee at 100MPa where the increase slows but still continues. The threshold voltages for these samples also change more than for sample A, with at least a 5V change in this first 100MPa followed by a slower change.

The I_d-V_{gs} curves for three samples (A – left scale, B and D – right scale) at the start and the end of the pressure run are shown in figure 4.1. The characteristics do not change drastically. Sample A has an improved mobility and similar threshold voltage after pressure is applied. Sample B shows some of the worst degradation with pressure after the 100MPa limit is reached, yet the device still shows a current response after pressure of 75% of the pre-pressure value. Sample D is a sample that retraced well after reaching a peak pressure of 300MPa (the same peak pressure as sample B but only 30% of the pressure applied to sample A) but also shows shifts in threshold voltage and a reduction in mobility. The hysteresis shown in the data for sample D is interpreted as trapped charges modulating the I-V response. The increase in hysteresis after pressure indicates an increase in trapped charge density. Plots of the three samples' mobility and threshold voltage are shown in figures 4.2 and 4.3, data for all of the samples are provided in appendix C.

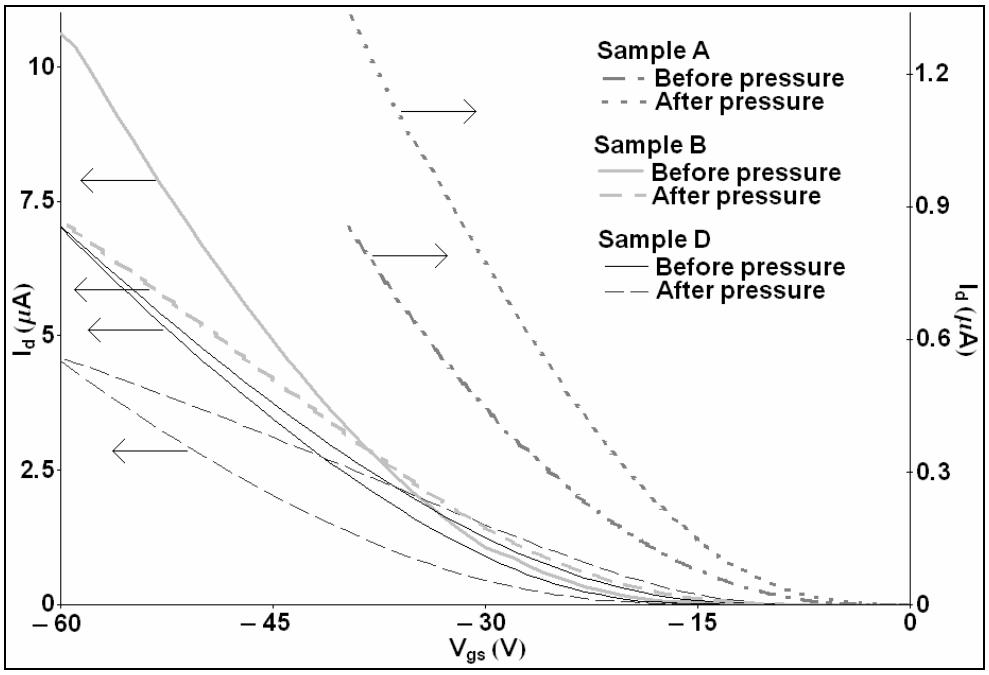

Figure 4.1: I_d-V_{gs} at atmospheric pressure while sealed in the pressure system. The pre- and post-pressure data are shown to indicate changes in the FET data incurred during the pressure cycle. Sample A V_{ds} is -10V, B → -25V, and D → -15V.

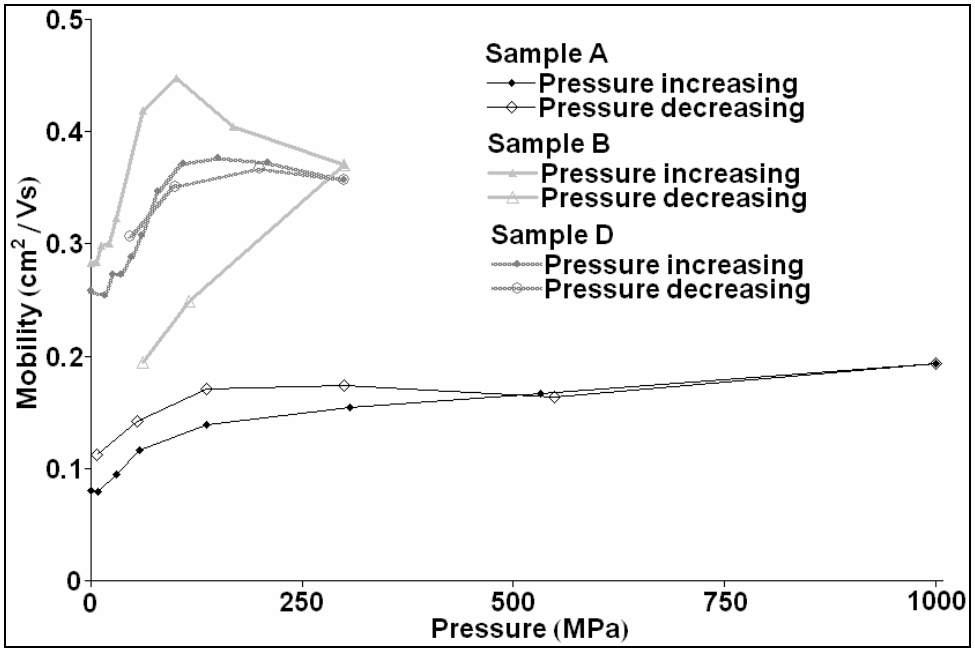

Figure 4.2: Mobility versus pressure for devices A, B, and D. V_{ds} for sample A is -10V, B → -25V, and D → -15V. V_{gs} for sample A is -40V, B → -60V, and D → -60V.

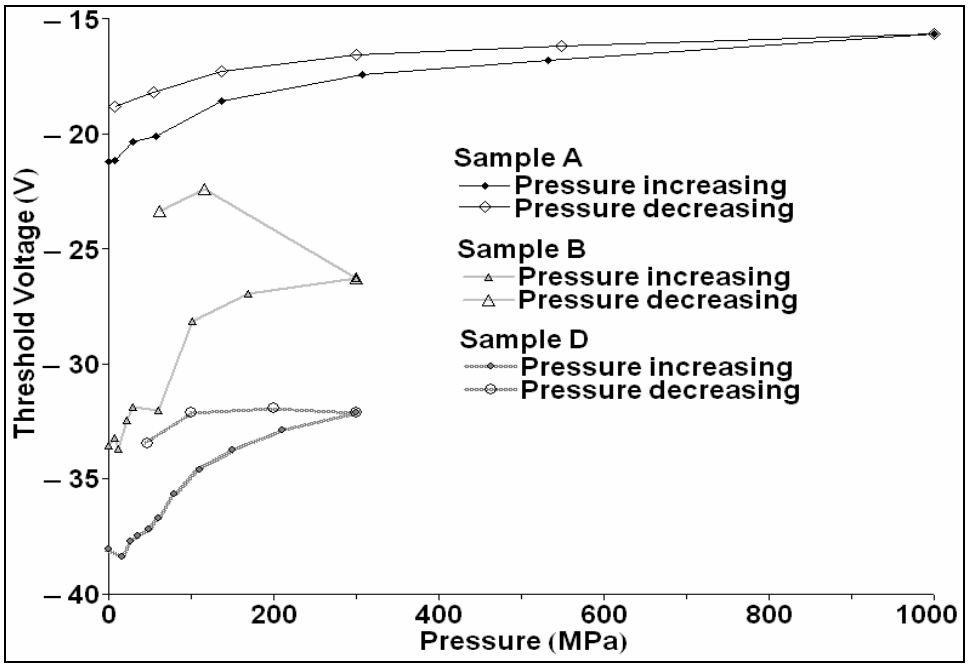

Figure 4.3: Threshold voltage versus pressure for devices A, B, and D. V_{ds} for sample A is -10V, B → -25V, and D → -15V. V_{gs} for sample A is -40V, B → -60V, and D → -60V.

The lack of a consistent pressure response in the pentacene FETs places uncertainty on the meaning of the data presented in this section. None of the samples tested exhibit the linear mobility response with pressure that was found by Dr. Rang. Sample A is comparable in total change in mobility and threshold over 1GPa but most of that increase in mobility is in the first 100MPa. The initial threshold voltages are also quite different (-20V here versus +5V). In each device tested, the majority of the mobility increase and the threshold voltage change occur in the first 100MPa. Beyond 100MPa the mobility increase slows and (except in sample A) begins to degrade. As seen in figure 4.2, sample D is able to retrace at a pressure that in sample B caused irreversible changes. In sample E (shown in appendix C) the sample is pressurized to 1GPa but also retraces irreversibly, indicating that while the threshold for degradation in the samples is shifted to higher pressures as the device iterations in table 4.1 progress, it is still present within 1GPa.

4.4 Semiconductor-oxide-"metal" capacitor

The semiconductor-SiO_2-metal capacitor (with doped Si acting as a metal) was developed as a way to measure the charge carriers injected into the FET channel in an organic semiconductor FET. The basic behavior of the device is governed by:

$$I = \frac{dQ}{dt} = \frac{d(CV)}{dt} = \frac{dC}{dt}V + C\frac{dV}{dt} = \frac{dC}{dt}V + Cr_v \qquad \text{Equation 4.1}$$

The current (I) is measured and the voltage sweep rate (r_v) is applied to the device. The capacitance (C) is the capacitance of the SiO_2 under the pentacene strip and metal electrode. As equation 4.1 demonstrates, the experiment will look at the transient state of the capacitor. A schematic of the device is shown in figure 4.4.

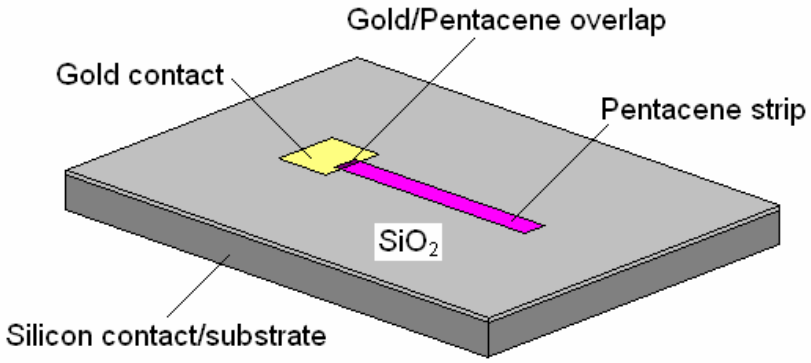

Figure 4.4: Layout of the capacitor device. The silicon/SiO_2 substrate is the same as the type used in the OFET fabrication described before. The pentacene is deposited 30nm thick. The total strip is approximately 0.5x5mm.

As the device is biased and the channel forms, carriers flow from the gold electrode into the pentacene strip. The carriers take some time to reach the end of the strip, this time allows for a measurement of the mobility within the film. The total injected carrier number can be calculated by integrating the measured current with respect to time, which can be converted into a voltage via the sweep rate. Similarly, the extracted carrier

number is found during the channel annihilation. A measure for the trap sites that do not release trapped charge carriers within the time span of one voltage cycle is obtained by subtracting the extracted carrier number from the injected; with the remaining carriers still trapped in the device. A typical measurement is shown in figure 4.5. The currents in figure 4.5 can be separated into a gold to Si capacitor displacement current level (this is a constant value) and a pentacene to Si current, as is roughly shown.

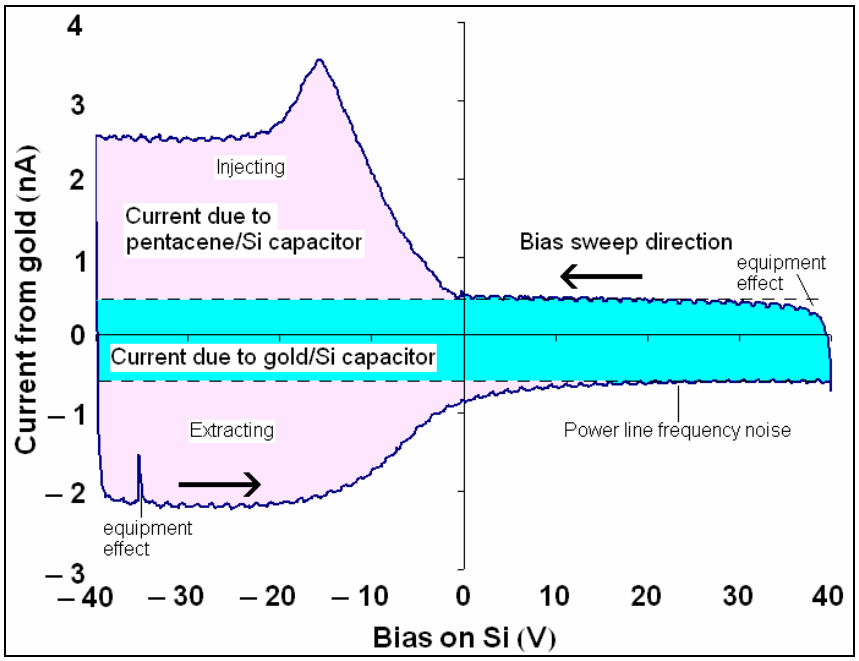

Figure 4.5: A typical I-V response from the device shown in figure 4.4.

In a high mobility semiconductor the current relation would look much more like a step function. Before the channel is formed the current would be constant as determined by the electrode area forming a capacitor, after channel formation the current is again constant but determined by the full electrode/semiconductor area. These two levels are present in figure 4.5 but there are also other features; most notably the slope in current when the channel begins to form, the peak in current during channel formation, and the slope between high current and low current during channel annihilation.

The slope and peak in current during channel creation are explained with a simple analytic model in section 4.4.1. The slope in current during channel annihilation is formed by the release of shallow traps after the free carrier charge is removed from the device. If this were the only effect the start of the current decrease slope should shift to 0V (i.e. the threshold voltage for channel formation) but the presence of trapped charges cause a shift from that voltage in the same way as the shift in threshold voltage described in section 3.4. A sampling of current curves during the pressure run is shown in figure 4.6. The location of the channel annihilation slope moves to the left and right according to the slow release trap counts measured in figure 4.10. The trap response to pressure in these devices may appear to be different from that formed in the pentacene FET measurement. However, differences are expected as transient measurements in this

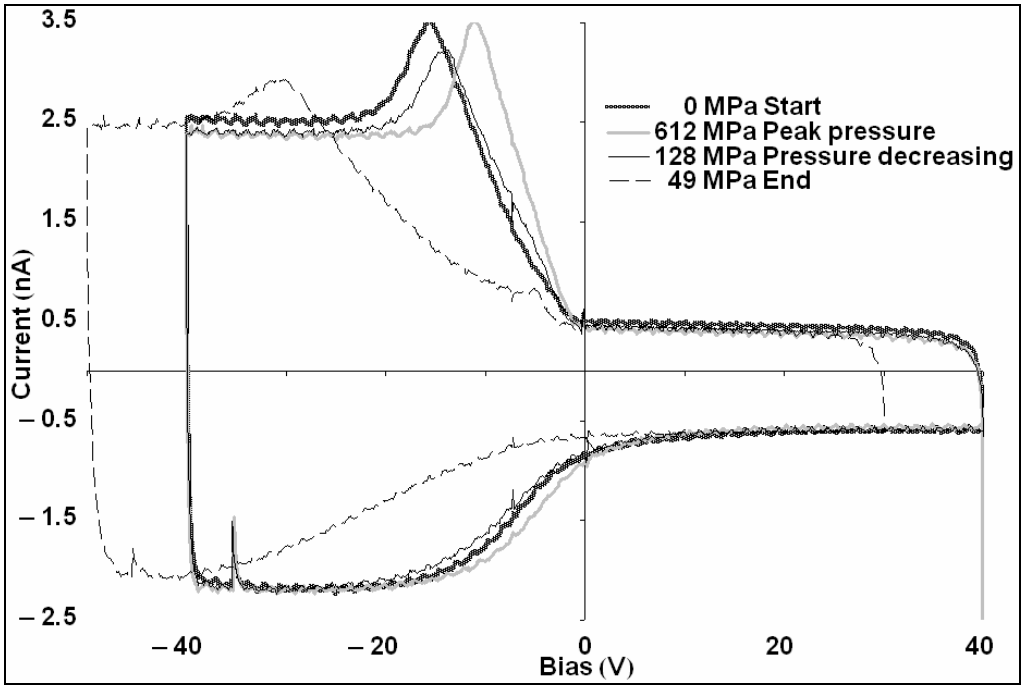

Figure 4.6: Current curve of the capacitor device during the pressure run. The curve for 49MPa is swept in voltage from +30V to -40V due to the lowering of the creation and annihilation slopes, the change in voltage is chosen to keep the same span in voltage and therefore the same time for one voltage sweep.

section and the FET output and transfer characteristics of the prior section probe different time scales.

4.4.1 The analytic model

The channel creation slope and peak in current are an effect of the slow mobility in this device (1 to 0.1cm^2/Vs). To illustrate how the slope and peak form, an analytic model is presented here; a more complete numeric model developed by Mr. Hsui-Chuang Chang is presented in Mr. Liang's paper on this device.[75] This model will assume an ideal contact; one that is ohmic, has no area and therefore no capacitance, and has an unlimited free carrier concentration to inject into available states in the semiconductor. The semiconductor will be assumed devoid of traps and impurity sites. The time scale, which is convertible into a voltage scale by the sweep rate parameter, is set to zero at the moment where the channel first starts to accept injected charge.

At $t = 0$ the carries will start to flow into the channel, but more carriers will be allowed in while the previous carriers move to the end of the pentacene strip, creating an increasing current. When the first carriers to be injected reach the strip's end ($x = L$), the channel's accessible free carrier sites will be half filled. To fill the other half, the carrier rate of increase will continue until a the initial carriers reach a value of two times the strip length, or a time of $2L/(\mu_p E)$. After this time the carrier profile will be uniform across the channel, lowering the current needed to add new carriers. This is shown schematically in figure 4.7 and will be shown to create a current plot like figure 4.8. The speed of the initial carriers is $\mu_p E$, where μ_p is the hole mobility and E is the electric field along the channel. The contact voltage changes at a constant rate of r_v.

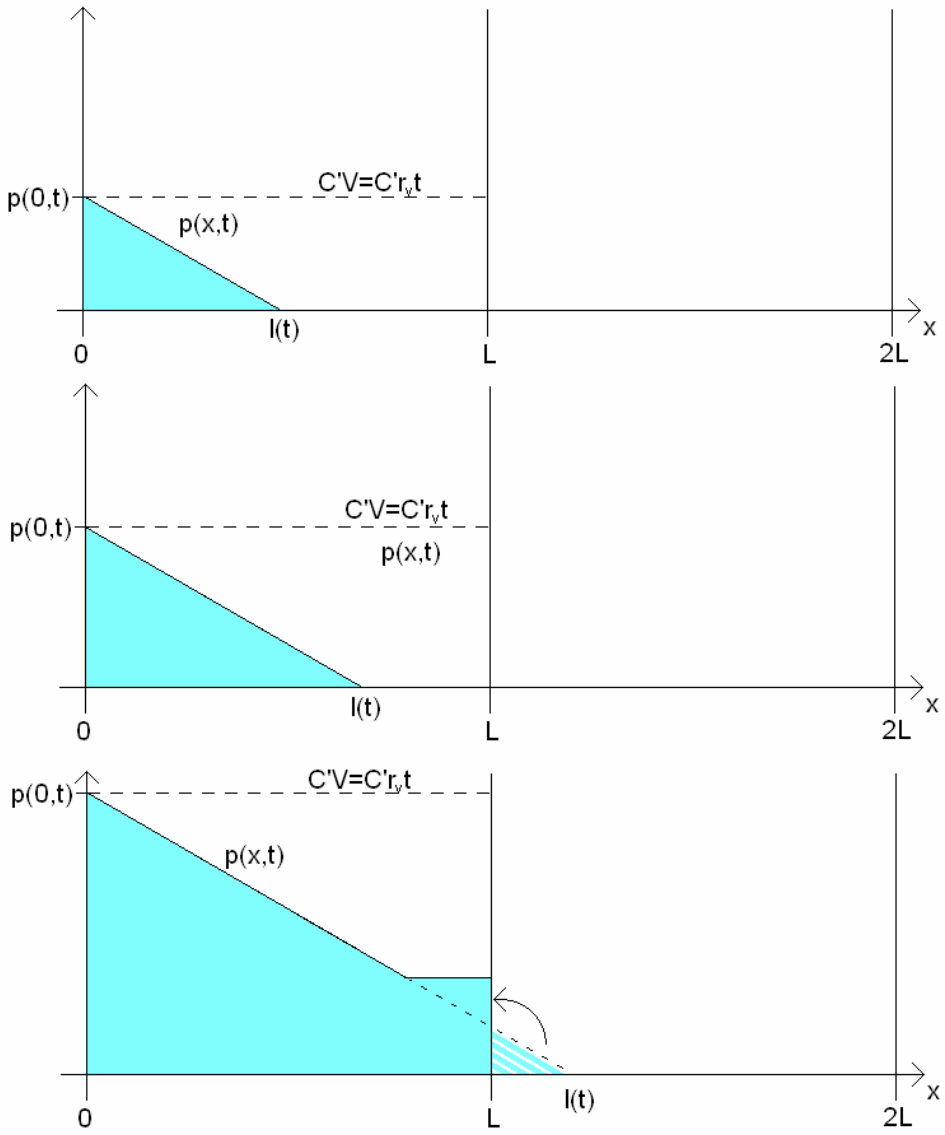

Figure 4.7: Carrier profile for the simple model. Top figure shows an early profile. Middle figure shows how the profile grows with time. Bottom figure shows how the profile changes once the carriers reach the end of the strip. p(x,t) is the carrier profile in the strip. *C*' is the capacitance per unit width of the pentacene strip. *l*(*t*) is the length the initial carriers will travel at time t.

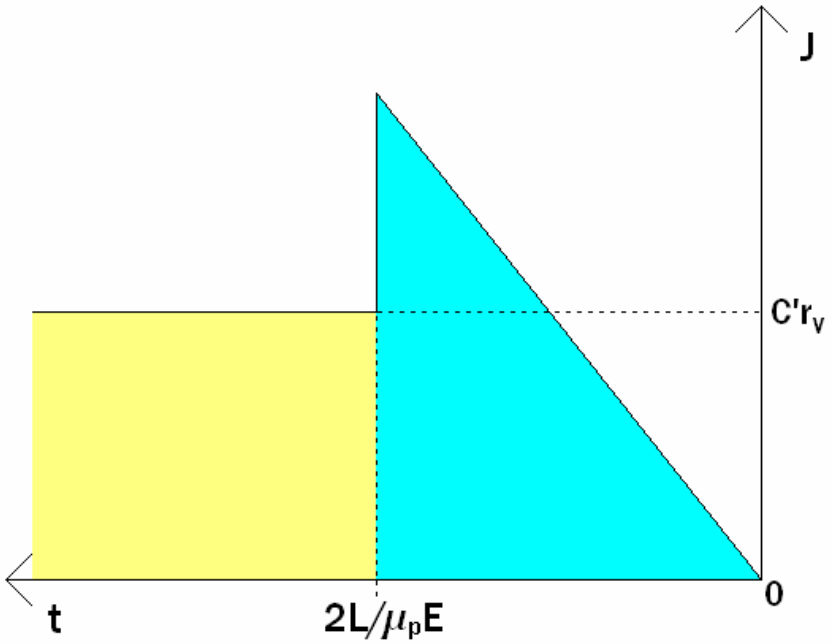

Figure 4.8: The current response for the model presented in figure 4.7. The time scale is inverted to allow better comparison to figure 4.5. The numerical model presented in reference 75 smoothes out and lowers the peak. *J* is the current per unit width of the strip.

Using this geometric analog, an analytic model can be formulated. Starting with the basic definition of the current:

$$I = WJ = eW\frac{\partial N(t)}{\partial t} \qquad \text{Equation 4.2}$$

W is the width of the strip; e is the carrier charge; $N(t)$ is the total number of carriers in the pentacene per unit width. Using the profile shown in figure 4.7, $p(0,t)$ can be written as:

$$p(0,t) = \frac{C'V}{e} = \frac{C'}{e} r_v t \qquad \text{Equation 4.3}$$

and $l(t)$ as:

$$l(t) = \mu_p E t \qquad \text{Equation 4.4}$$

$p(x,t)$ can be written as:

$$e\,p(x,t) = Q(x) = C'V(x)$$
$$p(x,t) = \frac{C'}{e}V(x) \qquad \text{Equation 4.5}$$

$Q(x)$ is the charge profile per unit width. $V(x)$ is the voltage between the channel and the silicon wafer, although only the voltage in the channel depends on x. This allows the field parameter in equation 4.4 to be defined by the Poisson equation:

$$E = -\frac{\partial V(x)}{\partial x} = -\frac{e}{C'}\frac{\partial p(x,t)}{\partial x} \qquad \text{Equation 4.6}$$

The derivative of $p(x,t)$ with respect to x is merely the slope of the profile seen in figure 4.7. Given that this profile is linear the slope can be defined as:

$$\frac{\partial p(x,t)}{\partial x} = -\frac{p(0,t)}{l(t)} = -\frac{C'}{e\,l(t)}V(t) = -\frac{C'}{e\,l(t)}r_v t \qquad \text{Equation 4.7}$$

This allows the length $l(t)$ to be written as:

$$l(t) = \mu_p E\,t = \mu_p\left(-\frac{e}{C'}\frac{\partial p(x,t)}{\partial x}\right)t = \mu_p\left(-\frac{e}{C'}\left(-\frac{C'r_v t}{e\,l(t)}\right)\right)t$$
$$l(t) = (\mu_p r_v)^{1/2}t \qquad \text{Equation 4.8}$$

And a final $N(t)$ as the integral of the triangle in figure 4.6 (extending to $2L$ when necessary):

$$N(t) = (1/2)\,p(0,t)\,l(t) = (1/2)\left(\frac{C'}{e}r_v t\right)\left((\mu_p r_v)^{1/2}t\right)$$
$$N(t) = (1/2)\frac{C'}{e}\mu_p{}^{1/2}r_v{}^{3/2}t^2 \qquad \text{Equation 4.9}$$

Beyond $t = 2L/\sqrt{(\mu_p r_v)}$, the time for the carriers to reach $2L$ according to equation 4.8, $N(t) = p(0,t)L$. The square dependence on time in equation 4.9 used in equation 4.2 creates the linear current in figure 4.7; the linear dependence beyond $t = 2L/\sqrt{(\mu_p r_v)}$ creates a constant current. Explicitly, these currents are given by:

$$J(t) = C'\mu_p^{1/2} r_v^{3/2} t \quad for\ t < \frac{2L}{\sqrt{\mu_p r_v}}$$
$$J(t) = C' r_v L \qquad for\ t > \frac{2L}{\sqrt{\mu_p r_v}} \qquad \text{Equation 4.10}$$

As can be seen in these equations, the linear (in time) current rises to two times the value of the constant current at the time $t = 2L/\sqrt{(\mu_p r_v)}$ then falls discontinuously to $C' r_v L$. This model exemplifies how the mobility in the film can be extracted by monitoring the slope of the current during channel formation before the peak. The model also explains the presence of a peak but is too simple to describe it accurately. The model presented by Mr. Chang is able to describe the peak and slopes (both in channel creation and annihilation) and confirms the channel creation slope dependence on the square root of the mobility.

4.4.2 Pressure response

By reworking equation 4.10, a simple approximation for the mobility can be found as:

$$I(t) = C\mu_p^{1/2} r_v^{3/2} t = C\mu_p^{1/2} r_v^{1/2} V(t)$$
$$\frac{I(t)}{V(t)} = slope = C\mu_p^{1/2} r_v^{1/2} \qquad \text{Equation 4.11}$$
$$\mu_p = \left(\frac{slope}{C r_v^{1/2}} \right)^2$$

C is the total capacitance of the oxide under the pentacene strip. The channel creation slopes are measured and plotted versus pressure in figure 4.9. The mobility based on equation 4.11 is also plotted (right side scale). The slopes and mobility both appear to

increase in a linear fashion after the 100MPa mark is reached. While the simple model shows a linear slope change translates into a quadratic mobility change, the change is small enough that this mobility plot still looks approximately linear. Looking at the mobility plotted in figure 4.9 and using a linear relation (like in Dr. Rang's paper) a mobility change of around 300% in 600MPa, or a little more than 500% over 1GPa, is on the high end of (but within) Dr. Rang's findings.

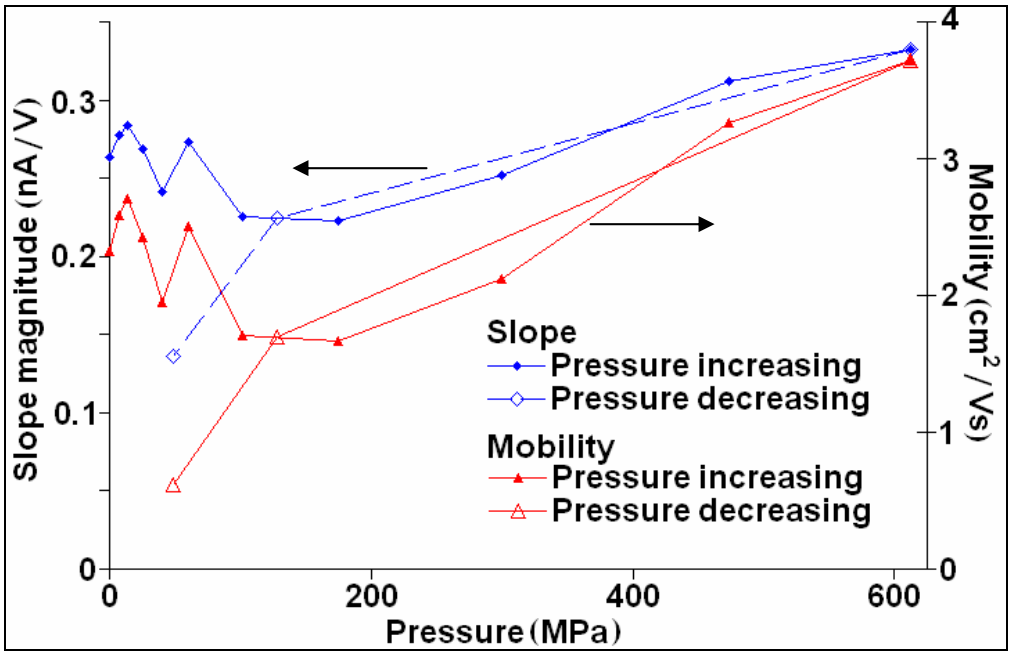

Figure 4.9: Slope and mobility versus pressure plot. Slopes are plotted on the left side, mobility on the right.

The results of integrating the currents to extract the number of carriers injected, extracted, and trapped versus pressure are shown in figure 4.10. A slight increase is seen in the total number of carriers injected and extracted. A mobility increase with pressure does not account for this phenomenon, the mobility will only fill the allowed states more quickly, not create them. Examining the constant current region of figure 4.5 (after the channel creation peak) with changing pressures gives figure 4.11. There is a slight

change, a decrease, with pressure. Looking at equation 4.11, none of the current parameters should change significantly with pressure. These changes are examined by Mr. Chang with the more complete numerical model. The result of his study shows that the injecting current has a small but long tail beyond the prominent peak. As the mobility increases and the carriers fill the channel faster, the tail shortens, lowering the "constant" current beyond the peak. The reduction of the tail by the carrier sites filling faster means the integration of currents will allow more of the carriers to be counted.

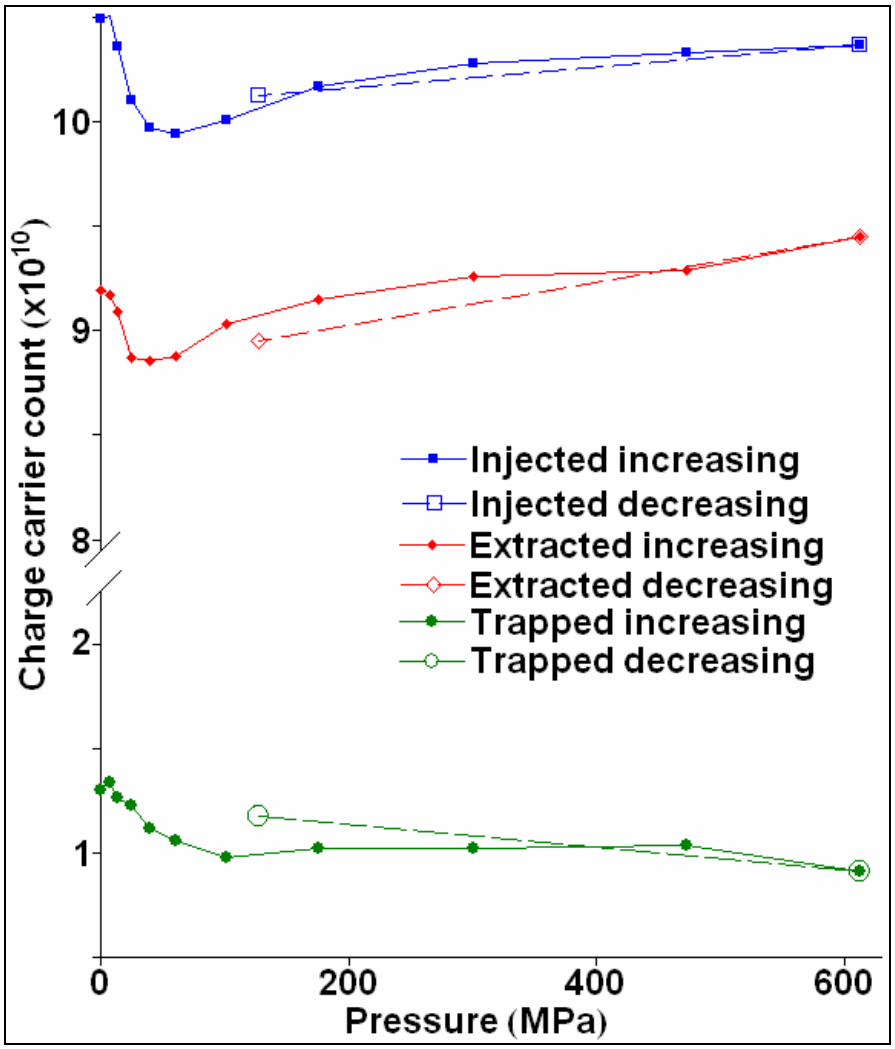

Figure 4.10: Number of carriers versus pressure plot. Trapped carrier count is simply the difference between the injected and extracted carrier totals.

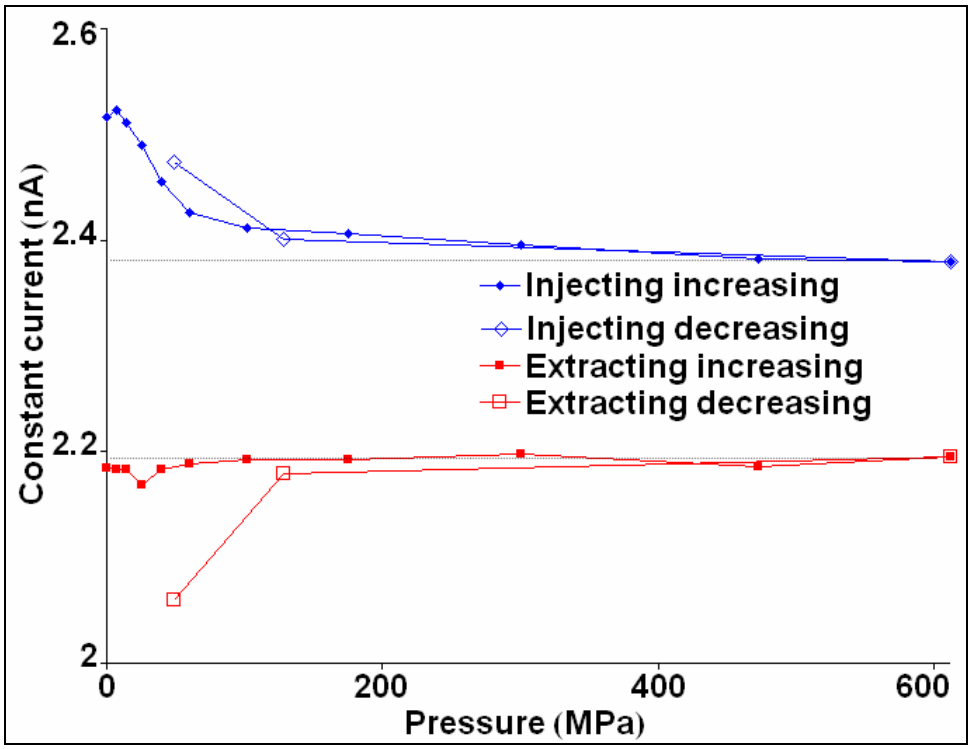

Figure 4.11: Plot of the capacitor current with a fully charged channel versus pressure. The extracting current curve is rectified by taking the negative of the measured value.

Charges populating slow traps can be found by subtracting the injecting and exiting number of carriers. The number of trapped carriers is essentially constant above 100MPa. The carrier injection and extraction numbers match the data found by Mr. Liang, however the trap level is higher here. It is likely that the difference in trap level is due to Mr. Liang measuring his devices in a vacuum environment while this device is measured in an Ar environment after being exposed to air.

4.4.3 Capacitor summary

This pentacene capacitor device structure shows a well behaved response to pressure. All parameters measured retrace well, indicating that the device does not

undergo irreversible changes during a pressure cycle. The mobility in figure 4.9 shows a roughly linear response to pressure, an increase that extrapolates to over 500% in 1GPa. The threshold voltage, as extracted from the onset of the slope monitored in figure 4.6, is found to remain roughly constant. A second threshold associated with channel annihilation does change slightly with pressure. This change is interpreted as a change in the charge state of trap levels. The lack of change in the channel creation threshold voltage indicates that the trapped charges measure in figure 4.10 release in the (minimum) 30min of time between measurements. This may also suggest that the threshold voltage changes seen in the FETs fill traps from the sub-threshold current between the source and drain. In the capacitor device (without a drain to source current) the trapped charge comes from the injected carriers forming the channel. Therefore the threshold voltage for this device will remain at zero (channel formation) in the absence of a trapped charge that can remain trapped longer than 30min.

4.5 Low drain voltage FET experiment

The films in the pentacene capacitor device and the FETs presented are nominally identical. The capacitor device's ability to reach 1GPa and evidence that the sub-threshold current may be important motivates further FET experiments with a lowered sub-threshold current. A sampling of I_d-V_{gs} curves during a pressure cycle for a FET operated at V_{ds} = -1V (to lower the sub-threshold current) is shown in figure 4.12. There is still a significant (relative) sub-threshold current but the pressure response is improved. A plot of the mobility (left side scale) and threshold voltage (right side) are shown in figure 4.13.

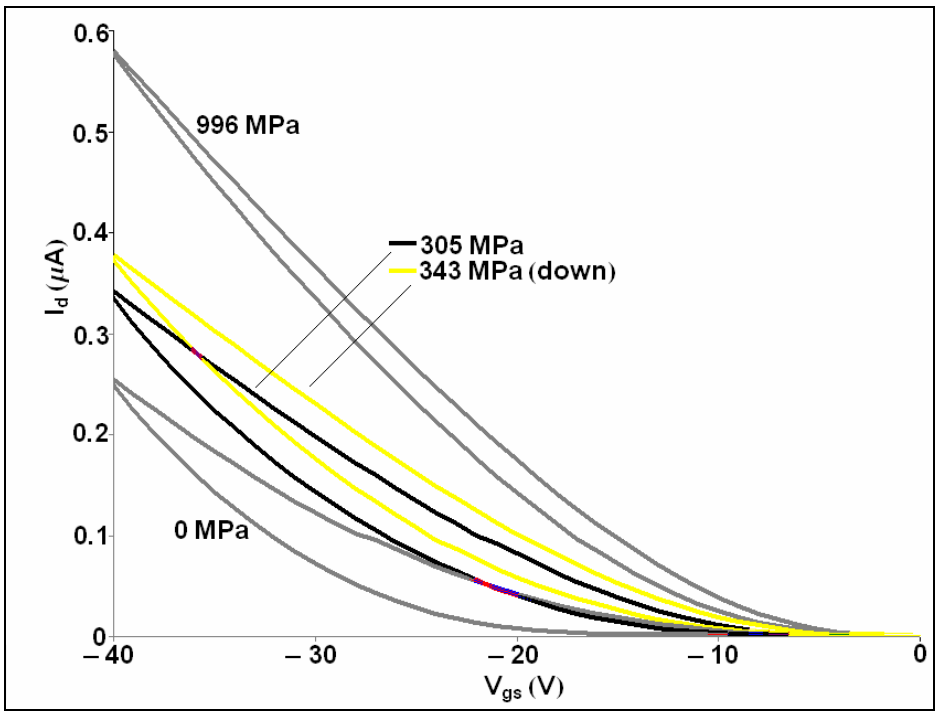

Figure 4.12: I_d-V_{gs} of the FET with reduced V_{ds} at multiple pressure points. V_{ds} = -1V.

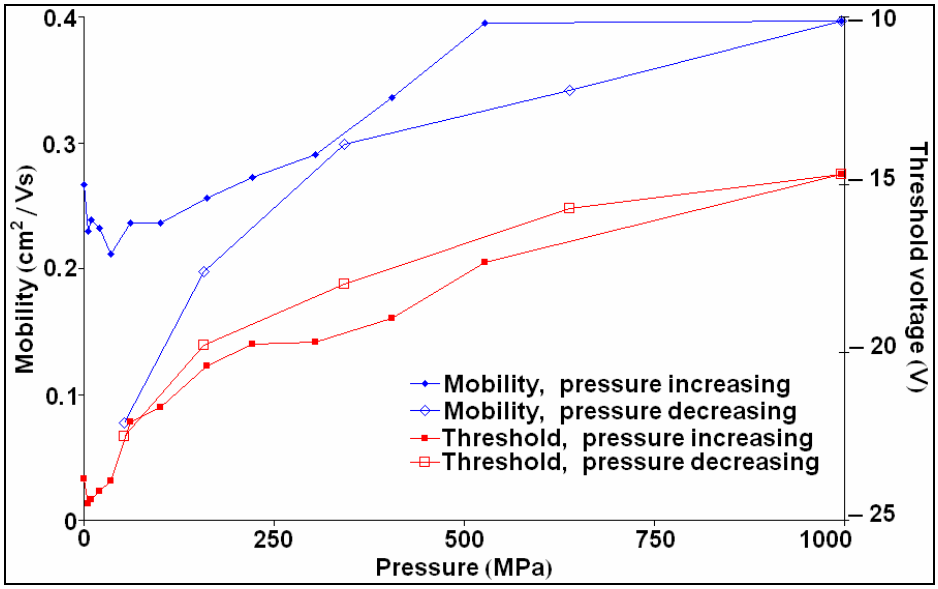

Figure 4.13: Mobility and threshold voltage versus pressure. V_{ds} = -1V. V_{gs} = -40V.

While this trend is more like the response found by Dr. Rang it still has some differences; notably the tendency of the mobility to saturate near 500MPa (which is

roughly where Dr. Rang's pressure run ended) and a much larger threshold swing. There are some interesting comparisons between this data and the data from the pentacene capacitor structure. In the sub 100MPa range the mobility for the FET appears to change little (especially if the one point that dips at about 50MPa were removed) as is the case in the capacitor device. The threshold in this range shifts by 5 to 7V, i.e. a large fraction of the total shift over the full pressure range (10V). The capacitor also indicates that most of the change in trapped carriers occurs over the first 100MPa, even though this change only amounts to a 1V shift, as seen in figure 4.9. Beyond 100MPa the mobility in the FET can be approximated by a linear relationship with a 100% increase in mobility for 1GPa (as in Dr. Rang's paper), which is a lower increase than the capacitor device demonstrates, but matches the linear trend. The FET threshold voltage beyond 100MPa shifts less (another 3V over the final 900MPa). The capacitor device shows a near constant trapped charge density beyond 100MPa.

Chapter 5: Carbon nanotubes

5.1 Introduction

Carbon nanotubes (CNTs) have generated a lot of interest due to their unique mechanical and electrical properties. Current commercial applications for CNTs center on their mechanical hardness and resiliency for use in composite materials.[76,77,78] Studies to exploit the electrical properties continue but are more difficult due to the strong dependence on the type of CNT.[79,80] Applications for CNT based sensors have been proposed based on a changing electrical response with deformation of the tube.[79,80] The pressure system here can be used to deform the tubes uniformly and study their response.

Carbon nanotubes are graphene sheets (single layer graphite) that are rolled up to form a tube. They can be either semiconducting or metallic, depending on unique indices for each type of tube, commonly denoted by *m* and *n*. These tubes show incredible hardness in the axial direction with a modeled bulk modulus in the hundreds of GPa range, however the radial direction has a much smaller modulus (by at least an order of magnitude)[81,82]. Pressure studies have primarily focused on CNT bundles (often called crystals and ropes as well).[81,83,84,85,86,87,88,89,90] CNT bundles show increased conductivity with pressure and a transition from a circular to a hexagonal cross section for the individual CNTs. Raman studies of single CNTs under pressure while in suspension reveal changes in the band gap and radial breathing phonon mode.[34,47,48] Both the bundle and suspension samples experiment on an assembly of CNTs. Single tubes are predicted to change shape (to an ellipsis, racetrack, and dumbbell shape cross section) and to have increased electrical conductivity under pressure.[91,92,93] Most of the transition pressures

(where change in the cross section starts) listed in these studies are above 1GPa, however a few values lower than the 1GPa limit of the GC10 cell are also found.[15,47,48,85,91] Even if a shape change occurs under 1GPa, there is no evidence that the nanotubes will exceed their elastic limit.[15,47,93] This project will focus on the electrical response of single, semiconducting, CNTs at pressures less than 1GPa.

5.2 Device setup

The samples tested in this project are bottom gated field effect transistors (FET). The CNTs are deposited on a silicon wafer with thermal oxide by Dr. Jia Chen at IBM Yorktown Heights. The Si wafer is doped to allow conduction and act as the gate, the contact to the gate is through a layer of metal on the back side of the wafer. Titanium/gold source/drain contacts are deposited on the CNTs by Dr. Chen. There is no registration of the CNTs to the contacts or detailed classification of the CNTs present, so the orientation and *m* and *n* indices of the nanotubes are unknown.

While the chirality of the tubes is unknown, some characterization is done. In figure 5.1 an AFM image shows a deposition of CNTs used. The tubes are all moderately long and have diameters of about 10nm. The image for this deposition, from the first batch of devices sent by Dr. Chen, indicates that the layer is more of a mat than individual tubes scattered on the surface. A more sparse layer is used for creating the CNT based FETs. The lengths of the tubes, shown in figure 5.1, demonstrate the need for source and drain contacts to be made with small channel lengths, so that the devices can access a single nanotube and not a chain. A metal pattern with channel lengths of 1 or 0.5μm and a width of 10μm is used. These source and drain metallizations are connected

to pads of 100 by 100µm and form a total metal pattern that took up less than 1mm^2. The pattern is repeated every 1mm, see figure 5.2. This final chip design is able to yield nearly 50% of the devices in working order.

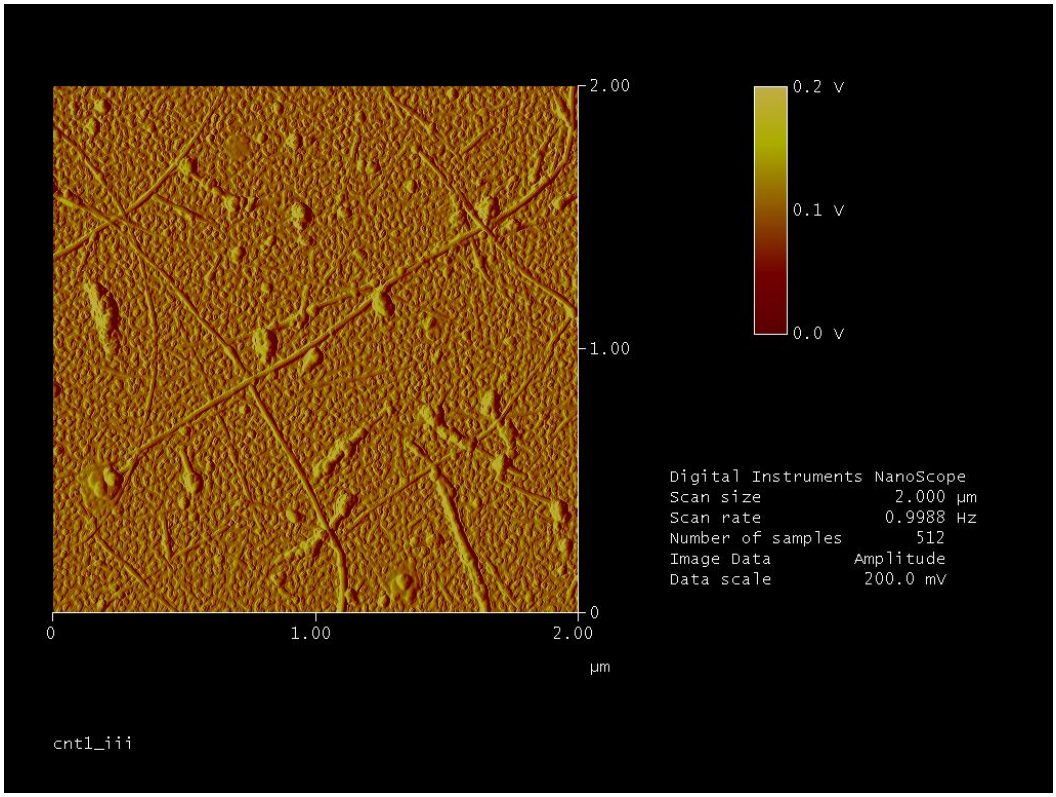

Figure 5.1: An AFM image of the first CNT device layer sent. The tubes are generally larger than 1µm in length and smaller than 20nm in diameter.

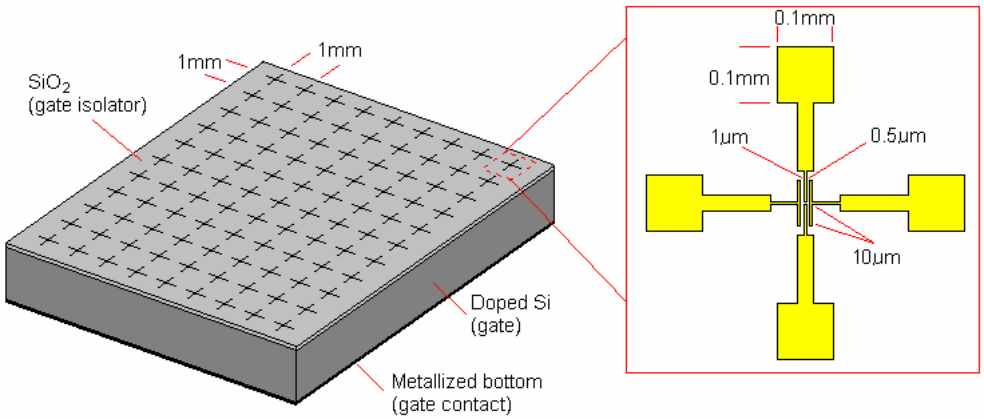

Figure 5.2: Final device layout and dimensions; gate oxide thickness is 300nm.

The typical preparation for the sample is to test all of the devices, cut the chip into 1 x 2mm die, and then retest the devices. The CNT devices are able to withstand cutting on a wafer saw while being exposed to cooling water (10 out of 11 survive on a test run). However one of the ways a device can fail is from incomplete lift off of the contact metal. A UV tape (from Furukawa Electric Company) allows a similar amount of devices to survive the sawing process (14 out of 16) and has the potential to remove some metal that shorts the devices due to incomplete lift off, allowing them to be used. After the die are cut, the retest is used to select devices for use in the pressure system. Target devices are semiconducting CNT FETs with low gate currents.

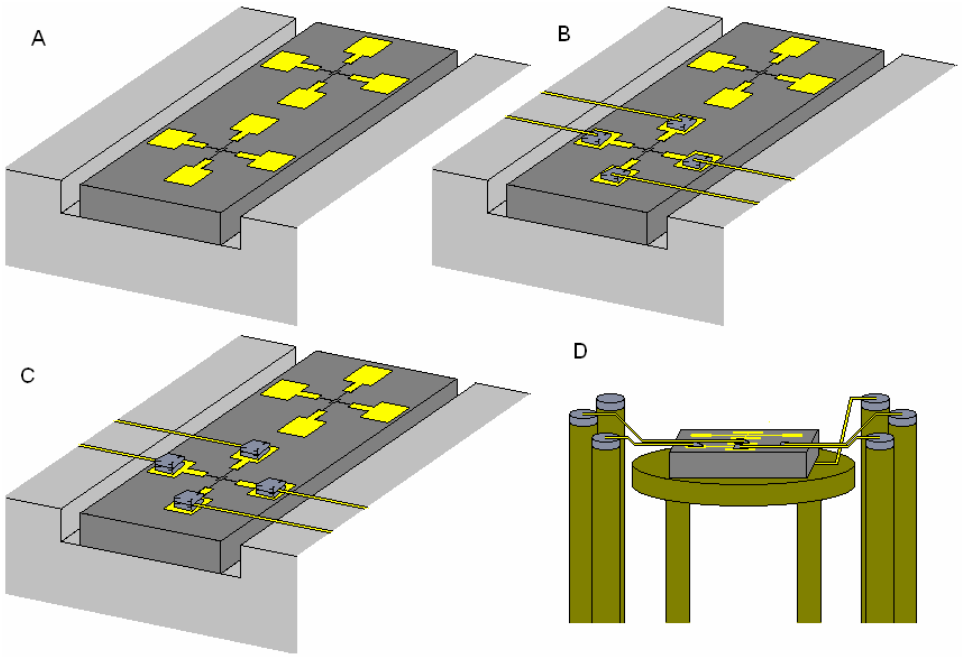

Figure 5.3: Device mounting process. A; Chip in Al block. B; In and gold wires set and ready for heating. C; After heating more In is added to ensure the wires are enveloped. D; The free ends of the wires are soldered to the In tipped plug feed-throughs.

A specialized method needs to be used to contact the devices to the feed-throughs on the GC10 plug. Indium is used to solder the wires to the gold pads on the die and to

connect the wires to the posts on the GC10 plug. A rough schematic of the process is shown and described in figure 5.3.

5.3 Effects of pressure on I-V characteristics

The primary I-V response measured is an I_d-V_{gs} curve. The typical curve is swept with V_{gs} = +10V to -10V and V_{ds} = -0.5V. I_d-V_{ds} curves are also monitored with V_{ds} swept from +0.5V to -0.5V and V_{gs} = +10V, 0V, and -10V. The geometry of the CNT device complicates clear characterization; while the metallization sets up a channel of 10μm by 1 or 0.5μm, the actual width of the channel is the CNT diameter and the actual length could be longer if the CNT is not perfectly aligned at a 90 degree angle to the source/drain contact edge. The uncertainty in the channel length and width can be partially alleviated by normalizing the extracted mobility. The form factor element will be constant for a given device and cancel out in a comparison of mobilities at different pressures. Another problem with an unaligned CNT is that the source/drain voltage across the CNT is only partially in the direction of conduction, creating different fields in different devices with the same V_{ds}. The only way to remove this effect is to image the device and find the alignment of the CNT. Only one device is presented here which represents the only sample to be successfully loaded and stressed in the pressure system. With additional samples, imaging to find alignments and compare the devices could be done and represents an avenue for future experimentation.

Initially, helium was used as the initial pressure transmitting gas. Two samples were monitored and found to have little systematic change under He pressure. However, it is possible the small He atom passed through the tube wall without imparting a

deforming force to the CNT. A calculation of the space inside the carbon hexagon, based on C-C bond lengths, confirmed that He can penetrate the nanotube walls. The experiment was re-run with Ar as the pressure medium. Analysis of Ar indicated that deformation should occur, see figure 5.4. Ar may still enter the nanotube if the ends were open or defects were in the tube where Ar could pass through, although since a measurable response was found it is assumed these effects are minor.

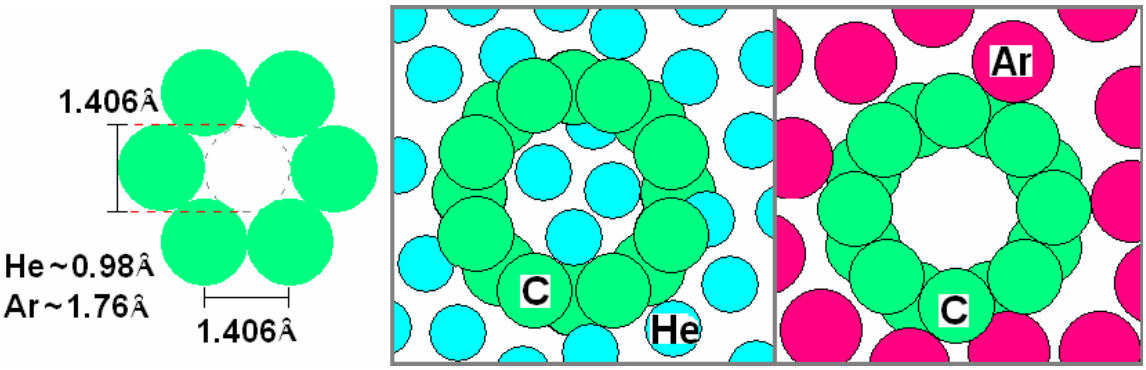

Figure 5.4: Simple analysis of gas penetration into the CNT.

Only one device remained for testing in the Ar environment. The I_d-V_{gs} for this device is shown in figure 5.5. Isolating the higher bias region as the main semiconductor response, a linear trend is extracted to calculate the mobility. A plot of mobility change with pressure is shown in figure 5.6. A change of near 50% over 1GPa is found for this device. This is lower than the increases found for the P3HT and pentacene, but the bulk modulus of the CNT is generally higher than in the other materials. The retrace shows a large separation in the pressure increase and decrease curves at 600MPa, but the final mobility matches the initial mobility indicating that the device is not permanently altered during pressurization. A threshold voltage plot, corresponding to the linear extrapolation on which the mobility is based, versus pressure reveals no consistent change, see

figure 5.7. Ar is able to impart pressure to the CNT and the pressure increases the mobility of the device up to 50%.

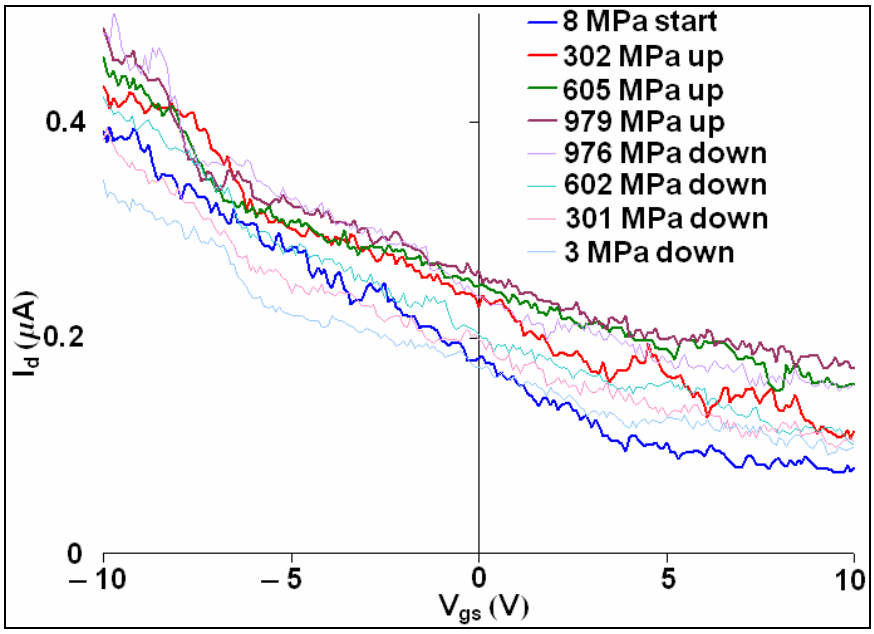

Figure 5.5: The device I_d-V_{gs} curves under Ar pressure. V_{ds} = -0.5V.

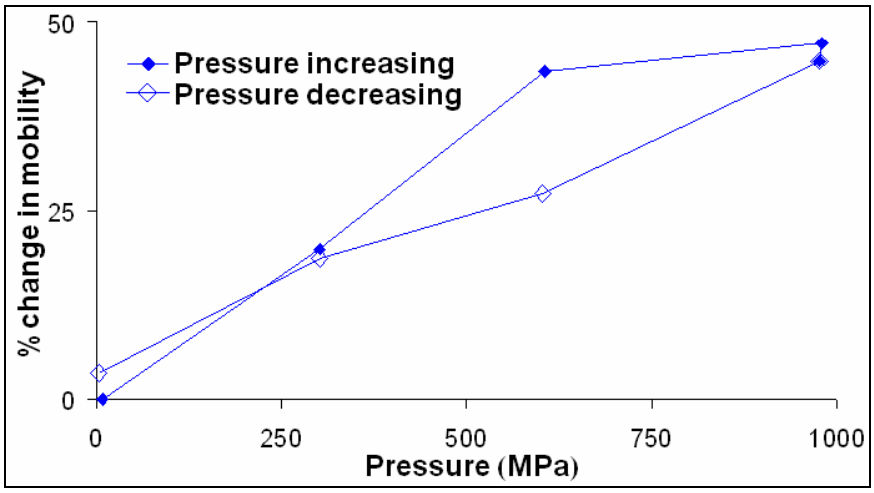

Figure 5.6: Change in mobility vs. pressure, the analysis comes from a linear fit to the high bias region in figure 5.5. V_{ds} = -0.5V. For a 5nm diameter CNT on the 1μm channel (oriented at 90° to the contacts), the initial mobility is approximately 200cm^2/Vs.

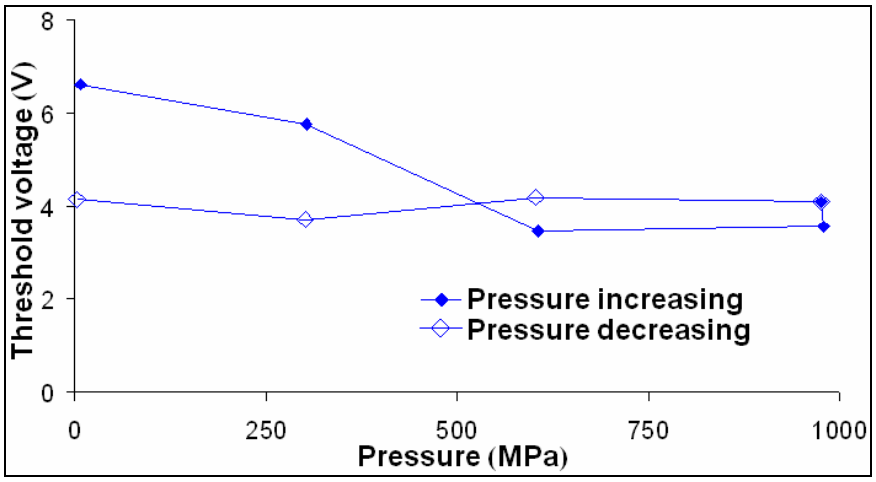

Figure 5.7: Threshold changes as calculated by the linear fits to the currents in figure 5.5 used in the mobility calculations for figure 5.6.

5.4 Temperature dependence

The noise that is present in figure 5.5 is expected to be temperature dependant; hence a variable temperature experiment is performed. A device sealed in the pressure system is placed in a liquid nitrogen (LN2) bath (the entire pressure cell is submersed) and the I_d-V_{ds} measured. The electrical response is found to vanish in the bath and does not fully recover upon removing the device from the low temperature environment. An incomplete recovery is found immediately after removal from the LN2 but the device subsequently degrades with time. Figure 5.8 shows the curves measured for the device at room temperature before the bath, at 12C after the chilling, and room temperature the next day. The curves are the I_d-V_{ds} with V_{gs} = -10V. The detrimental effects of cooling the sample ruled out using LN2 to minimize the noise present.

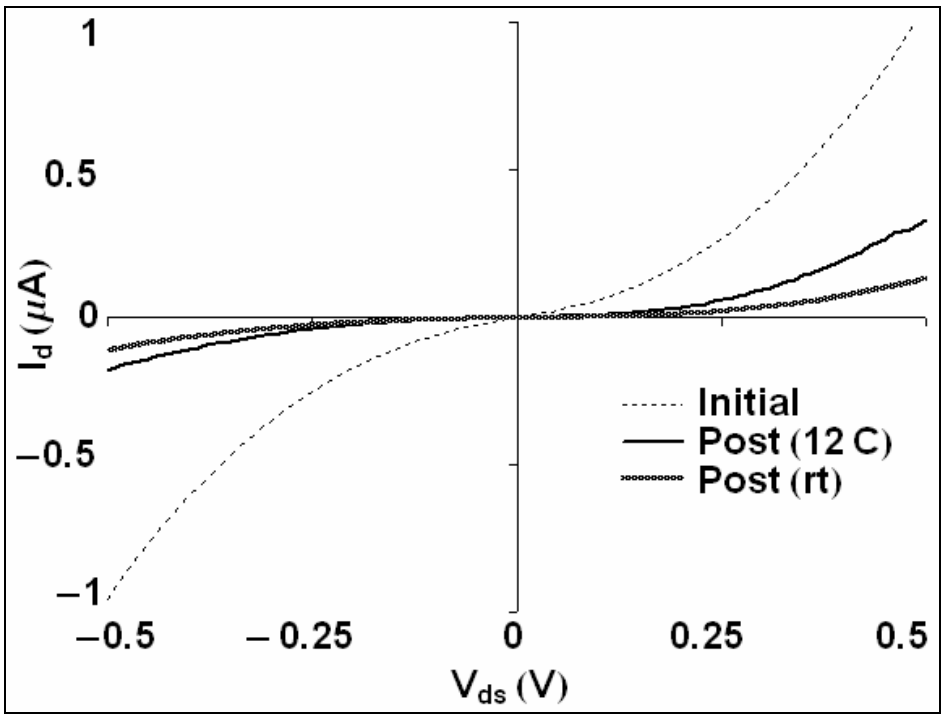

Figure 5.8: I_d-V_{gs} curves in a temperature test. The atmosphere is Ar and it is placed under 19MPa (source bottle pressure) to ensure that the chilling and condensing of the gas under LN2 does not result in a partial vacuum in the pressure system. V_{gs} = -10V.

5.5 Summary/Conclusion

Ultimately it was found that CNT based devices do exhibit a pressure response if a proper pressure transducing medium can be found. A change of 50% in mobility over 1GPa is found, which with a bulk modulus of about 10GPa for the tube walls seems reasonable.[91,93] It is unfortunate that follow up experiments to verify the pressure response could not be done. To further the research, characterization of the CNT being tested to connect the response to a CNT type/family (specific *m* and *n* number) is possible. Also, a systematic study of the temperature dependence is warranted.

Chapter 6: Single molecular crystals

6.1 Introduction

While thin films can achieve a certain degree of molecular order, domains and grain boundaries are present in addition to stacking imperfections and impurities.[1,7,20,29,30,72,94] These imperfections are blamed for the uncertainty in the pentacene FET data presented in section 4.3. To eliminate the effects of grain boundaries and further reduce impurity and disorder effects, FETs made with single crystals of organic semiconductor material are tested. Previous research on single crystal FETs have revealed many improved characteristics.[31,35,36,53,65,95,96,97]

Rubrene is chosen as a starting material due to the previously published results by Rang et al. In his work, the device is a rubrene crystal with source and drain contacts, the gate insulator, and gate contact fabricated directly on the crystal surface, figure 6.1. This device can return a 100% change in mobility over 1GPa. To vary this experiment the device structure is changed to a crystal laminated to the source, drain, insulator, and gate structure after they are fabricated, figure 6.2.

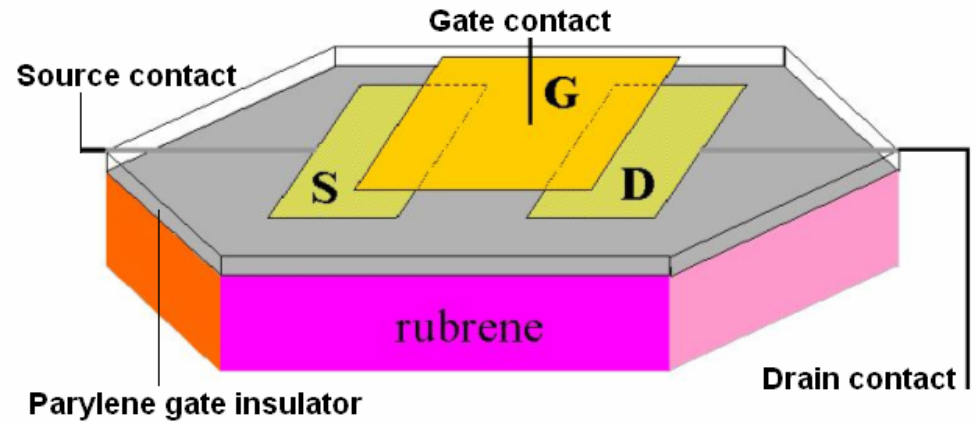

Figure 6.1: Device setup of FET on rubrene crystal.

6.2 Crystal and device fabrication

The device substrates with the source, drain, insulator, and gate are fabricated by Mr. Yu Xia of Prof Frisbie's group. Two substrates are fabricated for testing, one using a hard silicon substrate and another using a soft PDMS substrate. The silicon substrate, figure 6.2 a, follows the device structure used by Dr. Newman for tetracene single crystal devices. The Si wafer is doped and acts as the gate. There is 300nm of thermally grown SiO2 on the top surface to provide a gate insulator. The source and drain contacts are made by etching wells into the SiO_2, filling the wells with gold, and planarizing the surface (to make the contacts flush with the SiO_2 layer). The PDMS substrate, figure 6.2 b, follows a procedure used by Dr. Menard et al. in their study of single crystals.[97] This substrate is formed by creating a mold into which liquid PDMS is poured and then hardened. The mold forms a stamp that has raised source and drain contacts, an open air gap to provide the gate insulation, and a lower level for the gate. The contact metal is evaporated on the stamp, with the steep sides to the raised source/drain providing isolation between the contacts and the gate. In both cases the crystals are set in place as the last step in device fabrication, sometimes using slight pressure or biasing the device to promote crystal adhesion, but often the crystal will adhere on its own.

The crystals are grown by Mr. Xia as well. A thermal gradient sublimation is used to both purify the source material and grow the crystals. The sublimation system is composed of glass tubes wrapped with heating elements. A carrier gas (Ar) is supplied to move the sublimated material through the gradient, this gas then exits the system through a silicone oil bubbler to prevent moisture backflow. The temperature gradient is set before the source material is raised to its sublimation point. A purification run will

typically create some crystals; these crystals are pulverized and used as a source for the final crystal growth.

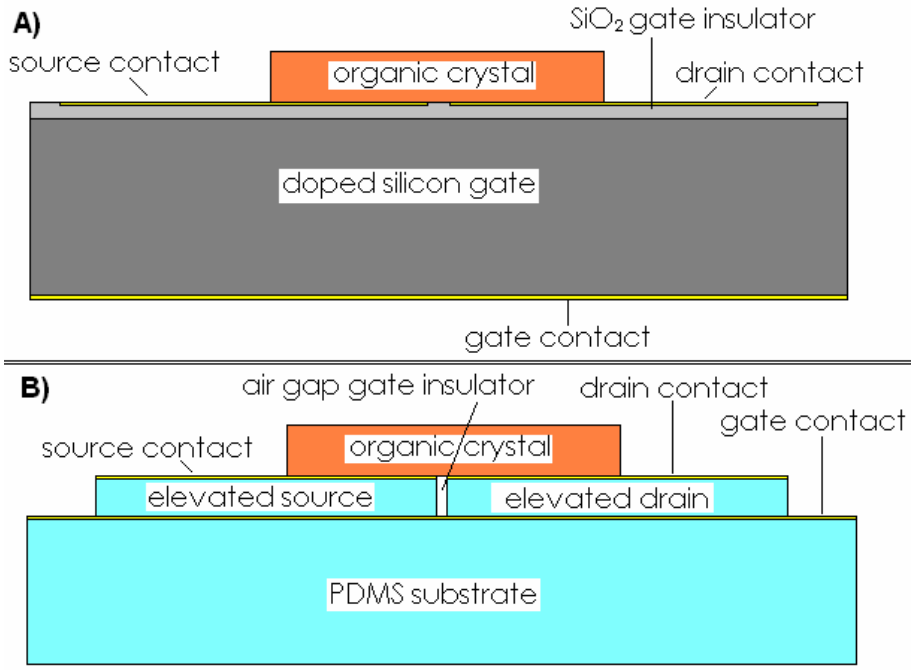

Figure 6.2: A. Diagram of an organic crystal on a silicon wafer device.
B. Crystal on PDMS stamp.

An examination of the effects of pressure on the single crystals is preformed before I-V tests. Optical and AFM measurements are used to characterize the crystals before and after a pressure cycle on the free standing crystal. Little to no change is discovered in these tests. X-ray characterization for these crystals is not deemed feasible due to the small size of the crystals, a size of nearly 10mm by 5mm is desired but even a good large crystal is likely to be only in the couple mm^2 range.

6.3 Pressure effects on I-V characteristics

Using a silicon wafer for an organic crystal substrate has the advantages of good adhesion to the crystal and of being durable, both for wiring the device and in the

pressure system. The problem is that the adhesion is too strong and the compression mismatch is too large for the device to undergo large changes in strain. The organic materials are assumed to have a bulk modulus of near 5GPa but crystalline silicon has a modulus of around 100GPa. The strong adhesion between the crystal and substrate and the compression mismatch are exemplified in the image shown in figure 6.3. This device is made with a relatively thick rubrene crystal (~300μm) attached to a silicon substrate. The crystal appears to have sheared off an interfacial layer of the organic crystal from the bulk, most likely because the crystal is trying to compress more than the silicon would allow. The device is pressurized to 150MPa and during the 70MPa to 150MPa step the current in the device decreases dramatically, indicating that this is when the damage to the crystal occurs, figure 6.4. However the current recovers, but now the threshold for detrimental pressure effects in subsequent experiments is reduce to 50MPa.

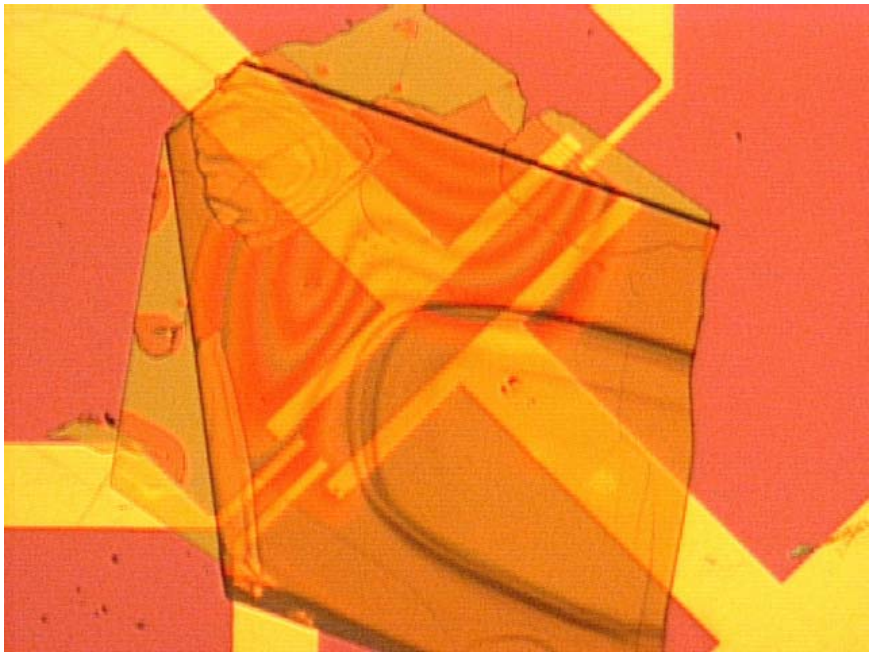

Figure 6.3: Image of the bulk crystal sheared off the interfacial organic layer connected to the Si wafer.

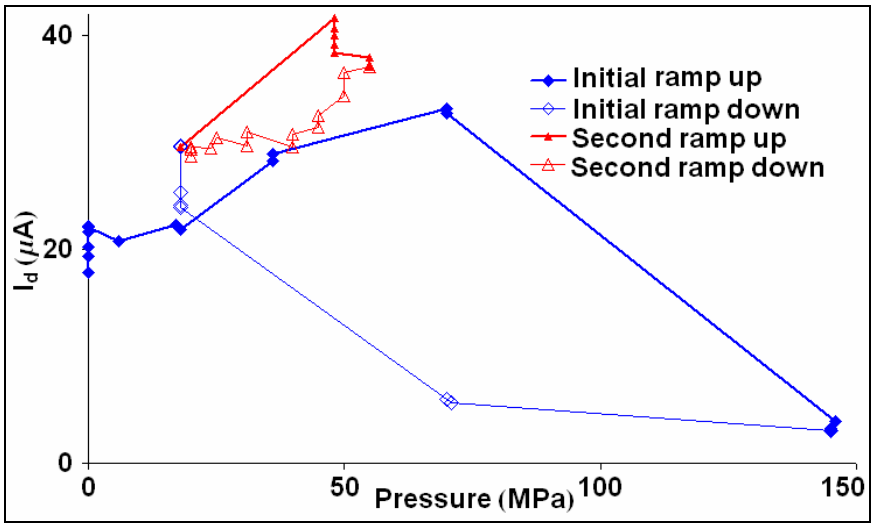

Figure 6.4: Current versus pressure plot for the device shown in figure 6.3. V_{gs} = -40V. V_{ds} = -7.5V

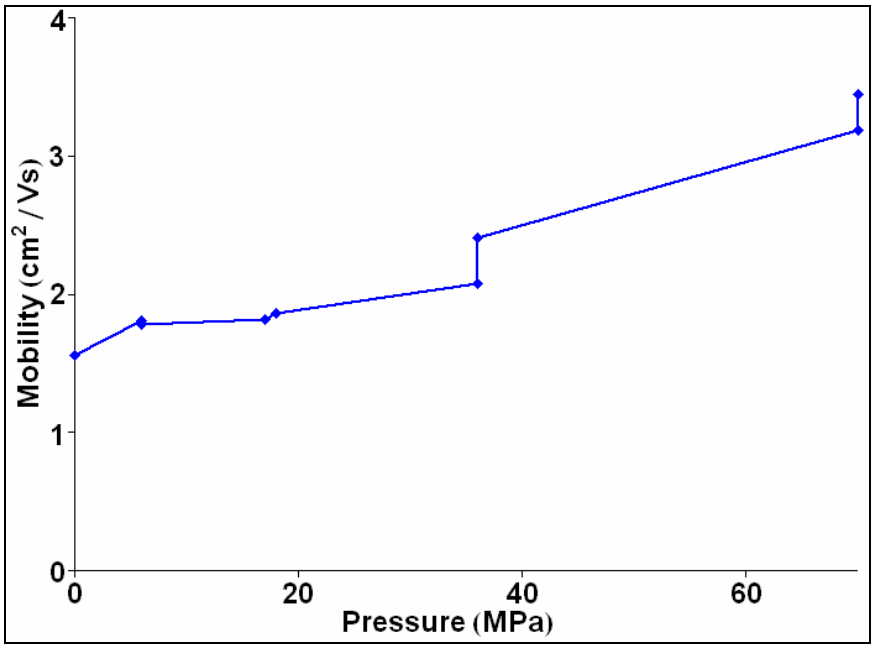

Figure 6.5: Mobilities versus pressure for the device shown in figure 6.3. V_{ds} = -7.5V

The I-V response is monitored through an I_d-V_{gs} curve. Extracting the mobilities for the initial increase to 70MPa (before damaging the crystal) gives the plot shown in figure 6.5. Within this small region there is already an increase in excess of 100%, which if extrapolated to 1GPa would be an increase of 1400%. If this crystal could be

monitored for the full 1GPa of pressure, the superlinear form from equation 1.8 might be measurable.

The threshold voltage for the initial increase is nearly constant at -12V until the 70MPa pressure is reached, where it shifts to -17V. The threshold voltage change for the full pressure range is shown in figure 6.6. With the change starting at 70MPa it is possible that this is when the damage to the crystal starts. This assumes that the threshold is shifting due to increasing trapped charge from an increased trap site concentration by damage the crystal incurs. Once the device "recovers" at 20MPa the threshold remains variable, indicating that these trap sites are still active and the device still shows the effects of crystal damage.

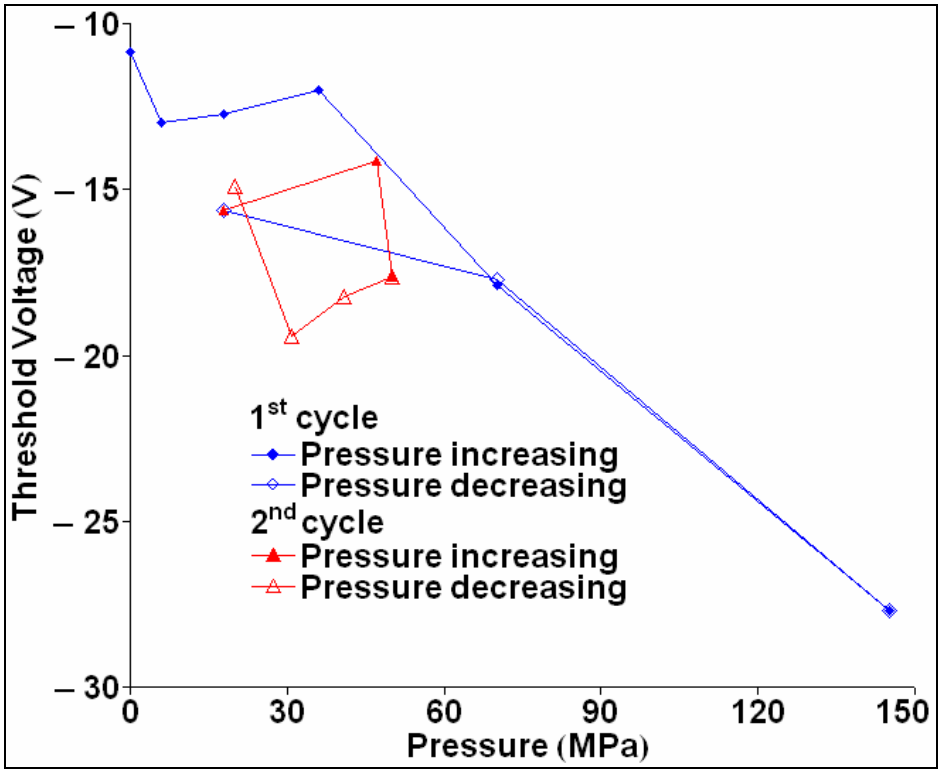

Figure 6.6: Threshold voltage shift for the device shown in figure 6.3. V_{ds} = -7.5V

A thinner crystal (~100μm) is applied to a silicon substrate to try and avoid the compression mismatch effects that caused the shearing depicted in figure 6.3. While visible damage is not detected with this device, the I-V response is very slow and high pressures are still not accessible. Initial current levels remain constant from atmosphere to 16MPa. Leaving the device dwell at 16MPa for 60hrs results in an increase in current from 19 to 23μA, or a 21% increase. Increasing the pressure beyond this point shows no change at 20MPa and then the current degrades. If only the initial and 16MPa data points (after the 60hrs) are considered, the mobility increases from 0.44 to 0.57cm^2/Vs (28%). The threshold voltage between these two points change from -15V to -16V. Extrapolating this to 1GPa on a linear scale yields a 1700% increase in mobility with a -62V shift in threshold voltage. Ultimately this device does not give enough data to allow for anything more than conjecture.

The upper limit of 70MPa using a silicon substrate emphasizes the need for a soft substrate, like PDMS. Unfortunately, the PDMS substrate suffers from a compression mismatch of its own, compressing more readily than the organic crystal, severing the bond that keeps the crystal attached to the source/drain contacts. Alterations to try and stiffen the PDMS failed to produce a sufficiently smooth surface that would bond to the crystal. A change in equipment that takes a small piece of Be/Cu foil and bends it to make a spring clip type of holder is also possible, figure 2.8. This equipment has not yet been tested thoroughly and the project remains in progress.

6.4 Summary/Conclusions

The plot in figure 6.4 shows that there may be a much greater mobility response to pressure for crystalline rubrene than currently reported. The reason for the increase in pressure sensitivity is attributed to the lack of processing on the crystal, which can damage the conduction layers in the organic crystal. The prospect of getting a compression matched contact setup that can laminate to the single crystal may allow a much larger increase in mobility and probe the exponentially dominant response of equation 1.8. An adaptation of the substrate to the crystal, or the equipment to hold the crystal, is needed to enhance this study.

Chapter 7: Summary and future work

7.1 Summary

It is clear that the application of hydrostatic pressure affects the transport of organic solids. Even in the case of carbon nanotube transistors, a single molecule, a distinguishable response to pressure is evident. The concept of increased mobility through decreased inter-molecular distance is supported by a larger mobility increase in thin films and crystals compared to CNT devices. In addition, a strong pressure response in the fixed charge concentration is observed in certain device structures (as observed with the threshold voltage) and explained by a shift of relative energy levels of the trap sites with the zero-bias Fermi level (or in the single crystal case, a change in trap site concentration).

7.1.1 Mobility

All FET devices show at least an initial increase in mobility with pressure. The P3HT FETs, carbon nanotube FETs, and pentacene capacitor all withstand the full 1GPa of pressure achievable with the current system. Even pentacene thin film FETs, if biased correctly, can withstand the pressure cycle and show an increase in mobility. Within the devices that fail under pressure, the single crystals and pentacene FETs at high V_{ds} bias, there is still a strong increase in mobility at low pressures (1atm to 100MPa).

Among all samples, the single crystal FETs show the greatest promise for mobility modulation with pressure. A possible increase in the 1000% range could be realized if the samples remained functional up to 1GPa. The pressure limit in these devices is

determined by the compression mismatch between the crystal and the substrate, requiring a change in substrate or equipment. The reason for this large potential is seen as two-fold; better order and increased compression. The crystal order and purity of the crystal increases the molecular overlap, and therefore the response of the transport coefficients to pressure. The lack of a hard surface to restrict the compression (as the silicon wafer may for the thin film devices used in this study) increases the actual lattice space reduction. The hard surface is still present in the devices tested in section 6.3 but the damage seen in the device due to pressure indicates that the crystal compression is governed by its own bulk modulus.

The P3HT samples show the next highest increase in mobility with pressure for a FET. A 300% increase over 1GPa for sample 1 is found in section 3.4. The mobility follows a linear trend which is explained by a small (3% or less) change in the lattice spacing. The reason this response is higher than that of pentacene thin film FETs is likely due to its packing. While P3HT forms planar chains that stack parallel to each other, figure 3.2, pentacene is known to pack in a herringbone structure.[39,51] So with pressure the planes containing the P3HT chains can simply move together and increase the π orbital overlap, while the pentacene must rearrange the molecular order to maximize the effect of compression.[37,50]

The comparisons to pentacene thin films thus far have been based on FETs, as presented in section 4.4 the capacitor device can also be used to measure a mobility response to pressure. This device shows a change in mobility of around 500% over 1GPa. The trend is approximately linear, same as for the P3HT. The FET samples in section 4.3 show an initial increase in mobility up to 100MPa and then either level off or

start to degrade. The largest mobility increase in these samples is about 100% for sample C and the lowest is about 30% for sample E (although that may be do to the lower starting mobility for sample C compared to sample E). If this 100% increase for 100MPa is extrapolated to 1GPa, the pentacene thin films approach the increase in mobility measured for rubrene single crystals. For the FET sample tested in section 4.5, the mobility increases about 100% up to 500MPa and then levels off up to 1GPa.

The carbon nanotube device shows the lowest increase in mobility, but also is unique because its semiconducting layer consists of a single molecule. An increase of 50% over 1GPa in the mobility is observed, figure 5.6. While other materials have a change in mobility largely attributed to their change in inter-molecular distance, the CNT devices change their inter-atomic spacing. Given that the carbon-carbon bonding is much stronger than the Van der Waals bonding in the molecular and polymer systems, it is not surprising that the change in mobility measured here is the smallest.

7.1.2 Threshold voltage shifts

A clear threshold voltage shift is visible in the P3HT and pentacene FETs, while the pentacene capacitor device does not show much (if any) threshold shift. The single crystal device has a nearly constant threshold voltage in the low pressure region and then starts to change under higher pressures, which is attributed to damage in the device. The CNT device does not show any consistent threshold voltage change.

The threshold voltage in a FET structure is directly related to a change in fixed (trapped) charge within the channel. This change is explained by a shift in relative energy levels with pressure (section 3.4 or appendix A). In the single crystal device from

figure 6.3, the damage to the crystal could create additional traps along cracks and the surface of the sheared layer. This picture could explain why the shift only occurs after 70MPa of pressure is reached. The pentacene-oxide-metal capacitor device in section 4.4 shows very little trapped charge change that can last to the next measurement. There is evidence of shallower (faster releasing) traps that alter the voltage where channel annihilation occurs (a shift to -20V), section 4.4. Also, there is some measured trapped charge that persists through one measurement but releases charge carriers in the (at least) 30min interval between measurements (small shift in channel annihilation onset from figure 4.6). It is possible that the presence of the second contact in FETs and the application of the V_{ds} bias is filling these shallower traps before they would be filled in the capacitor device, making them affect the threshold voltage in a different way.

7.2 Future work

The basic pressure response of P3HT is characterized by using the device setup covered in section 3.2. A variation in film deposition for device construction could lead to changes in pressure response. Using P3HT in the structure described in section 4.4 could offer a new measurement of the mobility response already found. An expansion of the temperature trials in section 3.5 is needed to properly measure the change in the zero-bias Fermi level and trap energy separation. The ion gels need to be characterized under pressure. If this characterization is possible, merging the ion gels with the capacitor structure could provide further insights into channel creation.

The pentacene capacitor device could also be tested with ion gels. A study of pentacene film characteristics versus pressure will be needed to determine why the mobility responses look similar to figure 4.2.

The future work for the single crystal and CNT based devices require useful FETs. For the CNTs this means obtaining devices again to prove the results already found. There is also some work on graphene resistance measurements under pressure that can be considered. For the single crystal FETs a device/equipment combination that allows for testing in the full pressure range is required.

Appendix A: The relationship between trapped charges and threshold voltages shifts.

In the following discussion a p-channel FET is assumed.

In equation 1.14 a change in the threshold voltage is related to a change in fixed charge by:

$$\Delta V_T = -\frac{\Delta Q_{fixed}}{C}$$

The ΔQ_{fixed} is attributed to traps. The traps may be donor-like (neutral when occupied by an electron) or accepter like (neutral when occupied by a hole). As can be shown, the distinction does not matter when dealing with the change in fixed charge.

$$\begin{aligned} Q_{fixed} &= eN_T^* \quad donor\ like \\ Q_{fixed} &= -e(N_T - N_T^*) \quad acceptor\ like \\ \Delta Q_{fixed} &= e\Delta N_T^* \end{aligned} \qquad \text{Equation A.1}$$

N_T^* is the trap concentration occupied by a charge carrier. N_T is the total sheet concentration of traps. The general form for N_T^* is:

$$N_T^* = \frac{N_T}{1 + \exp\left(\frac{\Psi_F - \Psi_T^*}{kT}\right)} \qquad \text{Equation A.2}$$

Ψ_F is the Fermi energy. kT is the thermal energy. Ψ_T^* is the effective trap energy, the trap energy plus any degeneracy factors that may be associated with the impurity.

A.1 Changing the trap site concentration

N_T is assumed constant for most of the devices considered in this thesis. Only when the semiconductor layer undergoes damage, like in the single crystal case in chapter 6, is trap site creation considered. This may not always be the case. A change in trap energy with changing pressure could move an impurity site energy from outside the band gap inside, effectively adding trap sites without introducing new impurities. This is also possible in reverse (a trap concentration leaving the band gap).

A.2 Fast traps

If the traps are allowed to fill fast (during the time the measurement is taken) the Fermi energy can be expressed through the HOMO level and the free carrier concentration, p_{free}:

$$p_{free} = N_0 \exp(\frac{\Psi_H - \Psi_F}{kT})$$

$$\Psi_F = \Psi_H - kT \ln\left(\frac{p_{free}}{N_0}\right)$$

$$N_T^* = \frac{N_T}{1 + \exp\left(\frac{\Psi_H}{kT} - \ln\left(\frac{p_{free}}{N_0}\right) - \frac{\Psi_T^*}{kT}\right)} \qquad \text{Equation A.3}$$

$$N_T^* = \frac{N_T}{1 + \frac{N_0}{p_{free}} \exp\left(\frac{\Psi_H - \Psi_T^*}{kT}\right)}$$

p_{free} is the free carrier concentration based on non-degenerate statistics. N_0 is the effective density of states in the HOMO band, assumed to be the total free carrier sites in the organic material. Ψ_H is the HOMO level energy (valence band edge).

p_{free} can be estimated, using equation 1.13, as:

$$V_g = -\frac{Q}{C} = -\frac{1}{C}(Q_{fixed} + e\,p_{free}) = V_T - \frac{e\,p_{free}}{C}$$

$$V_g - V_T = -\frac{e\,p_{free}}{C} \qquad \text{Equation A.4}$$

$$p_{free} = \frac{C}{e}(V_T - V_g)$$

Equation A.4 results in a p_{free} of the order 10^{12} cm^{-2} (for the maximum V_T-V_{gs} used in this project). An estimation of N_0 based on the pentacene molecular density of $3\text{x}10^{21}$cm^3 and normalizing by the monolayer thickness yields N_0 on the order of 10^{15}cm^{-2}. The fast trap's dependence on p_{free} creates a varying charge with bias, not a fixed charge. Consequently, the fast traps will not contribute to the ΔV_T described in equation 1.14.

A.3 Slow traps

For slow traps (those that do not change their charge state during the measurements) the Fermi level in equation A.2 can be replaced by the zero-bias Fermi level:

$$\Delta E = \Psi_{F0} - \Psi_T^*$$

$$N_T^* = \frac{N_T}{1 + \exp\left(\frac{\Delta E}{kT}\right)} \qquad \text{Equation A.5}$$

Ψ_{F0} is the Fermi level at zero-bias. Assuming that N_T remains constant under applied pressure and that the change in ΔE is small, Q_{fixed} can be written as:

$$\Delta Q_{fixed} \cong e\delta N_T^{*}$$

$$\delta N_T^{*} = -\frac{N_T}{kT}\left(1+\exp\left(\frac{\Delta E}{kT}\right)\right)^{-2}\delta(\Delta E) \qquad \text{Equation A.6}$$

Since $\Delta V_T = -\Delta Q_{fixed}/C$ (equation 1.14), a positive shift in ΔE will result in a positive ΔV_T.

A.4 Conclusion

Within this project a change in threshold voltage with pressure (in the absence of detectible damage to the semiconductor layer) is interpreted as a change in the energy level spacing between the trap and zero-bias Fermi levels.

Appendix B: Pressure effects on the pentacene film.

One interpretation of the pentacene data's inability to retrace is that the thin film is altered by the pressures applied. To check whether this is the case, a study of the films before and after pressure is preformed. An optical check of a film after pressure is show in figure B.1. As can be seen there are defects that appear in the film. While the presence of defects could be seen as confirmation that the films are damaged, the actual area of the channel that is altered is quite small and the changes in the pentacene transistor data is significant. These images are from a CCD mounted to a microscope using a 100x objective.

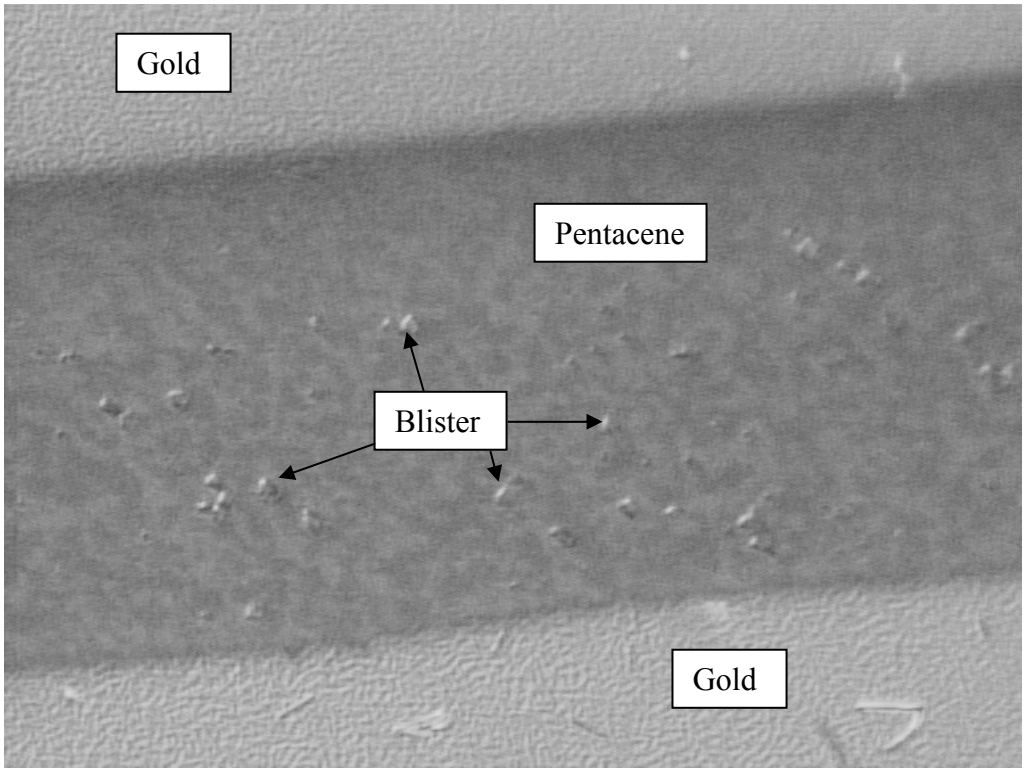

Figure B.1: Image of the blistering occurring in the channel of a pentacene FET. The top and bottom bands are the gold contacts. Damaged occurred during a pressure cycle to 1GPa.

This damage is visible only when the pressure ramp is too fast. Modifications to slow down the pressure increase and decrease cycle described in section 2.2.1 result in no visible damage to the thin film.

Atomic force microscopy (AFM) imaging is used next to clarify the films persistent response to pressure. The AFM images are taken with a Nanoscope III A – Dimension 3100 AFM in tapping mode. Figure B.2 shows a typical result for the AFM imaging. The results are fairly ambiguous. Occasionally the images would show some type of change but often it would appear like figure B.2, no real change.

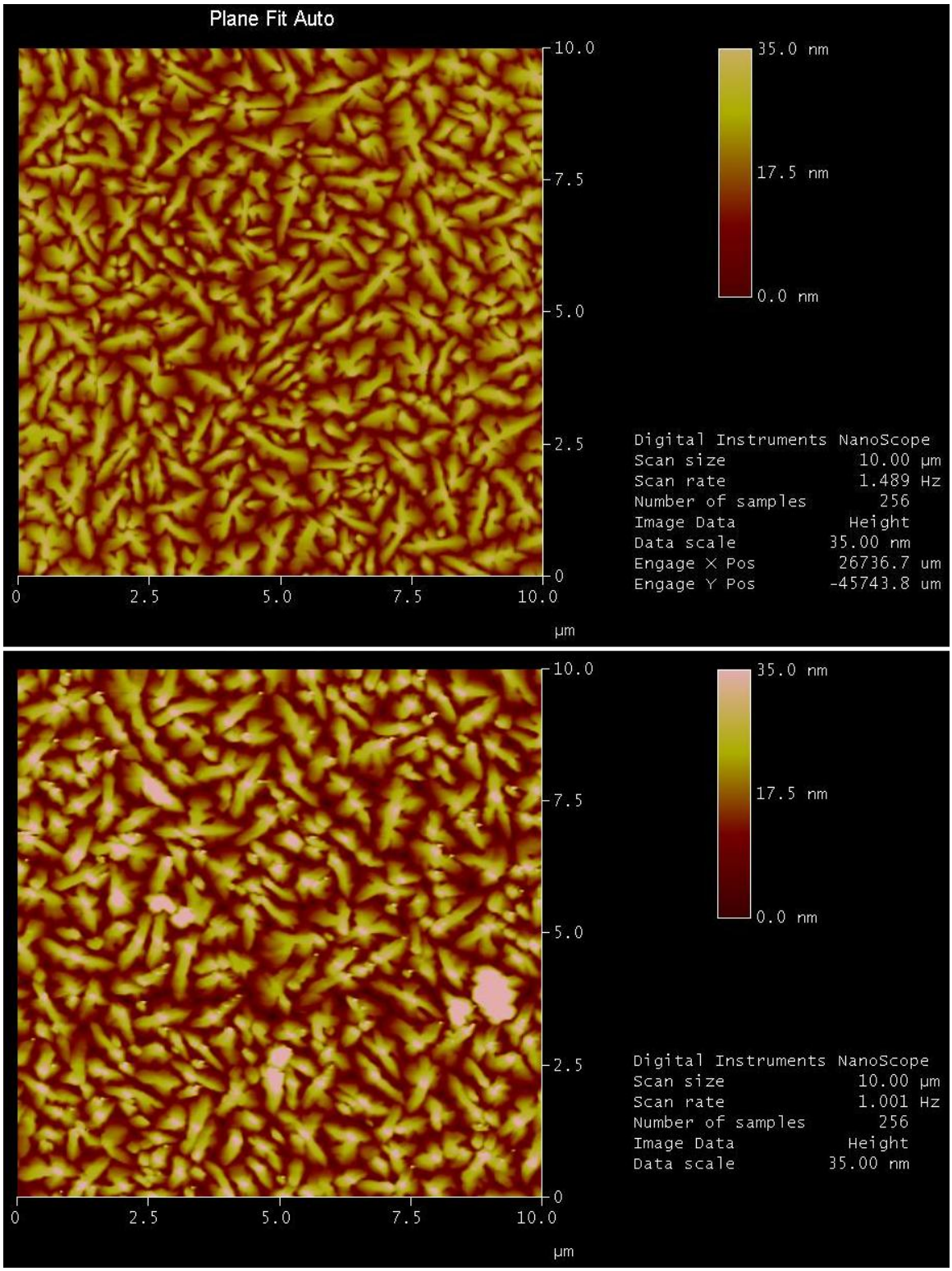

Figure B.2: AFM image before pressure (top) and after (bottom), only minor changes are visible.

X-ray characterization is preformed to determine if any polymorph changes occur. Six bare films (no metallization) for x-ray diffraction are prepared and measured by Dr. Sandra E Fritz-Vos. Then three samples experience pressure while the other three are used as a control group. After the pressure cycle finishes, the samples are again measured by Dr. Vos with little variation found. Upon refinement of the pressure run, a new x-ray test is preformed by Mr. Yu Xia on films fabricated by Mr. Yan Liang; again no changes are noticeable, see figure B.3.

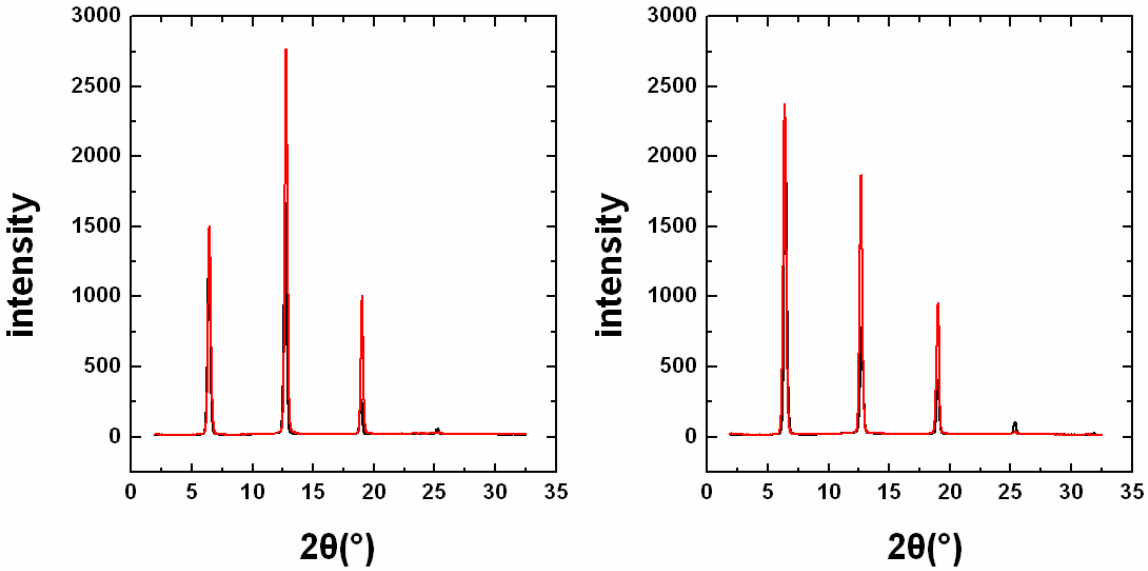

Figure B.3: X-ray diffraction of a pentacene film before and after pressure to 1GPa. The traces for the two films line up so that the reflections are indistinguishable. The two plots are for two separate samples.

The conclusion from this data is that proper pressure application, to the levels used in this project, is not sufficient to change the molecular ordering of the film.

Appendix C: Data summary for all of the pentacene FETs tested in section 4.3

This section is primarily a detailed summary of the data for the pentacene thin film FETs listed in table 4.1 and reprinted here:

Sample Name:	Fabricated by:	Pentacene thickness:	Substrate temperature during fabrication:
A	Dr. Vos	16nm	60C
B	Mr. Liang	30nm	No heating
C	Mr. Liang	15nm	No heating
D	Mr. Liang	15nm	40C
E	Mr. Liang	15nm	60C

Table 4.1: The pentacene samples and their controlled differences.

C.1 Sample A

Sample A is the first pentacene sample to have a positive response to pressure. The I_d-V_{gs} curves for the sample at various pressures are shown in figure C.1.

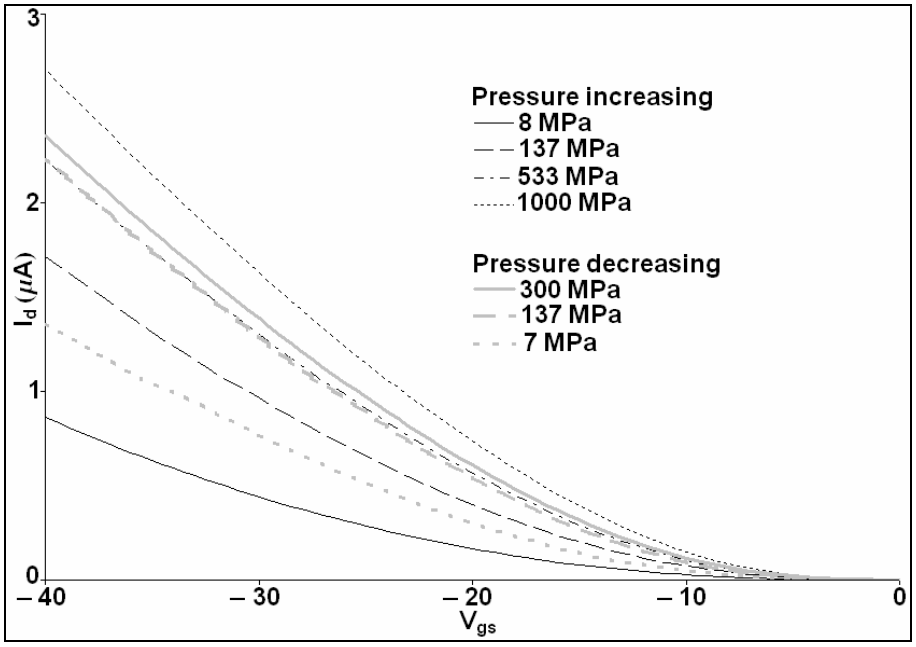

Figure C.1: I_d-V_{gs} for sample A under pressure. V_{ds} = -10V.

Tracking the current with pressure gives the plot shown in figure C.2.

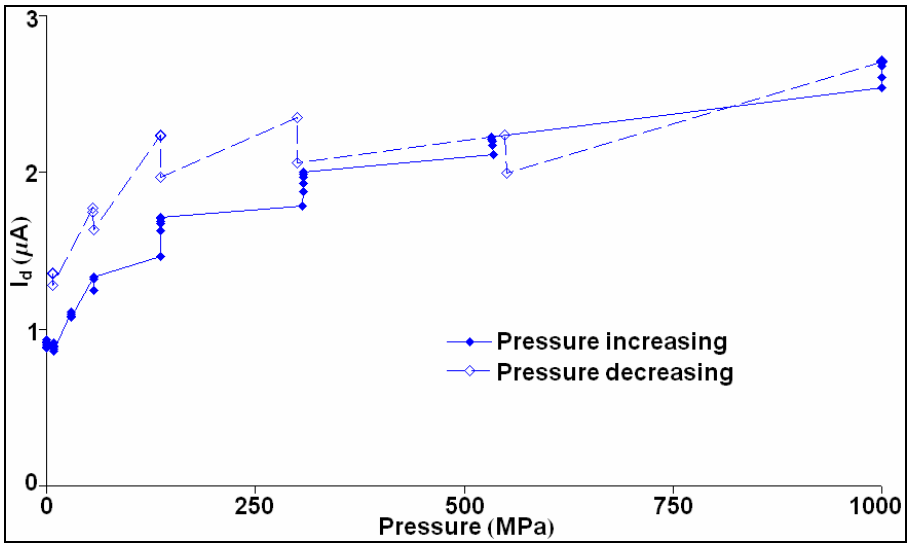

Figure C.2: Current versus pressure. V_{ds} = -10V. V_{gs} = -40V.

Mobility and threshold voltages versus pressure are shown in figure C.3.

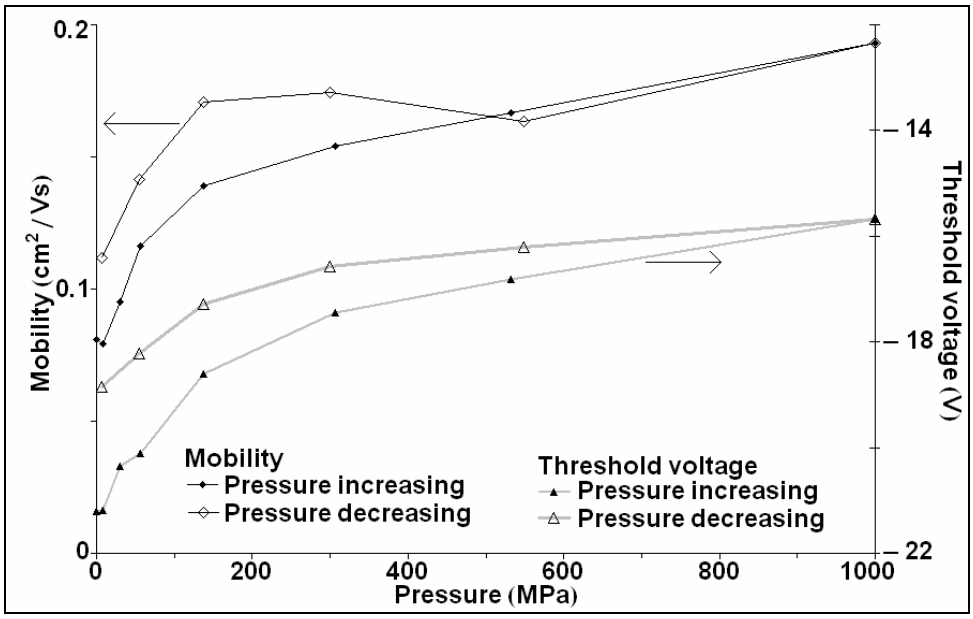

Figure C.3: Mobility (left scale) and threshold voltage (right scale) versus pressure. V_{ds} = -10V. V_{gs} = -40V.

Sample A shows good data. Additional samples are needed to show reproducibility. The sample is also older than the other samples, which may cause it to behave differently; for example sample A has the lowest initial mobility.

C.2 Sample B

The I_d-V_{gs} curves for the sample at various pressures are shown in figure C.4.

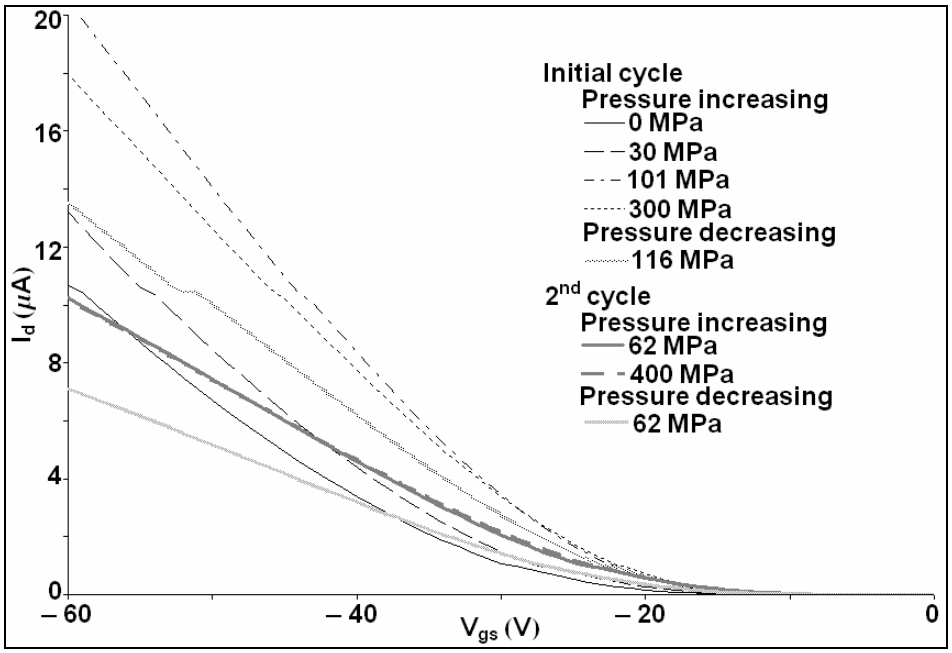

Figure C.4: I_d-V_{gs} for sample B under pressure. V_{ds} = -25V.

Tracking the current with pressure gives the plot shown in figure C.5.

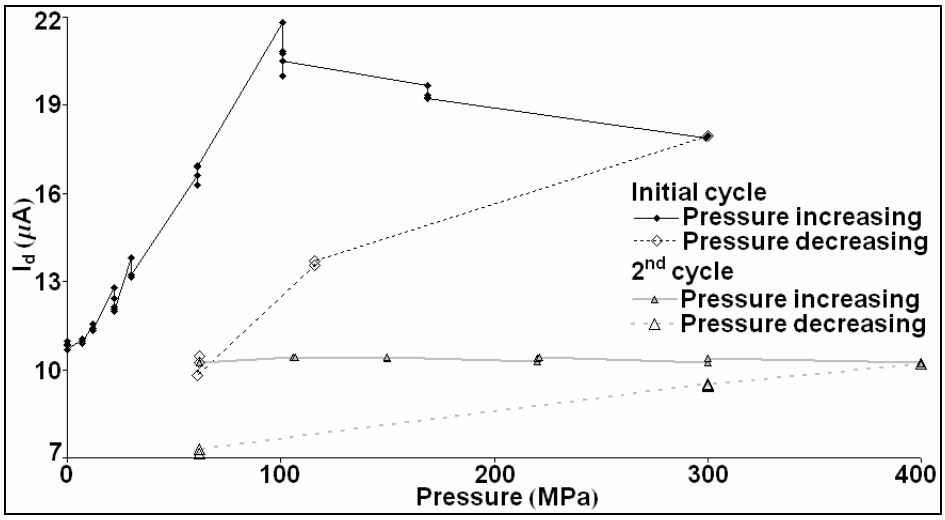

Figure C.5: Current versus pressure. V_{ds} = -25V. V_{gs} = -60V.

Clearly this sample is detrimentally affected by pressure. After initially pressurizing the sample to 300MPa and returning it to 60MPa the sample is again pressurized to determine if there is some kind of break-in effect. The second pressure cycle still results in degradation upon pressure release, indicating that the peak and degradation seen in the initial pressure cycle is not just a break-in effect.

Plotting the mobility and threshold voltage as a function of pressure is shown in figure C.6.

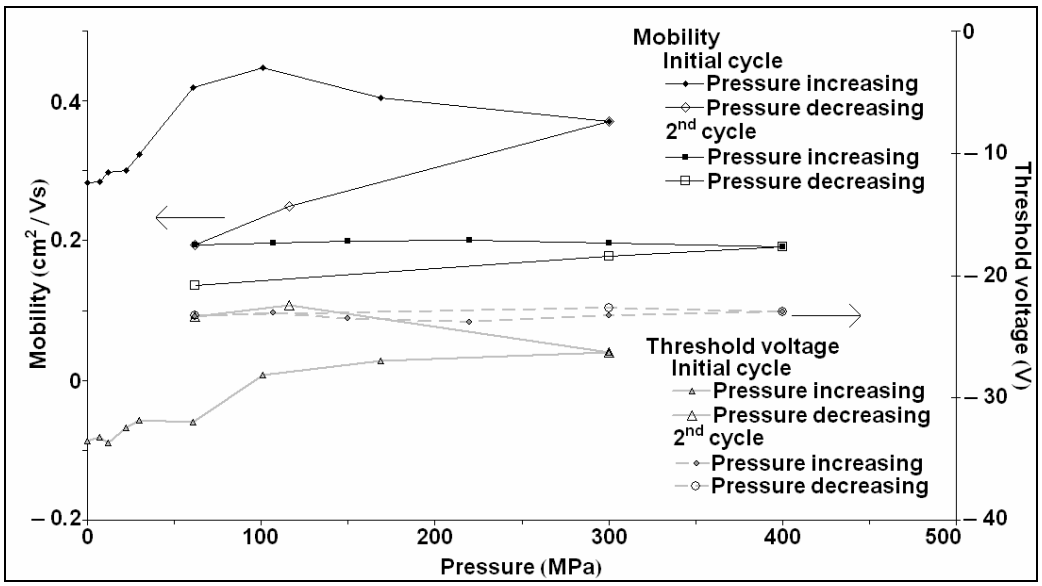

Figure C.6: Mobility (left scale) and threshold voltage (right scale) versus pressure. V_{ds} = -25V. V_{gs} = -60V.

The response for mobility and threshold largely mirrors the current response in figure C.5. The only controlled difference between sample A and B is that the pentacene layer on sample B is twice as thick and the substrate was not heated during deposition.

C.3 Sample C

The first iteration to try and match sample A is to mimic the pentacene layer thickness. Sample C is fabricated with 15nm (compared to 16nm for sample A) of pentacene. The I_d-V_{gs} curves for the sample at various pressures are shown in figure C.7.

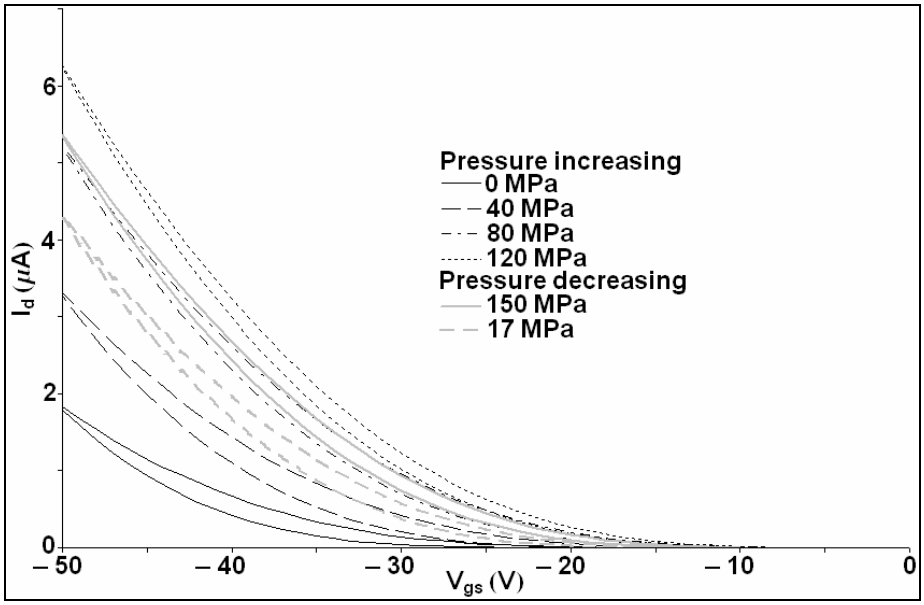

Figure C.7: I_d-V_{gs} for sample C under pressure. V_{ds} = -20V.

Tracking the current with pressure gives the plot shown in figure C.8.

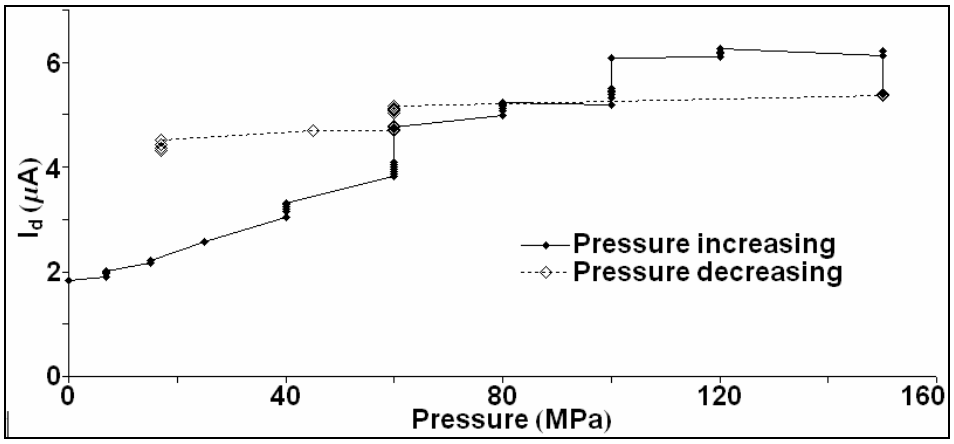

Figure C.8: Current versus pressure. V_{ds} = -20V. V_{gs} = -50V.

This sample shows a current peak near 120MPa. After reaching 150MPa the pressure run is stopped due to equipment issues. Once resolved, the pressure is ramped back down. The time taken fixing the equipment is the reason for the large drop at 150MPa.

Plotting the mobility and threshold voltage as a function of pressure is shown in figure C.9.

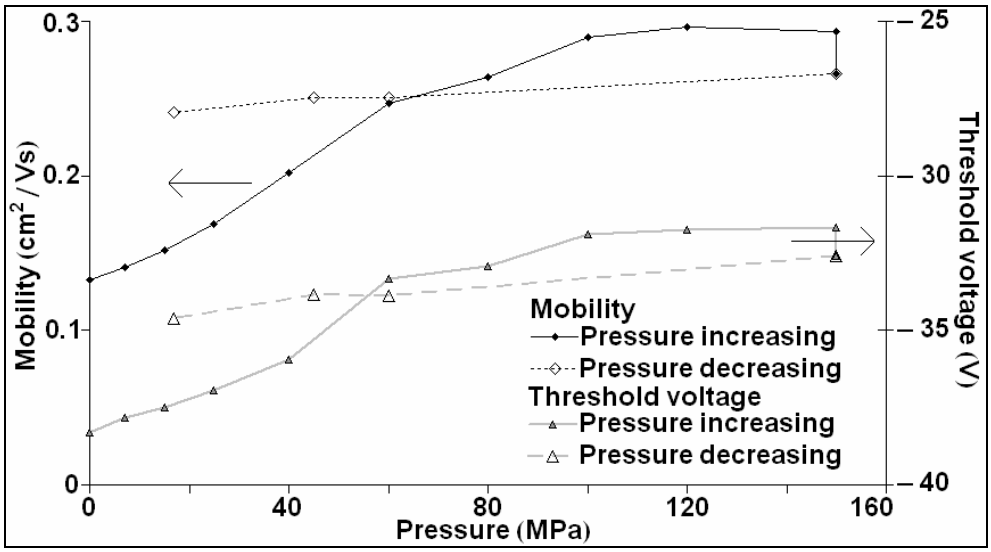

Figure C.9: Mobility (left scale) and threshold voltage (right scale) versus pressure. V_{ds} = -20V. V_{gs} = -50V.

C.4 Sample D

Some (40C) substrate heating is used when depositing the 15nm pentacene layer in sample D (sample A has a 16nm layer heated to 60C). The I_d-V_{gs} curves for the sample at various pressures are shown in figure C.10.

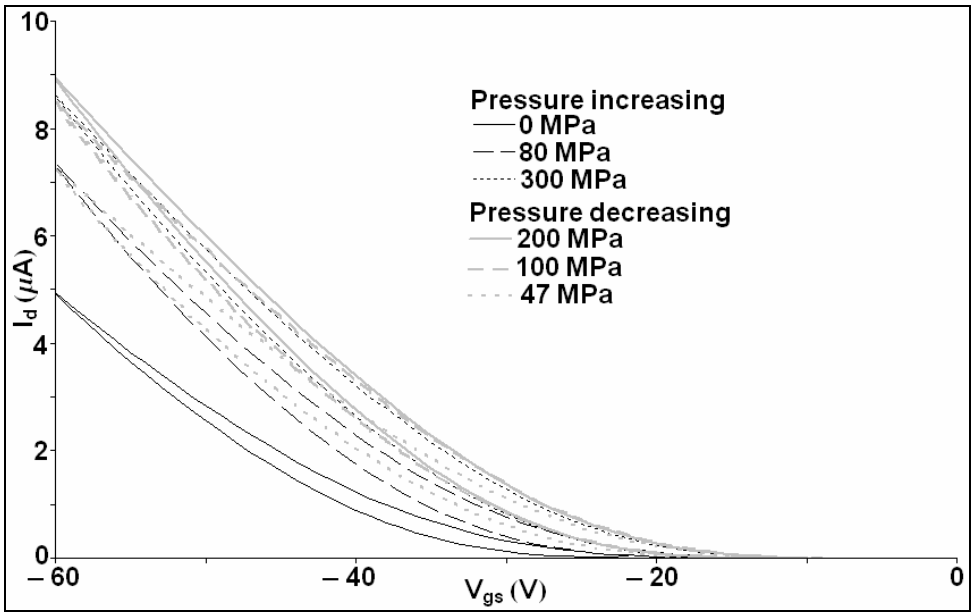

Figure C.10: I_d-V_{gs} for sample D under pressure. V_{ds} = -15V.

Tracking the current with pressure gives the plot shown in figure C.11.

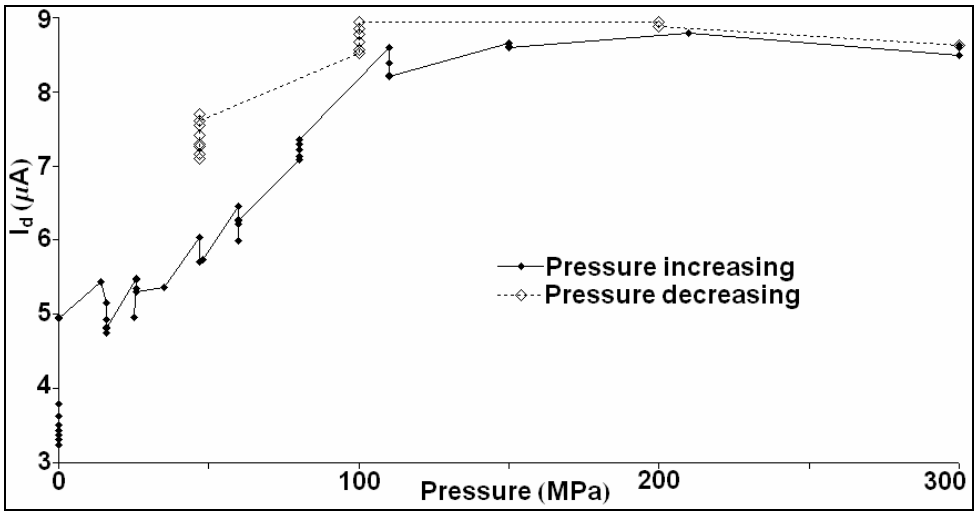

Figure C.11: Current versus pressure. V_{ds} = -15V. V_{gs} = -60V.

This sample shows some reasonable retrace data, a possible indication that the device response is getting closer to the response in sample A.

Plotting the mobility and threshold voltage as a function of pressure is shown in figure C.12.

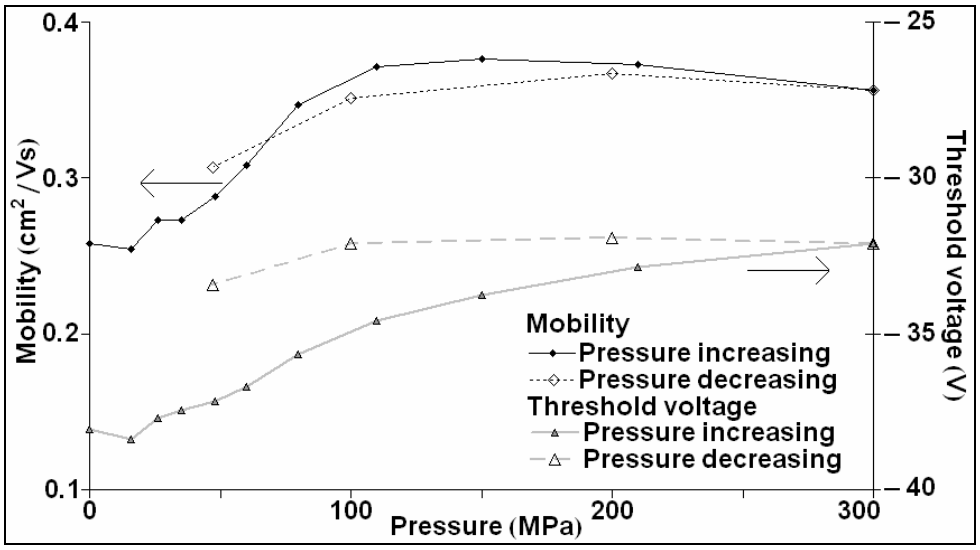

Figure C.12: Mobility (left scale) and threshold voltage (right scale) versus pressure. V_{ds} = -15V. V_{gs} = -60V.

The mobility also shows the retrace but the threshold voltage indicates a more persistent change with pressure.

C.5 Sample E

60C of substrate heating is used when depositing the 15nm pentacene layer in sample E, nearly the same as in sample A. The I_d-V_{gs} curves for the sample at various pressures are shown in figure C.13.

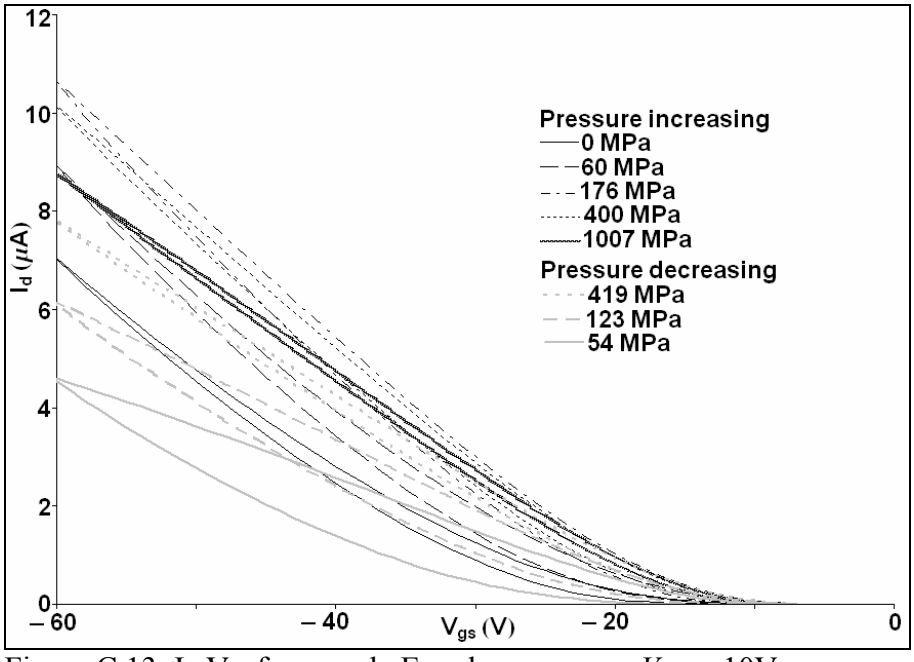

Figure C.13: I_d-V_{gs} for sample E under pressure. V_{ds} = -10V.

Tracking the current with pressure gives the plot shown in figure C.14.

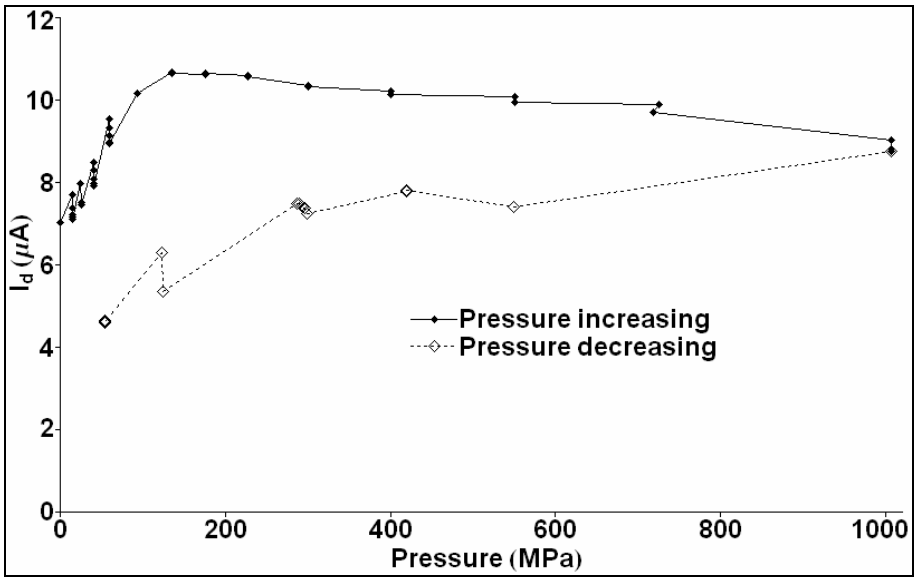

Figure C.14: Current versus pressure. V_{ds} = -10V. V_{gs} = -60V.

This sample is taken out to 1000MPa to test if the retrace emerging in sample D will withstand the full pressure range. The retrace is less than satisfactory but better than in sample B. Here the currents fall about 16% over 1GPa, sample B initially falls by about 17% over 0.3GPa.

Plotting the mobility and threshold voltage as a function of pressure is shown in figure C.15.

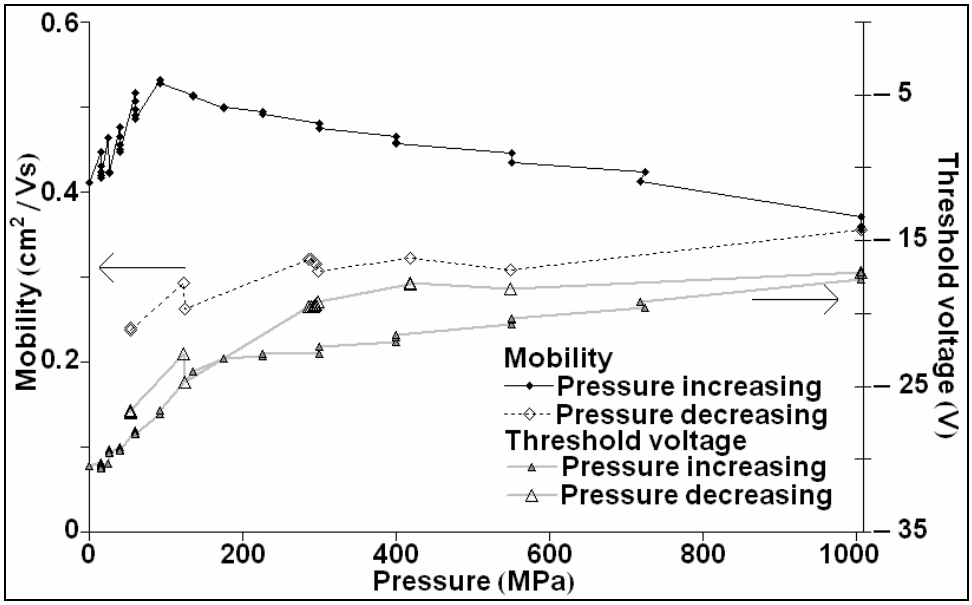

Figure C.15: Mobility (left scale) and threshold voltage (right scale) versus pressure. V_{ds} = -10V. V_{gs} = -60V.

Appendix D: Modeling a pentacene metal-semiconductor-metal structure

D.1 Introduction

While the preceding thesis focuses on the semiconductor materials' inherent transport properties, other transport phenomena need to be examined before useful applications can be developed. One of these phenomena is the metal/semiconductor carrier injection. As mentioned in chapter 4, pentacene is one of the most studied organic semiconductor materials and will be the focus of the calculations presented in this appendix.

This project takes data from different metal/pentacene/metal structures fabricated and tested by Dr. Lei Diao and applies a model to describe the material and contact properties.[98] The devices are substrates with gold, silver, or platinum deposited on them. Pentacene layers are deposited on top of these contacts. A final metal layer deposition of Au, Ag, or Pt is isolated within the pentacene layer to form the top contact.

The model treats the devices used in the experiment as ideal, with a uniform thin film and abrupt barriers at the contacts. Any imperfections are considered in terms of modifications of the code parameters, i.e. defining effective parameters. For example, changes in the order of the pentacene film will cause a variable mobility across the device; by averaging the mobilities throughout the layer a single effective mobility can be defined. This presents an option to further the work by replacing the effective parameters with modeled parameters. Within the mobility example, this would mean modeling how the pentacene mobility will respond to changes in the film order.

D.2 Model framework

Given the device geometry, a code originally developed by Drs. Davids, Campbell and Smith of Los Alamos National Laboratory for a layer of MEH-PPV between two metal contacts will be used as a starting point.[99] The model employs a relaxation method to solve the electrostatic problem in the device for equilibrium as the initial condition. To apply the model presented by Davids et al. to the devices used here, the treatment of the organic layer needs to be altered to allow for a higher mobility (pentacene's 0.1cm^2/Vs mobility versus MEH-PPV's $10^{-6}cm^2$/Vs), include a fixed space charge due to deep and slow traps, and include a bias dependent trap charge density associated with shallow and fast traps.

D.2.1 Equilibrium

To find the equilibrium condition for the device, the code solves the Poisson equation and the charge carrier density relations. The Poisson equation, shown in equation D.1, also illustrates where the trap and impurity charges are entered into the code.

$$-\frac{\partial^2 \phi}{\partial x^2} = \frac{\partial E}{\partial x} = \frac{4\pi e}{\varepsilon}\rho(x)$$
$$\rho(x) = p - n + r_d + r_{sh}$$

Equation D.1

φ is the potential in the pentacene layer; E is the electric field through the device; ε is the pentacene dielectric constant; e is the electron charge; $\rho(x)$ is the charge profile of the pentacene layer. The charge profile consists of holes (p), electrons (n), a fixed charge density (r_d), and a variable shallow trapped charge density (r_{sh}). The hole and electron charges are related to the potential through the relations shown in equation D.2.

$$n = N_0 \exp(\frac{\Psi_F - \Psi_C}{kT})$$
$$p = N_0 \exp(\frac{\Psi_V - \Psi_F}{kT})$$

Equation D.2

While in equilibrium, the Fermi level can be taken as the metal's Fermi level throughout the device, allowing the potential to describe the energy separation by taking the left contact metal's Fermi level to be zero potential.

$$n(x) = N_0 \exp(\frac{-e(\phi_b + \phi(x))}{kT})$$
$$p(x) = N_0 \exp(\frac{e(\phi_b + \phi(x) - E_G)}{kT})$$

Equation D.3

φ_b is the metal to semiconductor potential barrier at the left contact. N_0 is the effective density of states, estimated as the density of molecules in the pentacene film. kT is the thermal energy and E_G is the band gap. Within this project the material is assumed to be hole dominated, allowing the gap to be chosen arbitrarily large to eliminate the effects associated with electrons. The fixed charge (r_d) is a user entered constant. The trapped charge (r_{sh}) can be written as:

$$r_{sh} = \frac{N_T}{1 + \exp\left(\frac{\Psi_F - \Psi_T^*}{kT}\right)}$$
$$p = N_0 \exp(\frac{\Psi_V - \Psi_F}{kT})$$
$$\Psi_F = kT \ln(\frac{N_0}{p}) + \Psi_V$$
$$r_{sh} = \frac{N_T}{1 + \exp(\frac{kT \ln(\frac{N_0}{p}) + \Psi_V - \Psi_T^*}{kT})} = \frac{N_T}{1 + \frac{N_0}{p}\exp\left(\frac{\Psi_V - \Psi_T^*}{kT}\right)}$$

Equation D.4

In this relation N_T (the trap site density) and Ψ_V-Ψ_T^* (the valence band and trap energy separation) are entered as user controlled parameters, leaving only the hole concentration variable.

A numeric double integration is used to solve for the equilibrium potential in the device. This integration employs a relaxation technique and requires two boundary conditions. One of the conditions is chosen as the potential at one contact which is set to zero. The other initial condition is the field at this point, which must be found. A shooting method is used to solve for the potential at the other contact. When that calculated potential matches the built in voltage, the shooting method has converged.

D.2.2 Steady state, non-equilibrium condition

Each steady state condition will start from the equilibrium condition and relax to a converged solution for a unique applied voltage. To calculate the currents in the device the current continuity equations are used:

$$\frac{\partial n}{\partial t} = G - R + \frac{1}{e}\frac{\partial J_n}{\partial x}$$
$$\frac{\partial p}{\partial t} = G - R - \frac{1}{e}\frac{\partial J_p}{\partial x} \qquad \text{Equation D.5}$$

G and R are the generation and recombination rates of the carriers. For these devices, with hole dominated currents, the generation and recombination rates are negligible. The current densities (J_n and J_p) are the drift/diffusion currents, written in the Scharfetter-Gummel discritization as:

$$J_n = e\mu_n E\left(\frac{n(N+1)}{1-\exp(-\frac{eE}{kT}\Delta x)} + \frac{n(N)}{1-\exp(\frac{eE}{kT}\Delta x)}\right)$$
$$J_p = e\mu_p E\left(\frac{p(N+1)}{1-\exp(+\frac{eE}{kT}\Delta x)} + \frac{p(N)}{1-\exp(\frac{-eE}{kT}\Delta x)}\right)$$

Equation D.6

μ is the mobility of the pentacene layer (user entered parameter) and *N* is the index of the grid point being calculated.

This creates equations D.1, D.2, and D.5 that depend on the potential, electric field, and carrier concentrations. The bias for the steady state condition is entered through small perturbations on the potential at the contacts, which the relaxation method will transmit to the full device. The steady state condition is considered converged when the total current becomes position independent within prescribed accuracy limits.

With the potential and carrier concentration known, quasi-Fermi levels can be found by:

$$\Psi_{nf} = E_C + kT\log(\frac{n}{N_0})$$
$$\Psi_{pf} = E_V - kT\log(\frac{p}{N_0})$$

Equation D.7

Ψ_{nf} and Ψ_{pf} stand for the quasi-Fermi energy level.

D.2.3 Injection currents

Injection currents are independently calculated to provide a boundary condition for the non-equilibrium currents. The injection currents included within this model are the thermionic injection, tunneling, and interface recombination (backflow) currents. The thermionic injection current follows the relation:

$$J_{th} = AT^2 \exp(\frac{-\phi_B}{kT}) \qquad \text{Equation D.8}$$

A is the Richardson constant. φ_B is the contact barrier to injection. The barrier is allowed to be altered by image force lowering under proper biasing conditions; for the hole carrier device the injecting contact will need to be positively biased beyond the built in potential. The lowering considered here assumes a modified potential:

$$\phi(x) = \chi_b - E\,x - \frac{e}{\varepsilon\,x} \qquad \text{Equation D.9}$$

Finding the maximum, the new modified potential barrier is defined as:

$$\phi_B = \chi_b - e\,\Delta\phi$$
$$\Delta\phi = \sqrt{\frac{eE}{\varepsilon}} \qquad \text{Equation D.10}$$

In this relation E is the field at the contact and X_b is work function difference between the metal contact and the pentacene (original barrier).

The tunneling current takes the potential of equation D.9 and applies a WKB approximation to obtain the carrier transmission coefficients, equation D.11; ħ is $h/2\pi$ and m is the mass of an electron.

$$Tr(E) \cong \exp(-2\,\xi)$$
$$\xi = \frac{1}{\hbar}\int \sqrt{2m(\phi(x) - E)}\,dx \qquad \text{Equation D.11}$$

The final element of the injection currents is the interface recombination. This current arises from the fact that the mobilities in the pentacene film are small enough that the injected charges can build up at the contact faster than they can diffuse or drift into the film. This creates an excess of charge in one location, close to the contact that injected it, forcing some of the carriers to flow back into the contact. The hole diffusion

current back into the contacts is approximated by equation D.12, with all bias effects contained in the local carrier concentration value.

$$J_{bf} = e\upsilon\, p_{\text{contact}} \qquad \text{Equation D.12}$$

The proportionality constant in the relation, υ, can be found through detailed balance when considering the equilibrium state; here the tunneling current is zero and the total current also vanishes. Equating the thermionic current and backflow current at equilibrium leaves the constant determined as:

$$\upsilon = \frac{AT^2 \exp(\frac{-\phi_{B0}}{kT})}{p_{c0}} = \frac{AT^2}{N_0} \qquad \text{Equation D.13}$$

p_{c0} is a special form of p_{contact} (the hole concentration at the contact), identifying it as the equilibrium p_{contact} value.

D.3 Applying the code to actual devices

Data from three devices matching the setup that this code is meant to model is provided by Dr. Diao. The devices are constructed with both contacts made of the same metal (one device each with gold, silver, and platinum contacts). The data on each device spans a bias from -1 to 1V. The data is modeled from 0 to 1V (the 0 to -1V data would be redundant). The following parameters are held constant for this pentacene device; temperature = 300K, thickness = 250nm, ε = 4, $N_0 = 5.8\text{x}10^{21}\text{cm}^{-3}$, and $E_g = 2.4$eV. The dielectric constant is not well known but does not affect the I-V calculation much. The contact hole barrier heights and mobility have target values that are used to assist in the

modeling but are not considered fixed. The trap energy is chosen as $\Psi_T^*-\Psi_V = 0.29eV$ based on activation energy measurement made by Dr. Diao.

For all three devices, physically reasonable parameter sets are found that can model the experimental data. Unfortunately the parameter sets are not unique. Figure D.1 displays the experimental data and nine different modeled fits. The parameters used in the fits are listed in table D.1. A common mobility of $0.01cm^2/V\ s$ and a fixed charge concentration of $4x10^{15}cm^{-3}$ can be used to match each experimental data set. The order of the barriers for the symmetric devices are consistent with what was measured by Dr. Diao, in that the order was platinum with the lowest hole barrier, then gold, and silver following. Changes in the trap site concentration seem to be more important in the lower barrier contact metals; removal of the trapped charge did little to the silver device (highest barrier) but required an increase in the modeled barrier heights for gold and platinum (to fit the experimental data). Clearly, trade-offs between the effects associated with different phenomena (and parameters) are possible at this time, and only more experimental results that determine more of the essentially unknown parameters can remove the ambiguity.

Fit number	Contact metal	Hole barrier (eV)	Mobility (cm^2/Vs)	Fixed charge density (cm^{-3})	Trapped charge density (cm^{-3})
1	Pt	0.45	0.01	$7.5x10^{15}$	$1x10^{20}$
2	Pt	0.56	0.01	$3.5x10^{15}$	0
3	Pt	0.55	0.01	$4x10^{15}$	0
4	Au	0.53	0.002	$6x10^{15}$	$1x10^{20}$
5	Au	0.62	0.01	$4x10^{15}$	0
6	Au	0.56	0.001	$4x10^{15}$	0
7	Au	0.5	0.0001	$4x10^{15}$	0
8	Ag	0.695	0.01	$3.75x10^{15}$	$5x10^{20}$
9	Ag	0.695	0.01	$3.75x10^{15}$	0

Table D.1: Summary of parameters for the modeled curves in figure D.1. The "Fit number" column identifies the modeled fit in figure D.1 with the parameter set listed here.

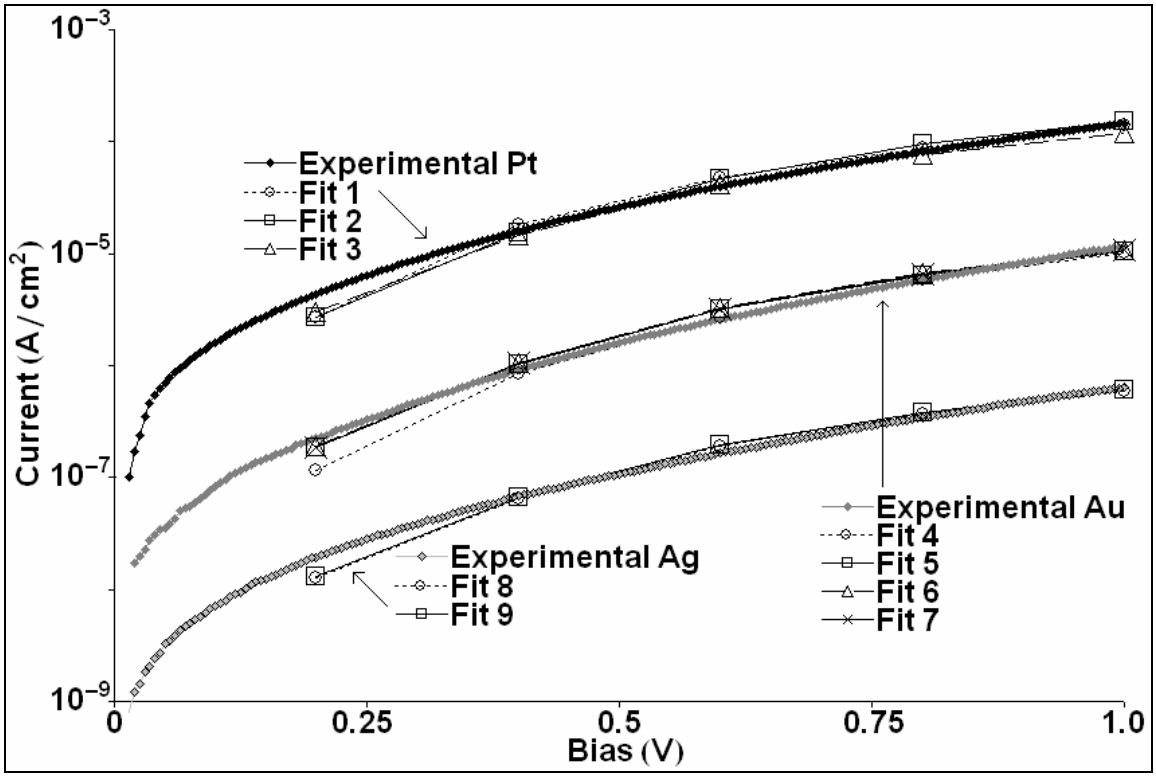

Figure D.1: Plot of the experimental data and modeled fits for the metal/pentacene/metal device.

References:

[1] H. Sirringhaus, P. J. Brown, R. H. Friend, M. M. Nielsen, K. Bechgaard, B. M. W. Langeveol-Voss, A. J. H. Spiering, R. A. J. Janssen, E. W. Meijer, P. Herwig, and D. M. Leeuw, "Two-dimensional charge transport in self-organized, high-mobility conjugated polymers," *Nature*, **401**, 685 (1999).

[2] H. Sirringhaus, N. Tessler, and R. H. Friend, "Integrated, high-mobility polymer field-effect transistors driving polymer light-emitting diodes," *Synthetic Met.*, **102**, 857 (1999).

[3] Z. Bao, A. Dodabalapur, and A. J. Lovinger, "Soluble and processable regioregular poly(3-hexylthiophene) for thin film field-effect transistor applications with high mobility," *Appl. Phys. Lett.*, **69**(26), 4108 (1996).

[4] S. F. Nelson, Y. –Y. Lin, D. J. Gundlach, and T. N. Jackson, "Temperature-independent transport in high-mobility pentacene transistors," *Appl. Phys. Lett.*, **72**(15), 1854 (1998).

[5] Y. –Y. Lin, D. J. Gundlach, S. F. Nelson, and T. N. Jackson, "Stacked pentacene layer organic thin-film transistor with improved characteristics," *IEEE Electr. Device L.*, **18**(12), 606 (1997).

[6] Y. –Y. Lin, D. J. Gundlach, S. F. Nelson, and T. N. Jackson, "Pentacene-based organic thin-film transistors," *IEEE T. Electron Dev.,* **44**(8), 1325 (1997).

[7] D. J. Gundlach, Y. –Y. Lin, T. N. Jackson, S. F. Nelson, and D. G. Schlom, "Pentacene organic thin-film transistors – Molecular ordering and mobility," *IEEE Electr. Device L.,* **18**(3), 87 (1997).

[8] P. F. Baude, D. A. Ender, M. A. Haase, T. W. Kelley, D. V. Muyres, and S. D. Theiss, "Pentacene-based radio-frequency identification circuitry," *Appl. Phys. Lett.*, **82**(22), 3964 (2003).

[9] K. Nomoto, N. Hirai, N. Yoneya, N. Kawashima, M. Noda, M. Wada, and J. Kasahara, "A high-performance short-channel bottom-contact OTFT and its application to AM-TN-LCD," *IEEE T. Electron Dev.*, **52**(7), 1519 (2005).

[10] Y. Wang, H. Cheng, Y. Wang, T. Hu, J. Ho, C. Lee, T. Lei, and C. Yeh, "Pentacene-based thin film transistors used to drive a twist-nematic liquid crystal display," *Thin Solid Films*, **491**, 305 (2005).

[11] W. Clemens, W. Fix, J. Ficker, A. Knobloch, and A. Ullman, "From polymer transistors toward printed electronics," *J. Mater. Res.*, **19**(7), 1963 (2004).

[12] G. Li, V. Shrotriya, J. Huang, Y. Yao, T. Moriarty, K. Emery, and Y. Yang, "High-effeciency solution processable polymer photovoltaic cells by self-organization of polymer blends," *Nat. Mater.*, **4**, 864 (2005).

[13] J. A. Rogers, Z. Bao, A. Dodabalapur, and A. Makhija, "Organic smart pixels and complementary inverter circuits formed on plastic substrates by casting and rubber stamping," *IEEE Electr. Device L.*, **21**(3), 100 (2000).

[14] H. Sirringhaus, N. Tessler, and R. H. Friend, "Integrated optoelectronic devices based on conjugated polymers," *Science*, **280**, 1741 (1998).

[15] J. Wu, J. Zang, B. Larade, H. Guo, X. G. Gong, and F. Liu, "Computational design of carbon nanotube electromechanical pressure sensors," *Phys. Rev. B,* **69**, 153406-1 (2004).

[16] J. G. Lee, Y. G. Seol, and N. –E. Lee, "Polymer thin film transistor with electroplated source and drain electrodes on a flexible substrate," *Thin Solid Films*, **515**, 805 (2006).

[17] S. K. Park, Y. H. Kim, J. I. Han, D. G. Moon, W. K. Kim, and M. G. Kwak, "Electrical characteristics of poly (3-hexylthiophene) thin film transistors printed and spin-coated on plastic substrates," *Synthetic Met.*, **139**, 377 (2003).

[18] Y. H. Kim, S. K. Park, D. G. Moon, W. K. Kim, and J. I. Han, "Organic thin film transistor-driven liquid crystal display on flexible polymer substrate," *Jpn. J. Appl. Phys.*, **43**(6A), 3605 (2004).

[19] S. E. Fritz, T. W. Kelley, and C. D. Frisbie, "Effect of dielectric roughness on performance of pentacene TFTs and restoration of performance with a polymeric smoothing layer," *J. Phys. Chem. B*, **109**, 10574 (2005).

[20] H. Yang, T. J. Shin, L. Yang, K. Cho, C. Y. Tyu, and Z. Bao, "Effect of mesoscale crystalline structure of the field-effect mobility of regioregular poly(3-hexyl thiophene) in thin-film transistors," *Adv. Funct. Mater.*, **15**, 671 (2005).

[21] A. Zen, J. Pflaum, S. Hirschmann, W. Zhuang, F. Jaiser, U. Asawapirom, J. P. Rabe, U. Scherf, and D. Neher, "Effect of molecular weight and annealing of poly(3-hexylthiophene)s on the performance of organic field-effect transistors," *Adv. Funct. Mater.*, **14**(8), 757 (2004).

[22] J. Chang, B. Sun, D. W. Breiby, M. M. Nielsen, T. I. Solling, M. Giles, I. McCulloch, and H. Sirringhaus, "Enhanced mobility of poly(3-hexylthiophene) transistors by spin-coating from high-boiling-point solvents," *Chem. Mater.*, **16**, 4772 (2004).

[23] S. K. Park, T. N. Jackson, J. E. Anthony, and D. A. Mourey, "High mobility solution processed 6, 13-bis(triisopropyl-silylethynyl) pentacene organic thin film transistors," *Appl. Phys. Lett.*, **91**, 063514 (2007).

[24] S. K. Park, Y. H. Kim, J. I. Han, D. G. Moon, and W. K. Kim, "High-performance polymer TFTs printed on a plastic substrate," *IEEE T. Electron Dev.*, **49**(11), 2008 (2002).

[25] G. Wang, T. Hirasa, D. Moses, and A. J. Heeger, "Fabrication of regioregular poly(3-hexylthiophene) field-effect transistors by dip-coating," *Synthetic Met.*, **146**, 127 (2004).

[26] S. Cho, K. Lee, J. Yuen, G. Wang, D. Moses, A. J. Heeger, M. Surin, and R. Lazzaroni, "Thermal annealing-induced enhancement of the field-effect mobility of regioregular poly(3-hexylthiophene) films," *J. Appl. Phys.*, **100**, 114503 (2006).

[27] G. Wang, J. Swensen, D. Moses, and A. J. Heeger, "Increased mobility from regioregular poly(3-hexylthiophene) field-effect transistors," *J. Appl. Phys.*, **93**(10), 6137 (2003).

[28] M. M. Ling and Z. Bao, "Thin film deposition, patterning, and printing in organic thin film transistors," *Chem. Mater.*, **16**, 4824 (2004).

[29] R. Ruiz, D. Choudhary, B. Nickel, T. Toccoli, K. Chang, A. C. Mayer, P. Clancy, J. M. Blakely, R. L. Headrick, S. Iannotta, and G. G. Malliaras, "Pentacene thin film growth," *Chem. Mater.*, **16**, 4497 (2004).

[30] H. Kakuta, T. Hirahara, I. Matsuda, T. Nagao, S. Hasegawa, N. Ueno, and K. Sakamoto, "Electronic structures of highest occupied molecular orbital bands of a pentacene ultrathin film," *Phys. Rev. Lett.*, **98**, 247601 (2007).

[31] V. Podzorov, E. Menard, J. A. Rogers, and M. E. Gershenson, "Hall effect in the accumulation layers on a surface of organic semiconductors," *Phys. Rev. Lett.*, **95**, 226601 (2005).

[32] A. N. Aleshin, H. Sandberg, and H. Stubb, "Two-dimensional charge carrier mobility studies of regioregular P3HT," *Synthetic Met.*, **121**, 1449 (2001).

[33] E. J. Meijer, M. Matters, P. T. Herwig, D. M. de Leeuw, and T. M. Klapwijk, "The Meyer-Neldel rule in organic thin-film transistors," *Appl. Phys. Lett.*, **76**(23), 3433 (2000).

[34] B. Liu, B. Sundqvist, O. Andersson, T. Wagberg, E. B. Nyeanchi, X. M. Zhu, and G. Zou, "Electric resistance of single-walled carbon nanotubes under hydrostatic pressure," *Solid State Commun.,* **118**, 31 (2001).

[35] C. R. Newman, R. J. Chesterfield, J. A. Merlo, and C. D. Frisbie, "Transport properties of single-crystal tetracene field-effect transistors with silicon dioxide gate dielectric," *Appl. Phys. Lett.*, **85**(3), 422 (2004).

[36] O. D. Jurchescu, J. Baas, and T. T. M. Polstra, "Effect of impurities on the mobility of single crystal pentacene," *Appl. Phys. Lett.*, **84**(16), 3061 (2004).

[37] M. Oehzelt, K. Weinmeier, G. Heimel, P. Puschnig, R. Resel, C. Ambrosch-Draxl, F. Porsch, and A. Nakayama, "Structural properties of anthracene under high pressure," *High Pressure Res.*, **22**, 343 (2002).

[38] A. M. Pivovar, J. E. Curtis, J. B. Leao, R. J. Chesterfield, and C. D. Frisbie, "Structural and vibrational characterization of the organic semiconductor tetracene as a function of pressure and temperature," *Chem. Phys.*, **325**, 138 (2006).

[39] S. E. Fritz, S. M. Martin, C. D. Firsbie, M. D. Ward, and M. F. Toney, "Structural characterization of a pentacene monolayer on an amorphous SiO_2 substrate with grazing incidence X-ray diffraction," *J. Am. Chem. Soc.*, **126**, 4084 (2004).

[40] M. W. Burand, K. A. McGee, X. Cai, D. A. da Silva Filho, J. –L Bredas, C. D. Frisbie, and K. R. Mann, "Synthesis, X-ray, spectroelectrochemical, and theoretical studies of a tricyanovinyl-capped quaterthiophene: A correlation of semiconductor performance with physical properties," *Chem. Phys. Lett.*, **425**, 251 (2006).

[41] T. M. Pappenfus, R. J. Chesterfield, C. D. Frisbie, K. R. Mann, J. Casado, J. D. Raff, and L. L. Miller, "A π-stacking terthiophene-based quinodimethane is an n-channel conductor in a thin film transistor," *J. Am. Chem. Soc.*, **124**, 4184 (2002).

[42] R. J. Chesterfield, C. R. Newman, T. M. Pappenfus, P. C. Ewbank, M. H. Haukaas, K. R. Mann, L. L. Miller, and C. D. Frisbie, "High electron mobility and ambipolar transport in organic thin-film transistors based on a π-stacking quinoidal terthiophene," *Adv. Mater.*, **15**(15), 1278 (2003).

[43] O. Berg, and E. L. Chronister, "Optical dephasing in pentacene-doped PMMA under high pressure," *J. Chem. Phys.*, **106**(11), 4401 (1997).

[44] B. J. Baer and E. L. Chronister, "The effect of pressure on the fluorescene lifetime of pentacene in *para*-terphenyl at low temperature," *J. Chem. Phys.*, **100**(1), 23 (1994).

[45] P. Puschnig, G. Heimel, K. Weinmeier, R. Resel, and C. Ambrosch-Draxl, "High pressure studies on the optical and electronic properties of *prar*-terphenyl," *High Pressure Res.*, **22**, 105 (2002).

[46] M. Croci, H. Muschenborn, F. Guttler, A. Renn, and U. P. Wild, "Single molecule spectroscopy: pressure effect on pentacene in *p*-terphenyl," *Chem. Phys. Lett.*, **212**(1), 71 (1993).

[47] M. S. Amer, M. M. El-Ashry, and J. F. Maguire, "Study of the hydrostatic pressure dependence of the Raman spectrum of single-walled carbon nanotubes and nanospheres," *J. Chem. Phys.,* **121**(6), 2752 (2004).

[48] W. Yang, R. Z. Wang, X. M. Song, B. Wang, and H. Yan, "Pressure-induced Raman-active radial breathing mode transistion in single-wall carbon nanotubes," *Phys. Rev. B,* **75**, 045425-1 (2007).

[49] J. Wu, W. Walukiewicz, W. Shan, E. Bourret-Courchesne, J. W. Ager III, K. M. Yu, E. E. Haller, K. Kissell, S. M. Bachilo, R. B. Weisman and R. E. Smalley, "Structure-dependent hydrostatic deformation potentials of individual single-walled carbon nanotubes," *Phys. Rev. Lett.,* **93**(1), 017404-1 (2004).

[50] L. Farina, A. Brillante, R. G. Della Valle, E. Venuti, M. Amboage, and K. Syassen, "Pressure-induced phase transition in pentacene.," *Chem. Phys. Lett.*, **375**, 490 (2003).

[51] L. Farina, K. Syassen, A. Brillante, R. G. Della Valle E. Venuti, and N. Karl, "Pentacene at high pressure," *High Pressure Res.*, **23**(3), 349 (2003).

[52] E. Venuti, R. G. D. Valle, L. Farina, and A. Brillante, "Phonons and structures of tetracene polymorphs at low temperature and high pressure," *Phys. Rev. B*, **70**, 104106 (2004).

[53] Z. Rang, A. Haraldsson, D. M. Kim, P. P. Ruden, R. J. Chesterfield, and C. D. Frisbie, "Hydrostatic-pressure dependence of the photoconductivity of single-crystal pentacene and tetracene," *Appl. Phys. Lett.*, **79**(17), 2731 (2001).

[54] O. Madelung, *Introduction to Solid-State Theory*, Springer-Verlag, New York, 448 (1978).

[55] C. Kittel, *Introduction to Solid State Physics, 7th ed.*, John Wiley and Sons, New York, 245 (1996).

[56] Y. D. Park, J. H. Cho, D. H. Kim, Y. Jang, H. S. Lee, K. Ihm, T. Kang, and K. Cho, "Energy-level alignment at interfaces between gold and poly(3-hexylthiophene) films with two different molecular structures," *Electrochem. Solid St.*, **9**(11), G317 (2006).

[57] R. J. Klien, M. D. Mcgehee, and M. F. Toney, "Highly oriented crystals at the buried interface in polythiophene thin-film transistors," *Nat. Mater.*, **5**, 222 (2006).

[58] H. G. O. Sandberg, G. L. Frey, M. N. Shkunov, H. Sirringhaus, R. H. Friend, M. M. Nielsen, and C. Kumpf, "Ultrathin regioregular poly(3-hexyl thiophene) field-effect transistors," *Langmuir*, **18**, 10176 (2002).

[59] X. M. Jiang, R. Osterbacka, O. Korovyanko, C. P. An, B. Horovitz, R. A. Janssen, and Z. V. Vardeny, "Spectroscopic studies of photoexcitations in regioregular and regiorandom polythiophene films," *Adv. Funct. Mater.*, **12**(9), 587 (2002).

[60] R. Osterbacka, C. P. An, X. M. Jiang, and Z. V. Vardeny, "Two-dimensional electronic excitations in self-assembled conjugated polymer nanocrystals," *Science*, **287**, 839 (2000).

[61] D. D. Schroepfer, P. P. Ruden, Y. Xia, C. D. Frisbie, and S. E. Shaheen, "Hydrostatic pressure effects on poly(3-hexylthiophene) thin film transistors," *Appl. Phys. Lett.*, **92**, 013305 (2008).

[62] E. J. Meijer, C. Detcheverry, P. J. Baesjou, E. van Veenandaal, D. M. de Leeuw, and T. M. Klapwijk, "Dopant density determination in disordered organic field-effect transistors," *J. Appl. Phys.*, **93**(8), 4831 (2003).

[63] H. Nishimura, M. Iizuka, M. Sakai, M. Nakamura, and K. Kudo, "Poly(3-hexylthiophene) field-effect transistor with controllable threshold voltage," *Jpn. J. Appl. Phys.,* **44**(1B), 621 (2005).

[64] S. Wang, J. Lou, B. Liou, R. Lin, and C. Yeh, "Process improvement and reliability characteristics of spin-on poly-3-hexylthiophene thin-film transistor," *J. Electrochem. Soc.*, **152**(1), G50 (2005).

[65] Z. Rang, M. I. Nathan, P. P. Ruden, V. Podzorov, M. E. Gershenson, C. R. Newman, and C. D. Frisbie, "Hydrostatic pressure dependence of charge carrier transport in single-crystal rubrene devices," *Appl. Phys. Lett.*, **86**, 123501 (2005).

[66] Z. Rang, M. I. Nathan, P. P. Ruden, R. Chesterfield, and C. D. Frisbie, "Hydrostatic-pressure dependence of organic thin-film transistor current versus voltage characteristics," *Appl. Phys. Lett.*, **85**(23), 5760 (2004).

[67] J. Zaumseil, K. W. Baldwin, and J. A. Rodgers, "Contact resistance in organic transistors that use source and drain electrodes formed by soft contact lamination," *J. Appl. Phys.*, **93**(10), 6117 (2003).

[68] J. Zaumsiel, T. Someya, Z. Bao, Y. Loo, R. Cirelli, and J. A. Rodgers, "Nanoscale organic transistors that use source/drain electrodes supported by high resolution rubber stamps," *Appl. Phys. Lett.*, **82**(5), 793 (2003).

[69] H. E. Katz, "Recent advances in semiconductor performance and printing processes for organic transistor-based electronics," *Chem. Mater.*, **16**, 4748 (2004).

[70] A. Facchetti, M. Yoon, and T. J. Marks, "Gate dielectrics for organic field-effect transistors: new opportunities for organic electronics," *Adv. Mater.*, **17**, 1705 (2005).

[71] T. W. Kelley, P. F. Baude, C. Gerlach, D. E. Ender, D. Muyres, M. A. Haase, D. E. Vogel, and S. D. Theiss, "Recent progress in organic electronics: Materials, devices, and processes," *Chem. Mater.,* **16**, 4413 (2004).

[72] T. W. Kelley, L. D. Boardman, T. D. Dunbar, D. V. Muyres, M. J. Pellerite, and T. P. Smith, "High-performance OTFTs using surface-modified alumina dielectrics," *J. Phys. Chem. B*, **107**, 5877 (2003).

[73] G. Darlinski, U. Bottger, R. Waser, H. Klauk, M. Halik, U. Zschieschang, G. Schmid, and C. Dehm, "Mechanical force sensors using organic thin-film transistors," *J. Appl. Phys.*, **97**, 093708 (2005).

[74] G. A. Samara and H. G. Drickamer, "Effect of pressure on the resistance of fused-ring aromatic compounds," *J. Chem. Phys.*, **37**(3), 474 (1962).

[75] Y. Liang, C. D. Frisbie, H. –C, Chang, and P. P. Ruden, "Conducting channel formation and annihilation in organic field-effect structures," submitted.

[76] E. T. Thostenson, Z. Ren, and T. –W Chou, "Advances in the science and technology of carbon nanotubes and their composites: a review," *Compos. Sci. Technol.*, **61**, 1899 (2001).

[77] J. N. Coleman, U. Khan, W. J. Blau, and Y. K. Gun'ko, "Small but strong: A review of the mechanical properties of carbon nanotube-polymer composites," *Carbon*, **44**, 1624 (2006).

[78] J. –P. Salvetat-Delmotte and A. Rubio, "Mechanical properties of carbon nanotubes: a fiber degest for beginners," *Carbon*, **40**, 1729 (2002).

[79] C. L. Erik, T. Thostenson, and T. –W. Chou, "Sensors and actuators based on carbon nanotubes and their composites: A review," *Compos. Sci. Technol.*, **68**, 1227 (2008).

[80] M. S. Dresselhaus, G. Dresselhaus, J. C. Charlier, and E. Hernandez, "Electronic, thermal and mechanical properties of carbon nanotubes," *Phil. Trans. R. Soc. Lond.*, **362**, 2065 (2004).

[81] S. Reich, C. Thomsen, and P. Ordejon, "Elastic properties of carbon nanotubes under hydrostatic pressure," *Phys. Rev. B,* **65**, 153407-1 (2002).

[82] D. Y. Sun, D. J. Shu, M. Ji, F. Liu, M. Wang, and G. Gong, "Pressure-induced hard – to-soft transition of a single carbon nanotube," *Phys. Rev. B,* **70**, 165417-1 (2004).

[83] M. H. F. Sluiter, V. Kumar, and Y. Kawazoe, "Electronic structure of single wall carbon nanotube bundles under compression as compared to graphite and hexagonal graphene stacking," *Physica B,* **323**, 203 (2002).

[84] M. H. F. Sluiter and Y. Kawazoe, "Phase diagram of single-wall carbon nanotube crystals under hydrostatic pressure," *Phys. Rev. B,* **69**, 224111-1 (2004).

[85] X. Ye, D. Y. Sun, and X. G. Gong, "Pressure-induced structural transition of double-walled carbon nanotubes," *Phys. Rev. B,* **72**, 035454-1 (2005).

[86] X. H. Zhang, D. Y. Sun, Z. F. Liu, and X. G. Gong, "Structure and phase transitions of single-wall carbon nanotube bundles under hydrostatic pressure," *Phys. Rev. B,* **70**, 035422-1 (2004).

[87] A. D. Bozhko, D. E. Sklovsky, V. A. Nalimova, A. G. Rinzler, R. E. Smalley, and J. E. Fischer, "Resistance vs. pressure of single-wall carbon nanotubes," *Appl. Phys. A,* **67**, 75 (1998).

[88] J. Tan, L. C. Qin, T. Sasaki, M. Yudasaka, A. Matsushita, and S. Iijima, "Structure and property changes of single-walled carbon nanotubes under pressure," *Synthetic Met.,* **121**, 1245 (2001).

[89] A. K. Sood, "Carbon nanotubes: pressure-induced transformations and voltage generation by flow of liquids," *Radiat. Phys. Chem.,* **70**, 647 (2004).

[90] J. A. Elliott, J. K. W. Sandler, A. H. Windle, R. J. Young, and M. S. P. Shaffer, "Collapse of single-wall carbon nanotubes is diameter dependent," *Phys. Rev. Lett.,* **92**(9), 095501-1 (2004).

[91] R. B. Capaz, C. D. Spataru, P. Tangney, M. L. Cohen, and S. G. Louie, "Hydrostatic pressure effects on the structural and electronic properties of carbon nanotubes," *Phys. Stat. Sol.(b),* **241**(14), 3352 (2004).

[92] Y. Xia, M. Zhao, Y. Ma, M. Ying, X. Liu, P. Liu, and L. Mei, "Tensile strength of single-walled carbon nanotubes with defects under hydrostatic pressure," *Phys. Rev. B,* **65**, 155415-1 (2002).

[93] T. Natsuki, T. Hayashi, and M. Endo, "Mechanical properties of single- and double-walled carbon nanotubes under hydrostatic pressure," *Appl. Phys. A,* **83**, 13 (2006).

[94] T. Komoda, Y. Endo, K. Kyuno, and A. Toriumi, "Field-dependent mobility of highly oriented pentacene thin-film transistors," *Jpn. J. Appl, Phys.*, **41**, 2767 (2002).

[95] V. C. Sundar, J. Zaumseil, V. Podzorov, E. Menard, R. L. Willett, T. Someya, M. Gershenson, and J. A. Rogers, "Elastomeric transistor stamps: reversible probing of charge transport in organic crystals," *Science*, **303**, 1644 (2004).

[96] Y. Xia, V. Kalihari, C. D. Frisbie, K. Nam, and J. A. Rogers, "Tetracene air-gap single-crystal field-effect transistors," *Appl. Phys. Lett.*, **90**, 162106 (2007).

[97] E. Menard, V. Podzorov, S. Hur, A. Gaur, M. E. Gershenson, and J. A. Rogers, "High-performance n- and p-type single-crystal organic transistors with free-space gate dielectrics," *Adv. Mater.*, **16**(23), 1097 (2004).

[98] L. Diao, C. D. Frisbie, D. D. Schroepfer, and P. P. Ruden, "Electrical characterization of metal/pentacene contacts," *J. Appl. Phys.*, **101**, 014510 (2007).

[99] P. S. Davids, I. H. Campbell, and D. L. Smith, "Device model for single carrier organic diodes," *J. Appl. Phys.*, ***82***(12), 6319 (1997).

List of publications

D. D. Schroepfer, P. P. Ruden, Y. Xia, C. D. Frisbie, and S. E. Shaheen, "Hydrostatic pressure effects on poly(3-hexylthiophene) thin film transistors," *Appl. Phys. Lett.*, **92**, 013305 (2008).

L. Diao, C. D. Frisbie, D. D. Schroepfer, and P. P. Ruden, "Electrical characterization of metal/pentacene contacts," *J. Appl. Phys.*, **101**, 014510 (2007).

Y. Liu, M. Z. Kauser, D. D. Schroepfer, P. P. Ruden, J. Xie, Y. T. Moon, N. Onojima, H. Morkoc, K. –A. Son, and M. I. Nathan, "Effect of hydrostatic pressure on the current-voltage characteristics of GaN/AlGaN/GaN heterostructure devices," *J. Appl. Phys.*, **99**, 113706 (2006).